Dissertation

submitted to the

Combined Faculties for the Natural Sciences and for Mathematics

of the Ruperto-Carola University of Heidelberg, Germany

for the degree of

Doctor of Natural Sciences

presented by

MSc. Hui LI

born in: Hebei, China

Oral-examination: November 2010

Assembly, stability and regulation of flagellar motor in *Escherichia coli*

First referee: Prof. Dr. Victor Sourjik

Second referee: PD Dr. Matthias P. Mayer

To my parents

Acknowledgements

First and foremost, I would like to express my sincere gratitude to Prof. Dr. Victor Sourjik for his supervision, encouragement and support throughout the entire course of my PhD study.

Also, I am very grateful to PD Dr. Matthias Mayer for his kind guidance, helpful discussion and valuable advice.

This work would not have been done without the financial support by the "Heinz Goetze Memorial Fellowship Program" of the Athenaeum Foundation. Many thanks go to Dr. Dietlind Wünsche for her all-round help and assistance when I was just starting in Heidelberg.

Part of this work has been done by collaborating with Prof. Dr. Urs Jenal and Dr. Alex Boehm in Biocenter, University of Basel, Switzerland. I wish to thank them for the pleasant collaboration.

I am grateful as well to all the former and present colleagues in the lab for giving me indispensible help, creating a wonderful and fun working environment. Especially, I would like to thank, Linda Løvdok for her patience when I was new to the lab, David Kentner for providing many plasmids and helpful discussions about my project, Silke Neumann for helping me to translate the summary of my dissertation into German and also sharing a laugh during movie nights, Abiola Pollard and Alvaro Banderas for their proof-reading of my dissertation manuscript and very helpful suggestions.

Despite the distance, my parents have always been there for me. My deepest gratitude goes to them for their endless support and constant inspiration through years.

Lastly, I would like to thank my beloved Qiang for sharing his memories and experiences with me, for his constant encouragement and understanding, and for always being willing to help me.

Contents

Zusammenfassung

Der bakterielle Flagellenmotor ist eine hochgeordnete und komplexe supramolekulare Struktur, die zwei Funktionen ausübt: Zum einen als rotierender Motor, der die Drehung der Flagellen antreibt und somit die Schwimmbewegung an die chemotaktische Wahrnehmung koppelt; Zum anderen als Typ III Proteinexportapparat, der zur Bildung der extrazellulären Flagellen benötigt wird. Die Biogenese des Motors ist ein eindrucksvolles Beispiel molekularer Selbstorganisation, bei der eine Vielzahl verschiedener Proteine mehrere oligomere Ringe in Zytoplasma, Periplasma und Plasmamembran bilden. Während die späten extrazellulären Schritte der Flagellenbildung vergleichsweise gut verstanden sind, ist über die frühen Schritte, die an der Bildung der Motorstrukturen im Zytoplasma und in der Plasmamembran beteiligt sind, nur wenig bekannt.

In dieser Arbeit wurde mithilfe von Fluoreszenzmikroskopie die Motor-Assemblierung in *E. coli* analysiert und mittels Fluoreszenz-Resonanz-Energie-Transfer (FRET) die zugrundeliegenden Proteininteraktionen *in vivo* untersucht. Die Analyse zeigte, dass FlhA, eine Komponente des Proteinexportapparats, die Fähigkeit besitzt, sich unabhängig von anderen Motorkomponenten spontan zusammenzulagern. Diese Zusammenlagerung stellt sehr wahrscheinlich den ersten Schritt in der Bildung des Motors dar, und ist gefolgt von einer Rekrutierung der MS-Ring Komponente FliF sowie der geordneten Anlagerung anderer Motorstrukturen, wobei die Assoziation jeder weiteren Struktur den wachsenden Komplex zu stabilisieren scheint. Darüber hinaus wurde durch Fluoreszenz Recovery After Photobleaching (FRAP) ein dynamischer Proteinaustausch in Teilen des funktionalen Motors nachgewiesen. Ferner konnte ein von der Reifung abhängiger Schutz der Motorkomponenten gegen proteolytischen Abbau festgestellt werden, was darauf hinweist, dass nicht eingebaute Untereinheiten durch einen Mechanismus der Proteinqualitätskontrolle entfernt werden. Außerdem wurde gezeigt, dass die DnaK/HtpG-Maschinerie sowohl an der Bildung des Flagellenmotors als auch an der Bildung chemosensorischer Komplexe beteiligt ist, und dass eine regulatorische Rolle zwischen YcgR, dem Bindeprotein von cyclischem di-GMP, und dem Stator-Protein MotA besteht.

Die vorliegende Arbeit liefert einen neuen und den bisher vollständigsten Einblick in die frühen Schritte der Bildung des Flagellenmotors und ermöglicht ein besseres strukturelles Verständnis des Flagellen-Exportapparats und anderer Typ III Sekretionssysteme. Das beobachtete Zusammenspiel zwischen Hierarchie und Kooperativität im Bildungssprozess spielt vermutlich auch bei der Assemblierung von anderen großen intrazellulären Komplexen eine Rolle.

Summary

Bacterial flagellar motor is a highly ordered and complex supramolecular structure with two functions: it is both a rotary engine that powers the rotation of the flagella, coupling swimming to chemotactic signaling, and a type III protein export apparatus needed for assembly of extracellular flagella. Motor biogenesis represents a formidable example of self-assembly, involving a number of different proteins that form multiple oligomeric rings in the cytoplasm, periplasm and plasma membrane. Although late extracellular steps of the flagellar assembly process are comparatively well understood, much less is known about the early steps of the motor structure formation in the cytoplasm and in the plasma membrane.

We used fluorescence imaging to dissect the order of the motor assembly in *Escherichia coli* cells and fluorescence resonance energy transfer (FRET) to map *in vivo* the underlying protein interactions. We observed that the self-association of the membrane export apparatus protein FlhA is independent of the other motor components, thus it is likely to be the first step in motor assembly. It is followed by the recruitment of the MS-ring component FliF and the ordered association of other motor structures with the association of each subsequent structure appearing to stabilize the growing assembly. We further applied fluorescence recovery after photobleaching (FRAP) to show that parts of the assembled motor undergo dynamic protein exchange. In addition, we found an assembly-dependent stabilization of motor components against proteolytic degradation, indicating removal of the unassembled motor subunits through a protein quality control mechanism. Furthermore, we additionally demonstrated the involvement of DnaK/HtpG machinery in assembly of flagellar motor and chemosensory complexes and showed regulatory interactions between cyclic di-GMP binding protein YcgR and the stator component of flagellar motor MotA.

Our results provide a novel and thus far the most comprehensive view of the early steps of flagellar motor assembly, enabling a better structural understanding of the flagellar export apparatus and other type III secretion systems. We believe that the observed combination of hierarchy and cooperativity in the assembly process could be common to many large intracellular complexes.

1 Introduction

Many unicellular organisms are able to move. Although movement requires energy expenditure, the ability to move in their habitat has profound consequences for cells and may mean the difference between life and death. Motility allows the cell to reach different regions of its environment. In the competition for survival, movement to a new location may offer a cell new resources and opportunities. Many species of bacteria can sense a wide range of environmental signals, such as changes in chemical gradients, pH, osmolarity or mechanical cues. Chemotaxis is the perception of spatial gradients of these signals and the generation of a motility response that allows cells to move up the gradient. The mechanism of motility response relies on a two-component system around a histidine protein kinase and a response regulator that regulates the motor apparatus. There are different types of motility including swimming and gliding, though the majority of motile bacteria move by means of flagella.

1.1 Bacterial chemotaxis sensory system

1.1.1 The biased random walk

The chemotaxis phenomenon has been well studied in motile bacteria, such as the enterobacterium *Escherichia coli* that swims by the rotation of flagella. *E. coli* is equipped with about half a dozen flagella, the filamentous organelles randomly distributed over the cell surface. Each flagellum consists of a long (~10 μm), thin (~20 nm) and helical filament, turned like a screw by a rotary motor at its base [1-4].

The motile behavior of an *E. coli* cell is characterized by the execution of a three-dimensional random walk, a sequence of smooth-swimming runs interrupted by tumbles, in which the cell erratically moves in place, randomly re-orienting itself before swimming off in a new direction [5]. Swimming and tumbling are the result of different rotational directions of the flagellar motor [6]. When the motors turn counterclockwise (CCW, viewed from filament to motor), the filaments work together in a bundle to drive the cell forward in a run. Clockwise (CW) rotation leads to tumbling when the bundle flies apart as shown in Figure 1. Without attractant or repellent, the tumbling events occur about once per second [5]. Movement is biased towards favorable directions by the control of swimming and tumbling probabilities. Receptors near the surface of the cell

count molecules of interest (sugars, amino acids, dipeptides) and control the direction of flagellar rotation. If a particular direction is deemed favorable, it is extended, i.e. the motors spin CCW longer than they otherwise would. This bias enables cells to actively find the favorable regions in their environment. Conversely, lower attractant or higher repellent concentrations stimulate CW rotation, so that the cell tumbles and changes course. The bacterium is able to sense differences in concentrations over a time span long enough to overcome local fluctuations of attractant. However, if exposure to constantly high concentrations of attractant is long enough, the cell starts to adapt to these concentration and returns to its original run and tumble behavior [7].

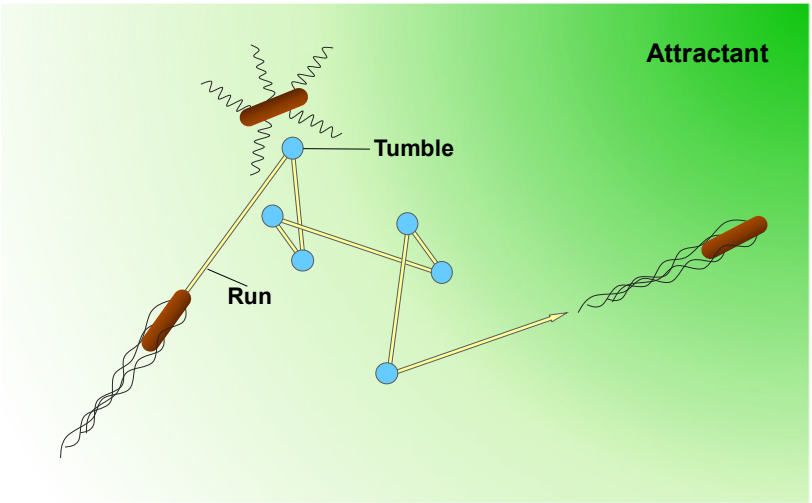

Figure 1: Chemotactic swimming behavior of *E. coli*. The cells swim in straight runs interrupted by short tumbles during which the cell changes direction. Increasing attractant concentration prolongs the run length so that the cell continues to move towards the attractant source. Repellents are avoided by increasing the tumbling frequency.

1.1.2 Chemotaxis signalling pathway

The chemotaxis signaling pathway of *E. coli* has been characterized in detail on the genetic, biochemical and structural levels. The entire pathway includes five chemoreceptors (Tsr, Tar, Trg, Tap, and Aer), which are also called methyl-accepting chemotaxis proteins (MCPs), six cytoplasmic chemotaxis proteins (CheA, CheW, CheR, CheB, CheY, and CheZ), and three proteins comprising a switch complex at the cytoplasmic face of the flagellar motor (FliM, FliN, and FliG) [8]. The sensor of the pathway is a chemoreceptor in the cytoplasmic membrane and a cytoplasmic histidine kinase associated with the chemoreceptor. The response regulator interacts directly with the flagellar motor. An overview of the pathway is shown in Figure 2.

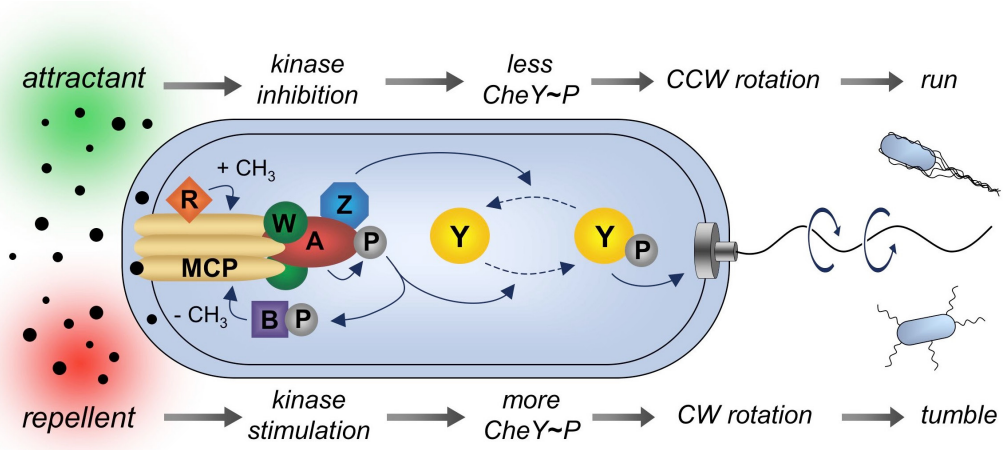

Figure 2: The chemotaxis signalling pathway. Receptors (MCPs) form a sensory complex with kinase CheA and the small adaptor protein CheW. Binding of ligands to the periplasmic receptor domain regulates the autophosphorylation activity of the kinase. The phosphoryl group is transferred to the response regulator CheY, which thereupon binds the flagellar motor, inducing clockwise (CW) rotation and tumbling of the cell. Attractants inhibit the kinase and phosphor-CheY is rapidly degraded by the phosphatase CheZ, which leads to counterclockwise (CCW) motor rotation and smooth swimming of the cell. Methyltransferase CheR and methylesterase CheB, which is also activated by phosphorylation from CheA, fine-tune the ability of receptors to stimulate CheA by adjusting the level of receptor methylation. The figure is kindly provided by Dr. D. Kentner.

The bacterial chemotaxis signalling pathway belongs to the two-component superfamily of signaling pathways [9], with two key proteins being the receptor-associated histidine kinase CheA and the response regulator CheY. Together with the small adaptor protein CheW, CheA is coupled to chemoreceptors anchored in the membrane [10]. The kinase activity of CheA is modulated by the binding of ligands to chemoreceptors and by the methylation state of the chemoreceptors: attractant binding and low receptor methylation state reduce CheA auto-phosphorylation activity, whereas repellent binding, attractant removal and increased receptor modification all increase CheA auto-phosphorylation activity. The phosphoryl group is subsequently transferred to CheY that in its phosphorylated state binds to the flagellar motor and induces CW rotation [11, 12]. Dephosphorylation of phospho-CheY is catalyzed by the phosphatase CheZ.

CheR, a methyltransferase, and CheB, a methylesterase, mediate adaptation to a constant attractant concentration by adjusting the methylation level of receptors [13-15]. An enhanced methylation level leads to more active receptors, and removal of methyl groups decreases the receptor activity. CheR is constitutively active, whereas CheB is a response regulator that is activated through phosphorylation from CheA [16, 17] and thereby

provides a negative feedback mechanism. Hence, ligand-induced changes in CheA-activity lead to an opposite regulation by receptor methylation, which counteracts the initial signal, until kinase activity returns to the pre-stimulus state. The adaptation system serves as a memory of past conditions because methylation works slower than the phosphorylation response, allowing temporal measurements of concentration changes. The adaptation system ensures remarkable sensitivity of the chemotactic response to small relative changes in the concentrations of multiple chemical signals over a broad range [5].

1.2 Bacterial flagellar motor

1.2.1 Structure and mechanism of flagellar motor

Flagellar motor is the output of chemotaxis sensory system. The best-studied bacterial flagellar motors are those of the gram-negative organisms, *Escherichia coli* and the closely related *Salmonella typhimurium*. These bacteria are rod-shaped, about 1 μm in diameter and 2-4 μm long. A cell is propelled by a set of four to six helical flagellar filaments that arise at random points on its sides and extend several body lengths out into the external medium (Figure 3).

A functional flagellum can be divided into motor, hook and filament (Figure 3). The motor is embedded within the cell envelope, while the hook and filament extend outwards from the cell body. The bacterial flagellar motor is a marvelous nanomachine, no more than 50 nm in diameter, built from about 20 different kinds of parts, the components of which have been honed to perfection by billions of years of evolution. It can be driven by the proton or sodium ion motive force across the cell membrane and spins CCW or CW at speeds on the order of 100 Hz. Like any rotary motor, the flagellar motor consists of two main parts: the stator and the rotor [3, 18]. The rotor spins relative to the cell and is attached to the helical filament by a universal joint called the hook, whereas the stator is anchored to the cell wall (Figure 3 C). The hook permits articulation between one angular direction of rotation for the motor and a different angular rotation for the filament [19]. The helical filament is composed of up to 20,000 subunits of a single protein that is capped by a scaffold, which permits the folding and polymerization of secreted filament subunits as they reach the tip of the structure following secretion [20].

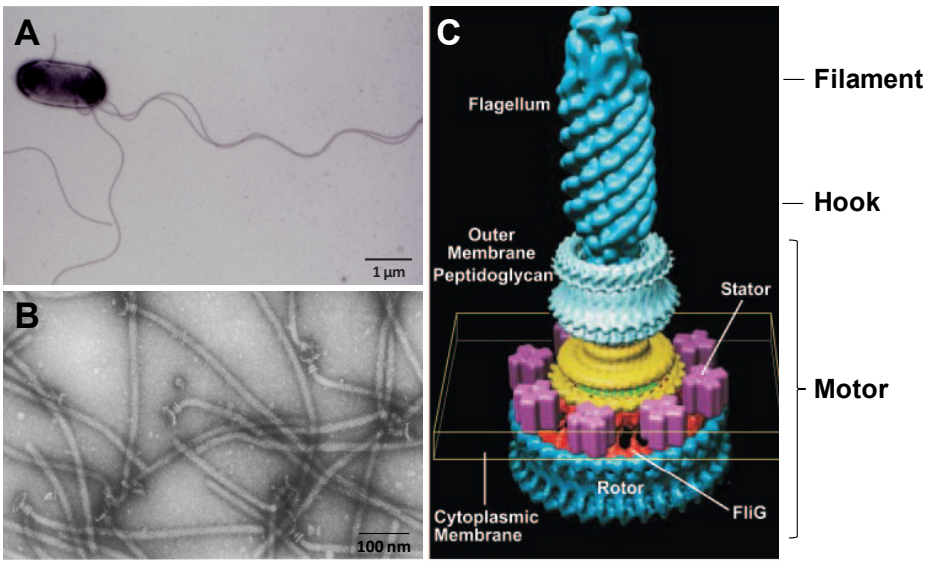

Figure 3: The structure of bacterial flagellum and flagellar motor. (A) Electron microscopy image of *Salmonella typhimurium* cell with multiple flagella, downloaded from http://www.bacteriophagetherapy.info. (B) Electron microscopy image of the flagellar fragments isolated from wild-type *Salmonella typhimurium* [21]. (C) The overall structure of the bacterial flagellar motor, based on cryo-electron microscopy [22].

The flagellar motor is one of the largest molecular machines in bacteria, with a molecular mass of ~11 MDa, ~13 different component proteins, and a further ~25 proteins required for its expression and assembly [20]. The overall structure of the flagellar motor has been determined by electron microscopy (EM), in particular single-particle image reconstruction by cryo-EM. Along with an EM reconstruction of the rotor from *Salmonella typhimurium* [23-25], a bacterial flagellum of gram-negative bacteria is shown schematically in Figure 4. The rotor consists of a basal body and a cytoplasmic switch complex. The basal body spans three layers of the cell envelope [26-28] with a set of rings up to ~45 nm in diameter. The L- and P- rings are embedded in the outer lipopolysaccharide membrane and peptidoglycan cell wall, respectively, and thought to work as a bushing between the rotor and the outer parts of the cell envelope. The MS-ring is located at the cytoplasmic membrane, which consists of ~26 copies of a single protein, FliF [29, 30]. The switch complex is also a ring-like structure that consists of three proteins FliG, FliM and FliN. The interaction between FliG and MotA is responsible for the torque generation [31], whereas FliM and FliN form a cytoplasmic bell-like structure called C-ring that binds the phosphorylated response regulator CheY and modulates the direction of motor rotation. In proton driven flagellar motors, the stators are complexes of two proteins MotA and MotB that form 8 to 10 proton channels per motor. When the

protons cross the membrane due to the difference of electric and chemical potential (proton motive force, or PMF), they bind to a specific aspartate residue within MotB, causing a conformational change in the stator that drives the rotor through an elementary rotational step. This conformational change in the stator is followed by the de-protonation of the aspartate residue, release of the proton into the cytoplasm and restoration of the stator to its original conformation [32]. In some marine and alkalophilic bacteria (for example, *Vibrio* and *Bacillus* species), sodium ions, instead of protons, are used for the same function [18].

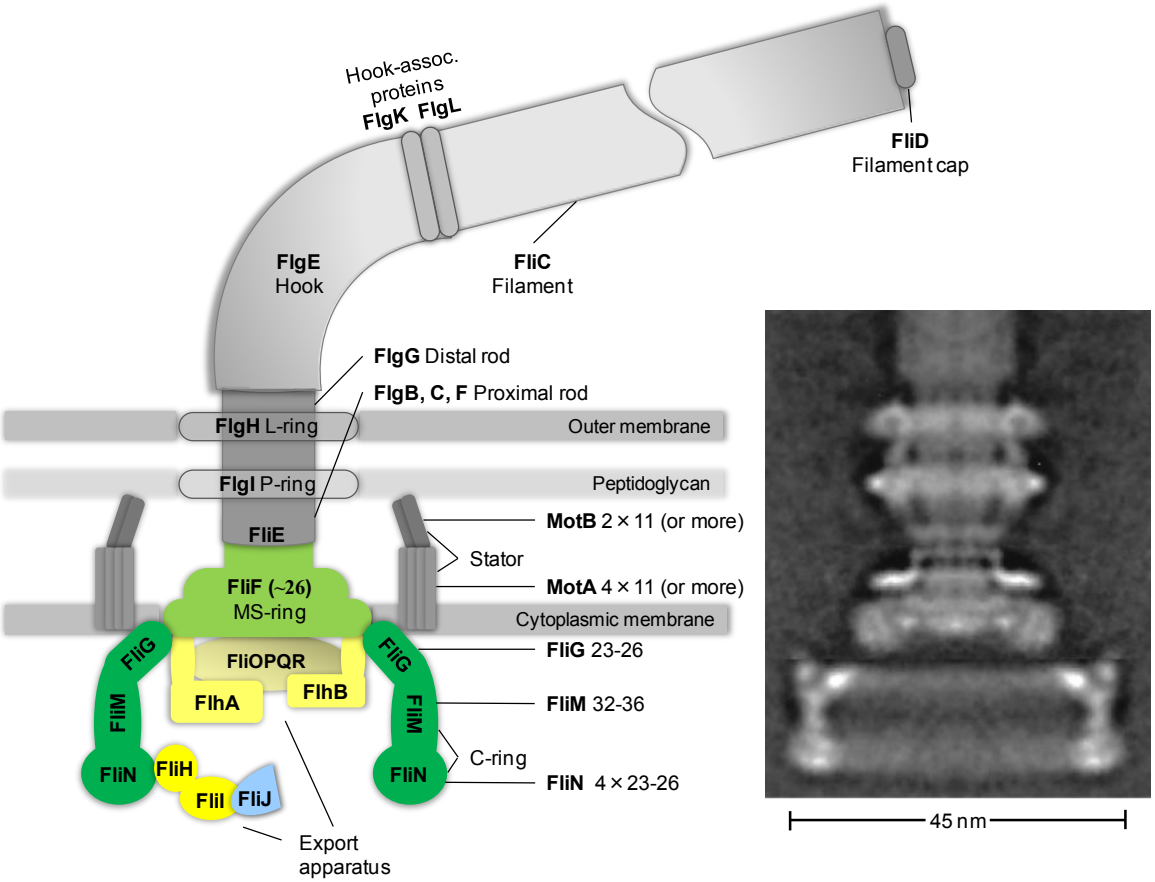

Figure 4: Schematic representation of bacterial flagellum. A schematic diagram of the flagellar motor, drawn to scale, compared to a rotationally averaged reconstruction of images of hook-basal bodies taken by cryo-electron microscopy. Individual proteins are indicated. The general morphological features are C-ring, MS-ring, P-ring, L-ring, hook, hook-associated proteins (which include the distal cap), and filament. MotA, MotB and components of the export apparatus do not resist extraction with detergent and therefore do not appear on the right. This reconstruction is derived from rotationally averaged images of about 100 hook-basal body complexes of *Salmonella* polyhook strain SJW880, embedded in vitreous ice [23]. Connections between the C-ring and the rest of the structure appear relatively tenuous. The figure is adapted from [3].

1.2.2 The flagellar type III export apparatus

Many of the substructures of the bacterial flagellum are external to the cell, and therefore their subunits must be exported. As shown in Figure 4, by defining external structure as any structure being outside of the cytoplasmic membrane, the proteins that are required for the structure and assembly of the external portions of the bacterial flagellum are: MS-ring/rod junction (FliE), proximal rod (FlgB, FlgC and FlgF), distal rod (FlgG) and rod cap (FlgJ), periplasmic P-ring (FlgI), outer membrane L-ring (FlgH), hook (FlgE), hook cap (FlgD) and hook-length control (FliK), hook-filament junction proteins (FlgK and FlgL), filament (FliC) and filament cap (FliD), and the regulatory protein (FlgM). All of these proteins cross the cytoplasmic membrane, and all, except for those that form the P- and L-rings that are secreted through the Sec pathway, use the flagellar-specific type III protein export apparatus. The flagellar type III protein export apparatus is part of a family of type III secretion systems (T3SSs) that are used to secrete virulence factors by gram-negative plant and animal pathogens [33, 34]. T3SSs were initially characterized by the lack of substrate signal-peptide cleavage and structural disorder of N-terminal secretion signals [35, 36]. Later, other key features of T3SSs were proposed, including substrate-associated secretion chaperones that stabilize or target their cognate secretion substrates [37] and ATP hydrolysis that is coupled to the delivery of substrates for PMF-dependent secretion from the cell [38-40].

The substructures of bacterial flagellum have several specific cap protein complexes that are always attached at the distal end of the growing structure to promote the efficient assembly process. Since newly exported flagellar subunits are incorporated into the growing flagellar structure right below the cap protein complex, the physical path for the flagellar protein export is believed to be through the central channel of the growing flagellum, whose diameter is only about 2 nm [41-44]. Therefore, the translocated proteins are most likely to be exported in an unfolded or partially folded state [45]. The export of flagellar proteins requires at least 9 components, 6 of which are integral membrane proteins, FlhA, FlhB, FliO, FliP, FliQ and FliR, and three are soluble components, FliH, FliI and FliJ, which are responsible for translocation of all the flagellar export substrates [46]. In addition to these proteins, the cytoplasmic proteins FlgN, FliA, FliS and FliT act as substrate-specific chaperones that facilitate the export of their substrates [47-52].

The integral membrane proteins have been postulated to be located in a patch of

membrane within the putative central pore of the MS-ring, although the relatively small pore size limits the number of inserted proteins. FliP and FliR have been identified in the purified basal body, and FliR has been observed to be located at the cytoplasmic face of the MS-ring by immuno-electron microscopy [53]. The integral membrane protein complexes are now known to use proton influx to derive the secretion of flagellar substrates [39, 40]. FlhA and FlhB have substantial cytoplasmic domains, which could project into the space within the C-ring. FlhA is the largest component of the flagellar export apparatus [54] and has been implicated in substrate translocation [55, 56]. C-terminus of FlhA was reported to be an adaptor that receives the late flagella building blocks FliD and flagellin (FliC) only when bound to their cognate chaperones FliT and FliS, respectively [57]. FlhB acts as an export switch to control flagellar protein export according to the flagellar assembly process [58, 59]. The conformational change in the C-terminus of FlhB is directly involved in switching from rod/hook to filament substrates [60, 61]. Thus, C-termini of FlhA and FlhB together form a gate to facilitate specific proteins entry into the export channel. The role of transmembrane helices of integral membrane export components is not well understood.

Three soluble components form the ATPase complex: FliI is an ATPase, the central catalytic domain shows extensive similarity to the catalytic ß subunit of F_0F_1-ATP synthase [62]; FliH interacts with the N-terminal region of FliI and regulates its ATPase activity [63]; FliJ acts as a putative general chaperone [64]. FliI and FliH form a heterotrimeric complex and the energy of ATP hydrolysis of FliI is used to facilitate the release of the complex from the FlhA/FlhB export gate [45]. FliJ acts as an escort during flagellar assembly by binding to different flagellar specific chaperones, such as FlgN and FliT [65]. The FliHIJ complex and its associated ATPase activity are not essential for export, but serve to make the export process more efficient. ATP hydrolysis in virulence T3SS is known to unfold secretion substrates [38], indicating that the primary role of the FliHIJ ATPase complex is to shuttle substrates to the integral membrane secretion system and present them as unfolded substrates for efficient PMF-dependent secretion. As a number of interactions between FliHIJ complex and C-ring proteins were demonstrated [66-69], the C-ring was postulated to provide the binding sites for the FliHI-chaperone-substrate complexes, which increase the concentration of substrates near the export gate to allow their efficient docking to the FlhA-FlhB platform.

1.3 Regulation of flagellar operon expression

Flagellar assembly is a highly ordered process that requires the coordinated expression of dozens of genes. Flagellar and related genes are expressed within a temporal transcriptional hierarchy that results in their products being made as they are needed for assembly. The system is turned on during exponential growth phase. As shown in Figure 5, the whole regulon can be divided into three promoter classes with expression of operons at one level affecting expression at lower levels.

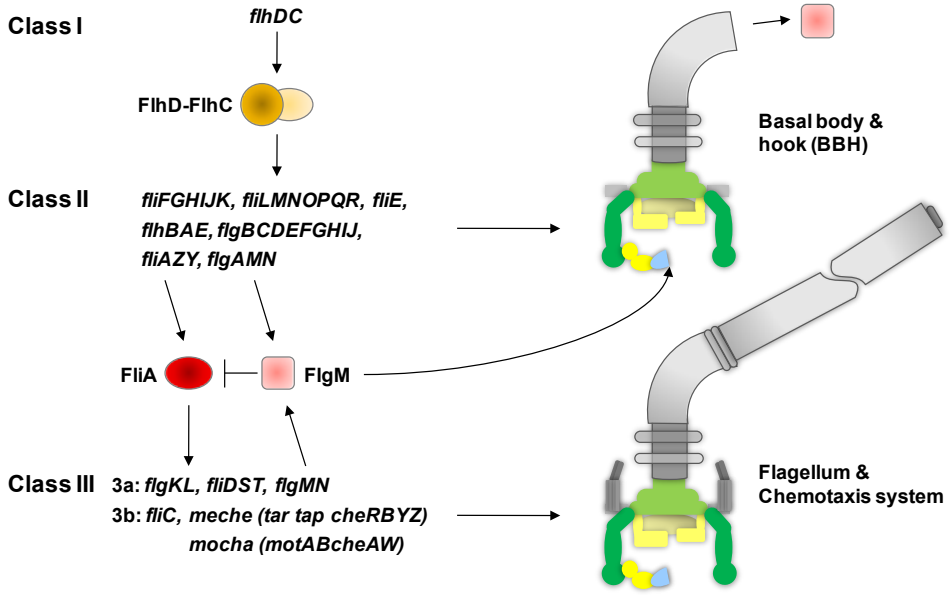

Figure 5: The genetically defined hierarchy of flagellar operons in *E.coli*. The master regulator FlhDC turns on class II genes, one of which, FliA, turns on class III genes. A checkpoint ensures that class III genes are not switched on until basal body and hook structures (BBH) are completed, which is implemented by FlgM that binds and inhibits FliA. When BBH are completed, they export FlgM out of the cell, leaving FliA free to activate the class III operons.

The master operon *flhDC* lies at the top of the hierarchy in class I, with its products being absolutely required for expression of all other genes in the flagellar regulon. It is regulated by signals from a variety of pathways, such as quorum sensing (QseBC, activator), osmolarity (OmpR, repressor) and protease degradation (ClpXP) [70]. Besides, LrhA is reported to be a key regulator controlling the transcription of flagellar, motility and chemotaxis genes by regulating the synthesis of FlhDC transcription factor [71]. Cyclic AMP [72] and the global *hns* gene [73] are known to be positive regulators of the flagella biosynthesis. Depending on the environmental conditions and growth phase, the alternative sigma factor σ^S, which is activated in post-exponential phase, can inhibit

FlhDC activity [74].

Class II genes encode components of the basal body and hook, the flagellar-specific sigma factor FliA (or σ^{28}) and the corresponding anti-sigma factor FlgM (or anti-σ^{28}) [75-77]. Within the class II cluster the promoters are turned on sequentially with significant delays in the order *fliL, fliE, fliF, flgA, flgB, flhB, fliA*. DNA regulatory sites in the promoter regions of the operons are ranked in affinity. When the concentration of a transcription factor increases in the cell, it binds to and activates the operons with the highest affinity sites first [78-80]. This observed order corresponds to the spatial position of the gene products during flagellar motor assembly starting in the cytoplasm and extending to the extracellular side. The *fliA* operon is the last class II gene to be switched on. When the transcription of *fliA* starts, the expression of FlhDC starts to decrease and the transcription of the class III operons begin.

Class III genes encode flagellin and other proteins needed late in the flagellar biogenesis, as well as chemotaxis proteins. The filament structural operons *flgK, fliD* and *fliC* are activated first, before *flgM* and the operons *mocha* and *meche*. The *mocha* operon consists of flagellar stator genes *motA* and *motB* and the chemotaxis genes *cheA* and *cheW*. The *meche* operon consists of chemotaxis genes *tar, tap, cheR, cheB, cheY* and *cheZ*. The other three receptors Tsr, Trg and Aer are encoded elsewhere in the genome [81]. FlgM binds to σ^{28} and prevents expression of class III genes [82]. Upon completion of the hook-basal body (HBB) complex, FlgM is secreted from the cell via the flagellar protein export apparatus that allows the class III genes to be expressed [83]. Thus, the flagellum has a direct role in regulating its own biosynthesis, with formation of the HBB complex serving as a key checkpoint for controlling flagellar gene expression.

Several additional feedback mechanisms have been suggested. FliZ, which is expressed from both class 2 and class 3 promoters, is a positive activator of class 2 promoters [84, 85]. Aldridge *et al.* [86] have recently observed that in *Salmonella typhimurium*, FliZ regulates the concentration of $FlhD_4C_2$ posttranslationally. FliT is a secretion chaperon for the flagellar cap protein FliD. Upon BBH completion, FliD is exported, thus raising the intracellular levels of free FliT. Free FliT then binds to FlhDC and thereby inhibits class II promoter activation [87].

1.4 The morphogenetic pathway of motor assembly

The bacterial flagellum is both a motor organelle and a protein export/assembly apparatus.

Its assembly proceeds successively from most cell-proximal structures to most cell-distal ones; it begins with the basal body, followed by the hook and finally by the filament (Figure 6). This order was recognized by Suzuki *et al.* [88], who studied mutants of *Salmonella* defective for different flagellar genes and searched for incomplete flagellar structures in pellets obtained from detergent extracts. The simplest structure found was a "rivet," comprising the MS-ring and rod. Similar result was obtained with mutants of *E. coli* [89]. A more recent study identified an even simpler initial structure, the MS-ring alone, and provided many details of the morphological pathway [90].

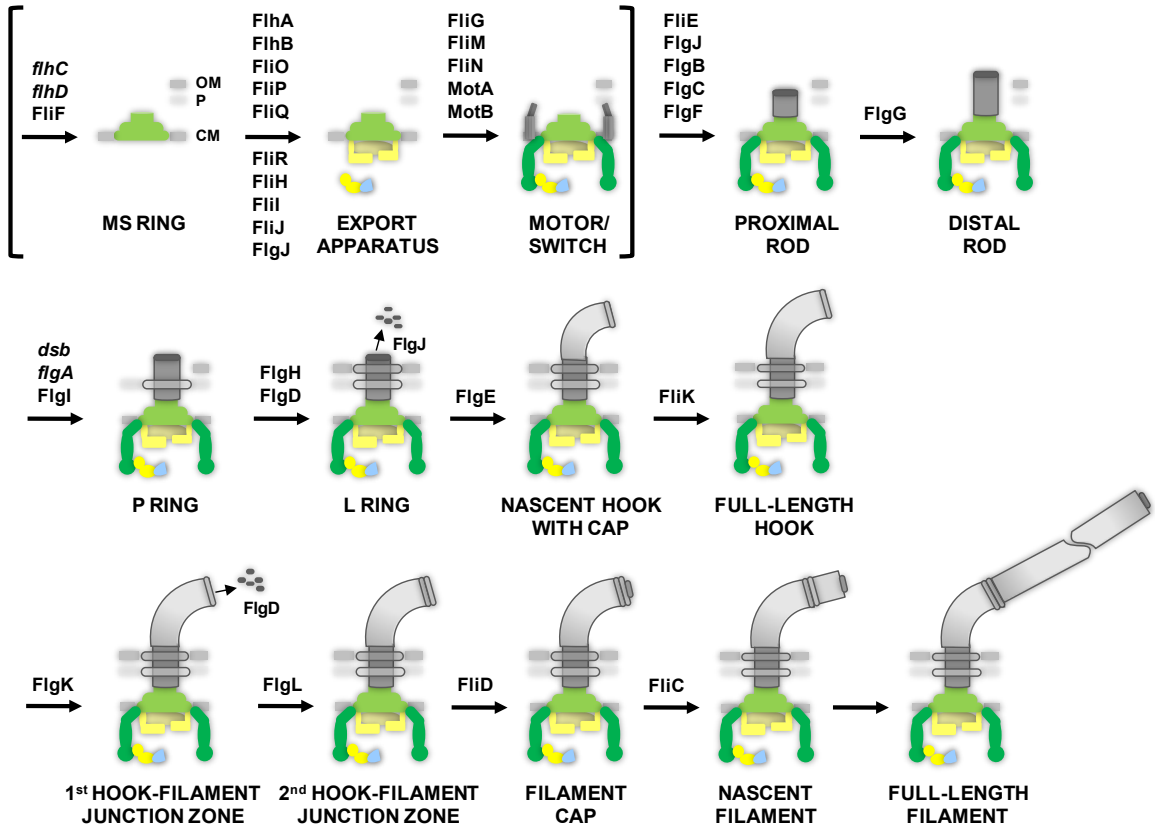

Figure 6: Morphogenetic pathway for the flagellum of *Salmonella*. The brackets indicate substructures that are assembled prior to the utilization of the type III export pathway. The Mot proteins constitute the stator element of the motor and are integral membrane proteins surrounding the MS-ring, while FliG and the C-ring (FliM and FliN) constitute the rotor/switch element of the motor and are peripheral membrane proteins mounted on the MS-ring. Genes (italics) or proteins necessary at each stage are indicated. The figure is adapted from [18].

Despite the overall progress in understanding the motor structure, early stages of motor assembly remain relatively obscure [18]. Overexpressed FliF was observed to self-assemble into the membrane-embedded MS-ring [91], and it is thus frequently

assumed to be the first assembled unit of flagellar motor [18, 92]. However, there is no other independent evidence for the self-assembly of FliF at physiological expression levels, and the interplay between formation of the MS-ring and insertion of the membrane components of the export apparatus remains unclear [18]. The most probable scenario is that the MS-ring protein and export apparatus proteins insert and assemble in a coordinated fashion [18]. Two reports in the literature support this notion. The first, intergenic suppression data indicates that at least one of the export components, FlhA, interacts with the MS-ring protein FliF [54]. The second, a study with temperature-sensitive mutants [93] led to the conclusion that two membrane components of the export apparatus, FliP and FliR, are somehow sequestered except when the temperature-sensitive protein is the MS-ring protein.

FliG and the C-ring, the sole peripheral membrane structure, together constitute the rotor/switch and are mounted onto the MS-ring. FliG probably assembles first because it is firmly attached to the MS-ring. Whether the other two proteins, FliM and FliN, assemble in any particular order is not known. FliG and the C-ring can assemble onto the MS-ring even in the absence of the export apparatus [94], but it is doubtful that they do so in the wild-type cell since it seems improbable on geometrical grounds that a preexisting MS-ring would permit subsequent assembly of rotor switch complex [18]. Although little experimental data is available, assembly of the rotor/switch, i.e. FliG plus the C-ring, is probably a simple self-assembly process. The torque-generating units MotA and MotB are assumed to be incorporated into the structure anytime, however, given the intimate functional relationship between the Mot complexes as stator and the FliG and C-ring as rotor, they may not be able to nucleate onto the MS-ring alone. Experiments, in which the *mot* genes were induced after the rest of flagellar assembly had been completed, showed that the Mot proteins could still assemble and function at the late stage [95], but this event may occur earlier in the wild-type cell, perhaps following completion of the C-ring.

The later stages corresponding to assembly of the proximal and distal rod [96], the P- and L-rings and the filament are well understood based on the combination of genetic studies with electron microscopy and crystallography [18, 97] (Figure 6). The proximal (FlgB, FlgC, FlgF) and distal rod (FlgG) are sequentially assembled [96]. FliE is needed for this assembly and is thought to form a junction between the MS-ring and the proximal part of the rod [98, 99]. FlgJ is a bifunctional protein, having muramidase activity [100] and binding affinity for the rod proteins [101]. The N-terminal domain of FlgJ is believed to

function as a rod capping protein, in which case it would be the first protein to be assembled onto the FliE substructure. The order of addition of the rod proteins themselves is a matter of debate. After completion of the distal rod, construction of the hook (FlgE) begins, but it does not proceed very far until the P- and L-rings (FlgI and FlgH) are assembled. FlgA is required for the assembly of P-ring [102] where the formation of disulfide bonds is catalyzed by DsbA and DsbB [103]. Assembly of the L-ring requires its constituent protein FlgH [104] and the flagellum-specific muramidase FlgJ [101]. When the hook has reached its mature length with the help of the cap protein FlgD and the length-control protein FliK, the cap is discarded and is replaced by three successive hook-associated proteins HAP1 (FlgK), HAP3 (FlgL), and HAP2 (FliD) [105]. Finally, the flagellin subunits FliC are inserted under the cap protein FliD to complete the formation of flagellar filament [41, 106].

1.5 Additional proteins controlling flagellar motor function and assembly

1.5.1 Proteins reported to interact with flagellar motor

Several additional proteins have been reported to interact with the motor, possibly modulating its function. Membrane-bound fumarate reductase (FRD) is a respiratory complex consisting of FRDA, FRDB, FRDC and FRDD subunits and was primarily expressed and functional under anaerobic conditions. Nonetheless, under aerobic conditions, it was shown to bind to FliG and to affect flagellar assembly and motor switching [107]. FRD binds to preparations of isolated switch complexes, forms a 1:1 complex with the switch protein FliG, and this interaction is required for both flagellar assembly and switching the direction of flagellar rotation. Fumarate, known to be a clockwise/switch factor [108], affects the direction of flagellar rotation through FRD [107]. DNA-binding protein H-NS is believed to impact motility by affecting flagellar biogenesis as well as function [109, 110]. It was reported that H-NS-deficient cells are non-flagellated because of a reduced transcription of FlhDC [111]. The *hns* strain restored its flagellation in the presence of FlhDC, but the resulting strain was still non-motile [110]. On the other hand, H-NS also interacts with the FliG protein, as revealed by a yeast two-hybrid screening [109], and the tightness of H-NS-FliG interaction modulates the rotational speed of flagella [112].

Moreover, recent reports suggest that the second messenger cyclic di-GMP (c-di-GMP) inhibits motility in bacteria [113, 114]. This compound is produced by a family of enzymes called diguanylate cyclases (DGCs) and is degraded by specific phosphodiesterases (PDEs). DGCs typically harbor a C-terminal GGDEF output domain that catalyzes c-di-GMP production. PDEs harbor a catalytic C-terminal EAL domain [74, 115, 116]. GGDEF and EAL domain proteins are found in most bacteria, and in most cases a single bacterial genome encodes many different members of these protein families [117]. YcgR, a PilZ domain protein from *E. coli*, was shown to bind c-di-GMP *in vitro* and to interfere with *E. coli* motility upon genetic inactivation of the PDE YhjH [110, 113]. Interestingly, *yhjH* and *ycgR* are coregulated with the flagellar and chemotaxis genes [110, 118]. Besides, some DGCs and PDEs were genetically linked to YcgR-mediated motility control [119, 120]. For instance, deleting *yegE* and overexpressing *yfgF* suppress the motility defect of the Δ*yhjH* strain, which may be due to the decreased intracellular levels of c-di-GMP. Together, these observations suggest a simple model, as shown in Figure 7, where PDEs limit the cellular c-di-GMP concentration, thereby preventing YcgR activation by c-di-GMP, and consequently allowing for unrestricted motility.

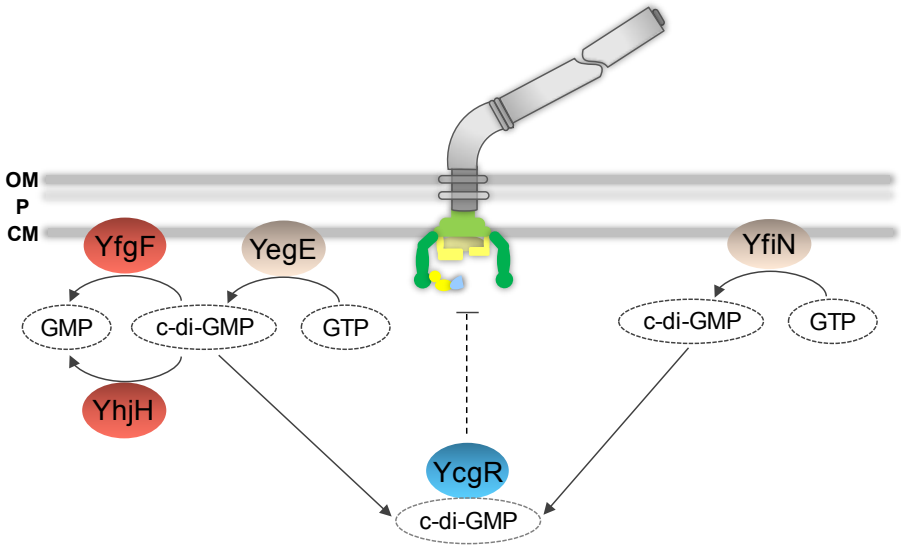

Figure 7: A model illustrating the influence of c-di-GMP signaling on motility. Genetic evidence suggests that the c-di-GMP second-messenger system is involved in motility control. The interaction of the YcgR-c-di-GMP complex with the flagellar motor is represented by a black dashed line. YegE and YfiN are DGCs. YfgF and YhjH are PDEs.

1.5.2 The Hsp70/Hsp90 multichaperone machinery

Heat-shock proteins (Hsps), known as chaperones, are highly conserved and present in all

organisms and in all cells. In eukaryotes, the Hsp70 machinery assists a large number of protein folding processes, including *de novo* folding of polypeptides, refolding of misfolded proteins, degradation of proteins, assembly and disassembly of oligomeric complexes, and the regulation of stability and activity of certain natively folded proteins [121, 122]. Some proteins are transferred to the Hsp90 machinery after they are processed by Hsp70. Figure 8 shows the connection between the Hsp70 and Hsp90 pathways in eukaryotes [123]. Newly synthesized and/or partially unfolded proteins are delivered to the Hsp70 complex via Hsp40. In most cases, Hsp70 is able to process the substrate on its own. However, certain substrates require Hsp90 for proper folding or activation. In this case, the scaffold protein Hop connects elements of the Hsp70 and Hsp90 machineries to form the intermediate complex. The Hsp70 component dissociates and, at the same time, p23 and prolylisomerases enter the complex. After that, the substrate is released from this final complex and Hsp90 is able to reenter the cycle by binding to Hop.

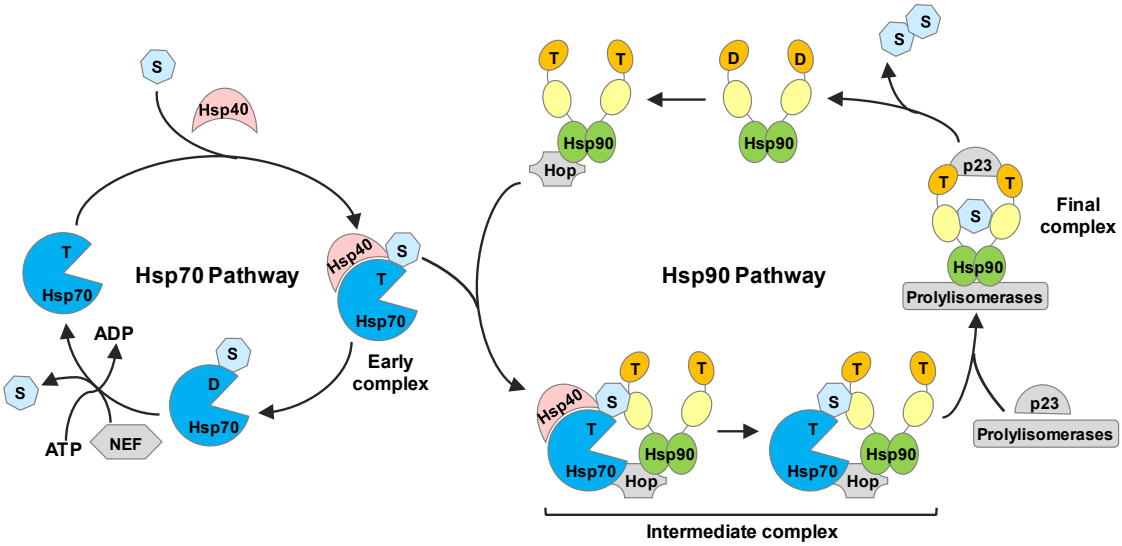

Figure 8: Connecting the Hsp90 and Hsp70 pathways in eukaryotes. Newly synthesized and/or partially unfolded proteins (S) are delivered to the Hsp70 complex via Hsp40. Two possible pathways branch from this "early complex". In most cases, Hsp70 is able to process the substrate on its own. After ATP hydrolysis, the nucleotide exchange factor (NEF) accelerates dissociation of ADP. Binding of ATP triggers substrate dissociation, and Hsp70 is ready to reenter the cycle. There are certain substrates which require Hsp90 for proper folding or activation. In this case, the scaffold protein Hop connects elements of the Hsp70 and Hsp90 machineries to form the "intermediate complex." The Hsp70 component dissociates and, at the same time, p23 and prolylisomerases enter the complex. After that, the substrate is released from this "final complex." After binding to Hop, Hsp90 is able to reenter the cycle. T: ATP-bound form, D: ADP-bound form. The figure is adapted from [123].

In eukaryotes, assisted by a large number of cochaperones, Hsp90s interact with some 200 client proteins, which are mostly regulatory components of signal transduction pathways [124], such as steroid hormone receptors [125], helix-loop-helix transcription factors [126], tyrosine and serine/threonine kinases [127-131], and the tumor suppressor p53 [132, 133]. This indicates that the function of Hsp90 might be of special importance for signaling pathways and regulation. Given the fact that for substrates such as citrate synthase the interaction of Hsp90 with highly structured folding intermediates has been demonstrated [134], it is tempting to speculate that the Hsp90 chaperone machinery assists the activation, stabilization or assembly of client proteins.

In *E. coli*, four cytosolic members of the Hsp70 family exist [135], with DnaK as the most prominent member. DnaJ and CbpA act as cochaperones of DnaK, stimulating the ATPase activity of DnaK. GrpE acts as nucleotide exchange factor for DnaK [136-138]. Whereas cytoplasmic Hsp90 is essential for viability under all conditions in eukaryotes [130, 139], the bacterial homologue HtpG is dispensable under normal growth conditions [140-142], the substrates of which are largely unknown. However, based on the function of Hsp90 in eukaryotes, it is possible that HtpG is involved in the bacterial signaling and in assembly of multiprotein complexes.

1.6 Aims of the current work

Bacterial flagellar motor has been studied for over half a century, and many of its key features have been revealed. All the proteins that constitute the flagellar motor are known, and its structure and assembly process are generally understood. In addition to the motor itself, many proteins and factors that affect the switch or rotation of the motor have been found. Despite this remarkable progress, quite a few fundamental questions still remain to be addressed. For instance, a detailed structure of the flagellar motor has yet to be obtained, due to its large size and location in the membrane. Also, little is known about the early steps of the motor structure formation in the cytoplasmic membrane. Furthermore, the stability of protein association within the flagellar motor remains to be studied, which will help to understand the assembly and function of the flagellar motor.

To address these questions, we combined several fluorescence microscopy techniques to determine the order of the early steps of motor formation *in vivo*, to map protein interactions involved in the assembly process, and to investigate stability of the assembled motor in *E. coli*. In particular, we analyzed the localization of fluorescent fusions to

flagellar motor and export apparatus proteins in different background strains to determine the order of motor assembly. We applied acceptor photobleaching FRET to map all the motor protein interactions. This experiment was carried out in different background strains, in order to distinguish protein interactions that are directly involved in the motor assembly from indirect interactions, which only occur due to protein proximity in the functional motor. FRAP was used to examine the dynamics of flagellar proteins at a functional motor in the cell. Our results largely advance our understanding of the motor assembly and structure, which is relevant for other type III secretion systems.

2 Materials and methods

2.1 Chemicals

Chemicals used in this work are listed in Table 1.

Table 1 Chemicals used in this work

Chemical	Company
Agar Bacteriology	Fluka
Agar Select	Difco
Agarose ultra pure	Difco
Ammonium sulphate	Applichem
Ampicillin	Applichem
APS	Sigma
L-Arabinose	Sigma
Bacto tryptone	Difco
Bacto yeast extract	Difco
Bromophenol blue	Applichem
Calcium chloride-dihydrate	Roth
Chloramphenicol	Applichem
1kb plus DNA ladder	Invitrogen
EDTA	Merck
Ethanol	Applichem
Ethidium bromide	Applichem
D-glucose	Applichem
Glycerol 99.5 %	Gerbu
Glycine	Applichem
Hydrochloric acid	Applichem
Isopropyl-ß-D-thiogalactoside (IPTG)	Roth
Kanamycin sulphate	Applichem
Lactic acid	Sigma
Magnesium chloride	Invitrogen
Magnesium sulphate	Roth
Methanol	Applichem
α-methyl-D,L-aspartate	Sigma
dNTP set	Invitrogen
Potassium Chloride	Applichem
Potassium di-hydrogen phosphate	Applichem
Di-potassium hydrogen phosphate	Applichem
Poly-L-Lysine	Sigma-Aldrich
Sodium chloride	Applichem

Table 1 - Continued from previous page

Chemical	Company
Sodium Dodecylsulfate (SDS)	Serva
Sodium Hydroxide	Applichem
TEMED	Sigma
TRIS	Roth
Tween 20	Sigma

2.2 Enzymes

Enzymes used in this work are listed in Table 2. All enzyme reactions were carried out in provided reaction buffers according to the manufacturer's instructions.

Table 2 Enzymes used in this work

Enzyme	Company
Taq DNA Polymerase	Invitrogen
Pwo DNA Polymerase	Roche
T4 DNA Ligase	Invitrogen
Restriction endonucleases	New England Biolabs / Fermentas

2.3 Antibodies

Monoclonal mouse GFP-specific antibody JL8 (BD Biosciences) and fluorescently labelled anti-mouse IgG goat antibody IRDye^{TM}700DX (Rockland) were used for immunoblot as primary and secondary antibody respectively.

2.4 Media and buffers

2.4.1 Growth media

LB

10 g Tryptone

5 g Yeast extract

5 g NaCl

1 M NaOH

Add H_2O to total volume of 1 l and adjust pH to 7

TB

10 g Tryptone

5 g NaCl

1 ml NaOH (pH 7)

Add H_2O to total volume of 1 l

2.4.2 Tethering buffer

100 ml 0.1 M KPO_4

200 µl 0.5 M EDTA

13.4 ml 5 M NaCl

100 µl 10 mM Methionine

1 ml 10 M Lactic acid

Add H_2O to total volume of 1 l and adjust pH to 7 with NaOH

2.4.3 Buffers for DNA gel electrophoresis

50 × TAE buffer for gel electrophoresis

242 g Tris base

57.1 g Glacial acetic acid

100 ml 0.5 M EDTA, pH 8

Add H_2O to total volume of 1 l

6 × DNA loading buffer

0.25 % (w/v) Bromophenol blue

0.25 % (w/v) Xylene cyanol

30 % (w/v) Glycerol

2.4.4 Buffers and solutions for immunoblot

10 × Running buffer

144.2 g Glycine

30.3 g Tris base

10 g SDS

Add H_2O to total volume of 1 l

Transfer buffer

2.9 g Glycine

5.8 g Tris base

3.8 g SDS

200 ml Methanol

Add H_2O to total volume of 1 l

10 × TBS

88 g NaCl

12.1 g Tris base

Add H_2O to total volume of 1 l and adjust pH to 7.4

4 × Laemmli buffer

8% SDS

40% Glycerol

20% 2-mercaptoethanol

0.008% Bromphenol blue

0.34 M Tris

adjust pH to 6.8

12% Resolving gel

1.7 ml Water

2.0 ml 30% Acrylamide mix

1.3 ml 1.5 M Tris (pH 8.8)

50 µl 10% SDS

50 µl 10% APS

2 µl TEMED

Stacking gel

0.68 ml Water

0.17 ml 30% Acrylamide mix

0.13 ml 1.5 M Tris (pH 6.8)

10 µl 10% SDS

10 µl 10% APS

1 µl TEMED

2.5 Bacterial strains

Table 3 lists the bacterial strains used in this work, with description of the genotype, source of the strain and reference if the strain has been previously published.

Table 3 Bacterial strains used in this work

Strain	Relevant genotype	Background	Reference or source
RP437	wild type	-	[143]
VS116	Δ*flhC*	RP437	[144]
MG1655	wild type	-	[145]
HL2	*fliF::kan*	MG1655	This work
HL3	Δ*fliF*	MG1655	This work
ECK1938	*fliH::kan*	BW25113	[146]
HL5	*fliH::kan*	MG1655	This work
HL6	Δ*fliH*	MG1655	This work
ECK1939	*fliI::kan*	BW25113	[146]
HL7	*fliI::kan*	MG1655	This work
HL8	Δ*fliI*	MG1655	This work
ECK1944	*fliN::kan*	BW25113	[146]
HL9	*fliN::kan*	MG1655	This work
HL10	Δ*fliN*	MG1655	This work
ECK1937	*fliG::kan*	BW25113	[146]
HL11	*fliG::kan*	MG1655	This work
HL12	Δ*fliG*	MG1655	This work
ECK1945	*fliO::kan*	BW25113	[146]
HL13	*fliO::kan*	MG1655	This work
HL14	Δ*fliO*	MG1655	This work
ECK1940	*fliJ::kan*	BW25113	[146]
HL15	*fliJ::kan*	MG1655	This work
HL16	Δ*fliJ*	MG1655	This work
ECK1942	*fliL::kan*	BW25113	[146]
HL17	*fliL::kan*	MG1655	This work
HL18	Δ*fliL*	MG1655	This work
ECK1891	*motA::kan*	BW25113	[146]
HL19	*motA::kan*	MG1655	This work
HL20	Δ*motA*	MG1655	This work
ECK1880	*flhA::kan*	BW25113	[146]
HL21	*flhA::kan*	MG1655	This work
HL22	Δ*flhA*	MG1655	This work

Table 3 - Continued from previous page

Strain	Relevant genotype	Background	Reference or source
DFB228	Δ*fliM*	RP437	[144]
DFB232	Δ*fliM* Δ*fliN*	RP437	[144]
DFB247	Δ*fliM* Δ*fliG*	RP437	[144]
LL14	*fliM-cfp, cheY-yfp*	RP437	This work
LL22	*fliM-yfp*	RP437	This work
HL23	Δ*htpG*	MG1655	Gift from G. Kramer (ZMBH, Heidelberg)
HL24	*htpG::htpG*(E34A)	MG1655	Gift from G. Kramer (ZMBH, Heidelberg)

2.6 Primers and plasmids

Primers used in this work are listed in Table 4. Forward and reverse primers are denoted f and r respectively. Table 5 lists the plasmids used in this work with relevant genotype, source of the plasmid and references.

Table 4 Primers used in this work

Primer	Sequence	Restriction site	Gene	Purpose
HL9	aacagcccatgggtgacatgaataatcc	Nco I	*fliN f*	for pHL1
HL10	tattcaggatccacggctcaggcggcgcattc	BamH I	*fliN r*	for pHL1
HL11	ggaacaggatccgtgagtgacatgaataatcc	BamH I	*fliN f*	for pHL4
HL12	ggttattctagactaacggctcaggcggcg	Xba I	*fliN r*	for pHL4
HL13	taacgaccatgggtaacctgacaggcacc	Nco I	*fliG f*	for pHL2
HL14	ggcagaggatccgacataggtatcctcgccgc	BamH I	*fliG r*	for pHL2
HL15	taaataggatccgtgagtaacctgacaggc	BamH I	*fliG f*	for pHL31
HL16	cacggctctagatcagacataggtatcctcgcc	Xba I	*fliG r*	for pHL31
HL17	aggatgccatggtgcttatcttattaggttacc	Nco I	*motA f*	for pHL14
HL18	cttgatggatcctgcttcctcggttgtcgtc	BamH I	*motA r*	for pHL14
HL23	accgacccatgggtaatctggccgcg	Nco I	*flhA f*	for pHL22
HL24	aggttcgagctctttgccgccaattgtcgcc	Sac I	*flhA r*	for pHL22
HL26	gccagagagctcatgggtcggtttctcg	Sac I	*flhB r*	for pHL56
HL27	ggtgcgccatggatgcgactgcagcccag	Nco I	*fliF f*	for pHL18
HL28	cctgtcggatccctcatgatcgttatttatccac	BamH I	*fliF r*	for pHL18
HL29	gtggtgccatggccacgcgcctgactc	Nco I	*fliI f*	for pHL25
HL30	tctcctgagctctgacactgtcgggaaaatacg	Sac I	*fliI r*	for pHL25

Table 4 - Continued from previous page

Primer	Sequence	Restriction site	Gene	Purpose
HL31	gacgttgagctcggtaaaataattggtatcgacc	Sac I	*dnaK f*	for pHL23
HL32	atagggggatccttttttgtctttgacttcttc	BamH I	*dnaK r*	for pHL23
HL33	agacctccatggaaggacaagaaactcgtg	Nco I	*htpG f*	for pHL24
HL34	ggcattggatccggaaaccagcagctggttc	Sac I	*htpG r*	for pHL24
HL44	aacggcccatggcagaacatggtgcgctg	Nco I	*fliJ f*	for pHL29
HL45	ctaagcggatccttcaggtttcctcatggcg	BamH I	*fliJ r*	for pHL29
HL46	ggatacccatggctgataatctgccgtgg	Nco I	*fliH f*	for pHL30
HL47	gcgtggggatcccaccactcctggtgctg	BamH I	*fliH r*	for pHL30
HL50	cgcaacccatggctgattacgcgataagcaag	Nco I	*fliL f*	for pHL28
HL51	cccatggagctctcgcagaataaaagcggtatac	Sac I	*fliL r*	for pHL28
HL54	cgttagccatggataaccacgctactgtgc	Nco I	*fliO f*	for pHL37
HL55	aacgacggatccggatctcccgctacgc	BamH I	*fliO r*	for pHL37
HL56	agatccccatgggtcgtttattgtctgtcgc	Nco I	*fliP f*	for pHL39
HL57	tttgccggatccgctgtaaaagctctgcgc	BamH I	*fliP r*	for pHL39
HL60	gccgtaccatggtgcaggtgacaagcgaac	Nco I	*fliR f*	for pHL38
HL61	gttacgggatcctattaatggcaattcact	BamH I	*fliR r*	for pHL38
HL64	gcgaggggatccgtgtctgataatctgccgtg	BamH I	*fliH f*	for pHL43
HL65	ggcgcgtctagattacaccactcctggtg	Xba I	*fliH r*	for pHL43
HL66	aggagtagatctgtgaccacgcgcctgac	Bgl II	*fliI f*	for pHL40
HL67	ttatcttctagattatgacactgtcggga	Xba I	*fliI r*	for pHL40
HL68	agataaggatccgtggcagaacatggtgcg	BamH I	*fliJ f*	for pHL41
HL69	gcgctatctagatcattcaggtttcctcatg	Xba I	*fliJ r*	for pHL41
HL70	agaccgagatctgtgactgattacgcgataagc	Bgl II	*fliL f*	for pHL42
HL71	tcgccctctagattatcgcagaataaaagcgg	Xba I	*fliL r*	for pHL42
HL80	cggcatgagctcgggaaaccagcagctggttc	Sac I	*htpG r*	combined with HL33 for pHL52
HL81	ttttccccatgggtcattaccatgagcagttc	Nco I	*ycgR f*	for pHL54
HL82	cgatgtggatccgtcgcgcactttgtccgc	BamH I	*ycgR r*	for pHL54
HL83	gagtttggatccgtgagtcattaccatgagc	BamH I	*ycgR f*	for pHL55
HL84	acgcgatctagatcagtcgcgcactttgtc	Xba I	*ycgR r*	for pHL55
HL85	cgcttaactagttttccaggattggcgacg	SpeI	*flhB f*	for pHL56
HL87	gtgccttctagattactcatgatcgttatttatcc	Xba I	*fliF r*	combined with HL27 for pHL73
HL88	cgaaaaactagtggaggaatgtcgtgcaaac	Spe I	*frdA f*	for pHL63
HL89	caaaagggatccgccattcgccttctccttc	BamH I	*frdA r*	for pHL63
HL90	tggaggggatccgtgcaaacctttcaagccg	BamH I	*frdA f*	for pHL64

Table 4 - Continued from previous page

Primer	Sequence	Restriction site	Gene	Purpose
HL91	aggttttctagattagccattcgccttctccttc	Xba I	*frdA r*	for pHL64
HL92	gaaggcccatggctgagatgaaaaacctg	Nco I	*frdB f*	for pHL65
HL93	ttgcacggatccgcgtggtttcagggtcgc	BamH I	*frdB r*	for pHL65
HL94	aggagaggatccatggctgagatgaaaaacctg	BamH I	*frdB f*	for pHL66
HL95	atgttgtctagattagcgtggtttcagggtc	Xba I	*frdB r*	for pHL66
HL96	agtgcaccatggcgactaaacgtaaaccgtatg	Nco I	*frdC f*	for pHL67
HL97	tcaggcggatccccagtacagggcaacaaac	BamH I	*frdC r*	for pHL67
HL98	agcctgccatggttaatccaaatccaaagcgttc	Nco I	*frdD f*	for pHL68
HL99	ggcgatggatccgattgtaacgacaccaatcag	BamH I	*frdD r*	for pHL68
HL100	acgaggtgcgcgatgaatgcgactgcagcc attccggggatccgtcgacc	-	*fliF f*	for making strain HL2; [146, 147]
HL101	ttactcatgatcgttatttatccactggcgtg taggctggagctgcttcg	-	*fliF f*	for making strain HL2; [146, 147]
HL102	ataaggtctagattatttgccgccaattgtcg	Xba I	*flhA r*	combined with HL23 for pHL74

Table 5 Plasmids used in this work

Plasmid	Relevant genotype	Reference or source
pTrc99	Expression vector; pBR ori, pTrc promoter, Amp^R	[148]
pBAD33	Expression vector; pACYC ori, pBAD promoter, Cm^R	[149]
pDK2	Expression vector for cloning of N-terminal CFP^{A206K} fusions; pTrc99a derivative	[150]
pDK4	Expression vector for cloning of N-terminal YFP^{A206K} fusions; pTrc99a derivative	[150]
pDK66	Expression vector for cloning of C-terminal YFP^{A206K} fusions; pTrc99a derivative	[150]
pDK85	Expression vector for cloning of C-terminal CFP^{A206K} fusions; pTrc99a derivative	[150]
pDK113	Expression vector for cloning of C-terminal CFP^{A206K} fusions; pTrc99a derivative; start code of CFP^{A206K} was changed from atg to gtg	This work
pDK79	Expression vector; pACYC ori, pBAD promoter, Kan^R	[150]
pKD46	Expression vector of the phage λ Red recombinase for gene recombination with chromosomal genes in *E. coli*	[147]
pCP20	Plasmid with temperature-sensitive replication for temporal production of the Flp enzyme in *E. coli*, Amp^R and Cm^R	[151]

Table 5 - Continued from previous page

Plasmid	Relevant genotype	Reference or source
pHL1	FliN-YFP expression plasmid; pDK66 derivative	This work
pHL2	FliG-YFP expression plasmid; pDK66 derivative	This work
pHL4	YFP-FliN expression plasmid; pDK4 derivative	This work
pHL5	CFP-FliN expression plasmid; pDK2 derivative	This work
pHL6	FliN-CFP expression plasmid; pDK113 derivative	This work
pHL8	FliG-CFP expression plasmid; pDK113 derivative	This work
pHL13	FliN-CFP expression plasmid; pDK79 derivative	This work
pHL14	MotA-CFP expression plasmid; pDK79 derivative	[152]
pHL15	FliG-CFP expression plasmid; pDK79 derivative	This work
pHL16	CFP-FliN expression plasmid; pDK79 derivative	This work
pHL18	FliF-YFP expression plasmid; pDK66 derivative	This work
pHL22	FlhA-YFP expression plasmid; pDK66 derivative	This work
pHL23	DnaK-YFP expression plasmid; pDK66 derivative	This work
pHL24	HtpG-YFP expression plasmid; pDK66 derivative	This work
pHL25	FliI-YFP expression plasmid; pDK66 derivative	This work
pHL28	FliL-YFP expression plasmid; pDK66 derivative	This work
pHL29	FliJ-YFP expression plasmid; pDK66 derivative	This work
pHL30	FliH-YFP expression plasmid; pDK66 derivative	This work
pHL31	YFP-FliG expression plasmid; pDK4 derivative	This work
pHL37	FliO-YFP expression plasmid; pDK66 derivative	This work
pHL38	FliR-YFP expression plasmid; pDK66 derivative	This work
pHL39	FliP-YFP expression plasmid; pDK66 derivative	This work
pHL40	YFP-FliI expression plasmid; pDK4 derivative	This work
pHL41	YFP-FliJ expression plasmid; pDK4 derivative	This work
pHL42	YFP-FliL expression plasmid; pDK4 derivative	This work
pHL43	YFP-FliH expression plasmid; pDK4 derivative	This work
pHL49	CFP-FliG expression plasmid; pDK2 derivative	This work
pHL50	CFP-FliG expression plasmid; pDK79 derivative	This work
pHL52	HtpG(E34A)-CFP expression plasmid; pDK79 derivative	This work
pHL54	YcgR-YFP expression plasmid; pDK66 derivative	[152]
pHL55	YFP-YcgR expression plasmid; pDK4 derivative	[152]
pHL56	FlhB-YFP expression plasmid; pDK66 derivative	This work
pHL57	FlhA-CFP expression plasmid; pDK85 derivative	This work
pHL58	FlhA-CFP expression plasmid; pDK79 derivative	This work
pHL59	FliF-CFP expression plasmid; pDK113 derivative	This work
pHL60	FliF-CFP expression plasmid; pDK79 derivative	This work

Table 5 - Continued from previous page

Plasmid	Relevant genotype	Reference or source
pHL61	CFP-FliL expression plasmid; pDK2 derivative	This work
pHL62	CFP-FliL expression plasmid; pDK79 derivative	This work
pHL63	FRDA-YFP expression plasmid; pDK66 derivative	This work
pHL64	YFP-FRDA expression plasmid; pDK4 derivative	This work
pHL65	FRDB-YFP expression plasmid; pDK66 derivative	This work
pHL66	YFP-FRDB expression plasmid; pDK4 derivative	This work
pHL67	FRDC-YFP expression plasmid; pDK66 derivative	This work
pHL68	FRDD-YFP expression plasmid; pDK66 derivative	This work
pHL70	HtpG-CFP expression plasmid; pDK79 derivative	This work
pHL71	FliO-CFP expression plasmid; pDK113 derivative	This work
pHL72	FliO-CFP expression plasmid; pDK79 derivative	This work
pHL73	FliF expression plasmid; pTrc99 derivative	This work
pHL74	FlhA expression plasmid; pTrc99 derivative	This work
pHLe1	DnaK-CFP expression plasmid; pDK79 derivative	This work
pVS31	CFP-FliM expression plasmid; pBAD33 derivative	This work
pVS42	FliM-CFP expression plasmid; pBAD33 derivative	This work
pVS61	FliM-YFP expression plasmid; pTrc99a derivative	This work
pVS62	YFP-FliM expression plasmid; pTrc99a derivative	This work
pVS88	CheZ-CFP-CheY-YFP expression plasmid; pTrc99a derivative	[153]
pVS483	H-NS-YFP expression plasmid; pDK66 derivative	This work
pAV1	CheY-YFP-CFP-FliM expression plasmid; pTrc99a derivative	[152]

2.7 Experimental methods

2.7.1 Construction of Fluorescent protein fusions

Plasmids used to express fluorescent protein fusions are listed in Table 5. With the exception of previously described FliM fusions [144], all fusions were constructed by amplifying the target gene using PCR and cloning the PCR product into its respective fusion vectors pDK4, pDK66, pDK2, pDK85 or pDK113 [150]. These vectors allow expression of N- and C-terminal gene fusions of $eyfp^{A206K}$ and $ecfp^{A206K}$, which encode true monomeric versions of YFP and CFP respectively [154] under the control of the pTrc promoter inducible by isopropyl-ß-D-thiogalactoside (IPTG). CFP fusions were subsequently moved into the vector pDK79 under the control of pBAD promoter inducible by L-arabinose. Immunoblotting with a monoclonal GFP-specific antibody (JL8;

BD Biosciences) was used to confirm the expression of full-length fusion proteins.

2.7.2 Strains and their growth

Escherichia coli K-12 strains used in this study are listed in Table 3. VS116 (Δ*flhC*) was derived from RP437 [143, 150]. DFB228 (Δ*fliM*), DFB232 (Δ*fliM* Δ*fliN*) and DFB247 (Δ*fliM* Δ*fliG*) are from David Blair (Department of Biology, University of Utah, USA). HL2 (*fliF::kan*) was made as described previously [146] using primers HL100 and HL101 in Table 4. HL5 (*fliH::kan*), HL7 (*fliI::kan*), HL9 (*fliN::kan*), HL11 (*fliG::kan*), HL13 (*fliO::kan*), HL15 (*fliJ::kan*), HL17 (*fliL::kan*) HL19 (*motA::kan*) and HL21 (*flhA::kan*) were made by P1 phage transduction from the donor strains ECK1938 (*fliH::kan*), ECK1939 (*fliI::kan*), ECK1944 (*fliN::kan*), ECK1937 (*fliG::kan*), ECK1945 (*fliO::kan*), ECK1940 (*fliJ::kan*), ECK1942 (*fliL::kan*) ECK1891 (*motA::kan*) and ECK1880 (*flhA::kan*) [146] to recipient strain MG1655 [145]. HL3 (Δ*fliF*), HL4 (Δ*flhA*), HL6 (Δ*fliH*), HL8 (Δ*fliI*), HL10 (Δ*fliN*), HL12 (Δ*fliG*), HL14 (Δ*fliO*), HL16 (Δ*fliJ*), HL18 (Δ*fliL*) HL20 (Δ*motA*) and HL22 (Δ*flhA*) were made by transforming strains HL2 (*fliF::kan*), HL5 (*fliH::kan*), HL7 (*fliI::kan*), HL9 (*fliN::kan*), HL11 (*fliG::kan*), HL13 (*fliO::kan*), HL15 (*fliJ::kan*), HL17 (*fliL::kan*) HL19 (*motA::kan*) and HL21 (*flhA::kan*) respectively, with pCP20 to remove the kanamycin resisitance [147]. Strains LL14 (*fliM-cfp cheY-yfp*) and LL22 (*fliM-yfp*) were made using homologous allele exchange as described before [144].

Cells were grown in tryptone broth (TB; 1% tryptone and 0.5% NaCl) supplemented with ampicillin, chloramphenicol and/or kanamycin at final concentrations of 100, 35 and 50 μg/ml, respectively. Overnight cultures, grown at 30°C, were diluted 1:100 and grown at 34°C for about 4 h, to an OD_{600} of 0.45-0.5, in presence of the indicated levels of IPTG and arabinose. Cells were harvested by centrifugation (4,000 rpm, 5 min), washed once with tethering buffer (10mM potassium phosphate, 0.1 mM EDTA, 1 mM L-methionine, 67 mM sodium chloride, 10 mM sodium lactate, pH 7) and resuspended in 10 ml tethering buffer prior to fluorescence imaging, immunoblot analyses, FRAP or FRET measurements.

TB soft agar plates were prepared by supplementing TB with 0.3% agar (Applichem), 100 g/ml ampicillin and indicated concentrations of IPTG. Swarming was inoculated using fresh cells from LB agar plates. Swarm assays were performed at 34℃ for 6-8 hours. Following incubation, photographs of plates were taken with a Canon EOS 300D

(DS6041) camera. Images were analyzed with ImageJ (Wayne Rasband, NIH) to determine the diameter of the swarm rings.

2.7.3 Tethering assay

Tethering assay was performed essentially as described before [155]. Cells were grown as described above and 5 ml cells were resuspended in 1 ml tethering buffer. Flagella were sheared by passing the 1 ml volume of cell suspension back and forth between two syringes connected by thin polyethylene tubing. After shearing, cells were washed twice by centrifugation and resuspension in tethering buffer. 40 µl of the cell suspension was mixed with 20 µl anti-flagellin antibody (1:300 dilution) and placed into ethanol-cleaned tunnel slide. The tunnel slide was inverted and incubated in a humid chamber for 30-60 min. After washing out the non-attached cells with an excess of tethering buffer, fluorescence images of tethered cells were taken by Zeiss AxioImager microscope equipped with an ORCA AG CCD camera (Hamamatsu), a 100× NA 1.45 objective, and HE YFP (Excitation BP 500/25; Emission BP 535/30) filter set.

2.7.4 Fluorescence imaging

For microscopy, cells were applied to a thin agarose pad (1% agarose in tethering buffer). Fluorescence imaging was performed on a Zeiss AxioImager microscope equipped with an ORCA AG CCD camera (Hamamatsu), a 100× NA 1.45 objective, and HE YFP (Excitation BP 500/25; Emission BP 535/30) and HE CFP (Excitation BP 436/25; Emission BP 480/40) filter sets. Each imaging experiment was performed in duplicate on independent cultures. All images in one figure were acquired under identical conditions. Images were subsequently analyzed using ImageJ software (W. Rasband, http://rsb.info.nih.gov/ij/). To quantify fluorescence of individual motors (Figure 18), integral fluorescence of cell region containing the motor was measured and intensity of a nearby motorless cellular region of the same area was subtracted.

2.7.5 Quantification of protein expression

Mean expression levels of YFP fluorescent proteins were quantified in a population of approximately 10^4 cells as described before [156] using flow cytometry on a FACScan (BD Biosciences) equipped with a 488 nm argon laser. FACScan data were analyzed using CellQuestTM Pro 4.0.1 software. The absolute level of YFP expression was estimated using the calibration factor of 350 YFP molecules per FACS fluorescence unit,

which has been established previously [157]. Mean expression levels of CFP fluorescent proteins in single cells were quantified in microscopy images using ImageJ software. Absolute numbers were obtained using genomic *fliM-cfp* fusion as a reference and assuming that its expression level is identical to that of the genomic *fliM-yfp* fusion, which was quantified by FACS. Mean value of the autofluorescence background, measured for control cells, was subtracted from all values.

2.7.6 Immunoblot analyses

For quantitative immunoblot analyses, cells were grown and washed with the buffer as described above. Cells from 1.5 ml of suspension were harvested by centrifugation at 13,000 rpm for 1 min and resuspended in 150 µl tethering buffer. Upon addition of 50 µl 4× Laemmli buffer, sample was boiled for 10 min at 98°C and frozen at -20°C. Sample volumes were adjusted to the same amount of cells, estimated based on the OD_{600} value of the culture. Samples were separated using SDS-PAGE and transferred to the Hybond-ECL nitrocellulose membrane (Amersham Biosciences) using semidry blotter (Biometra) according to manufacturer's instructions. Membranes were blocked and hybridized as described before [144] using primary monoclonal mouse GFP-specific antibody (JL8; BD Biosciences) at 1:5,000 dilution. Secondary fluorescently labelled IRDye^{TM}700DX anti-mouse IgG goat antibody (Rockland) was used for detection at 1:10,000 dilution. Fluorescence signals from immunoblot were detected using an infrared LI-COR scanner (Odyssey) and signal intensities in individual bands were quantified using ImageJ.

2.7.7 Mass spectrometry assay

For mass spectrometry assay, cells were prepared as described above and concentrated 10 times in tethering buffer. Cells in 1 ml suspension were lysed by sonication in short bursts (3 × 10 second periods, 50% power) on ice. Cell debris was removed by centrifugation at 4 °C, 10,000 rpm for 20 mins and the membrane fraction was subsequently isolated by the ultracentrifugation at 4 °C, 100,000 g for 30 mins. The membrane pellet was resuspended in 20 µl 1× PBS buffer. 20 µl 50mM ammoniumbicarbonate solution with 8M urea (pH 8.5) were added in the membrane susupension and the mixture was incubated at room temperature for 20 mins. 4 µl of the mixture was taken out, mixed with 32 µl 50 mM ammoniumbicarbonate solution with 8 µg/ml Trypsin (Promega) and incubated over night at 28°C for digestion. The digestion was stopped with 4 µl acetic

acid and the membrane debris was removed from the sample by ultracentrifugation at 4 °C, 100,000 g for 30 mins. 25 µl sample was analysed by a nanoHPLC system (Eksigent 1D plus) coupled to a ESI LTQ Orbitrap mass spectrometer (Thermo Fisher).

Samples were loaded on a C18 trapping column (Inertsil, LC Packings) with a flow rate of 10 µl/min in 0.1% TFA. Peptides were eluted and separated on an analytical column (75 µm × 150 mm) packed with Inertsil 3 µm C18 material (LC Packings) with a flow rate of 200 nl/min in a gradient of buffer A (0.1% formic acid) and buffer B (0.1% formic acid, acetonitrile): 0-5 min: 3% B; 5-18 min: 3-40% B; 18-20 min: 60-90% B. The column was connected with a nano-ESI emitter (New Objectives). 1500 V were applied via liquid junction. One survey scan (res: 60000) was followed by 5 information dependent product ion scans in the LTQ. Only doubly and triply charged ions were selected for fragmentation. Product ion spectra were extracted by Mascot Distiller version 2.2.1.0. and grouped within a precursor m/z tolerance of 0.03 amu and with 5 intermediate scans at maximum. All MS/MS samples were analyzed using Mascot (Matrix Science; version 2.2.04). Mascot was set up to search the SwissProt database (selected for Escherichia coli, downloaded April 2010, 22664 entries) assuming trypsin as the digestion enzyme. Mascot was searched with a fragment ion mass tolerance of 0.50 Da and a parent ion tolerance of 4.0 ppm. Deamidation of asparagines and oxidation of methionine were specified in Mascot as variable modifications. Scaffold (Proteome Software; version 2.05.02,) was used to validate MS/MS based peptide identifications. Peptide identifications were accepted if they could be established at greater than 95.0% probability as specified by the Peptide Prophet algorithm [158]. Quantification was done from the mass spectra by generation of extracted ion chromatograms with a tolerance of 0.02 Da of the calculated m/z precursor values of identified peptides and the peak detection and quantification tools were provided with the instrument software QualBrowser version 2.0.7.

2.7.8 Studying protein binding kinetics by FRAP

Background

The dynamics of a fluorescent protein underlying the steady-state distribution can be assessed using a specific type of photobleaching technique called FRAP (Fluorescence Recovery After Photobleaching). Fluorescent molecules in a small region of the cell are irreversibly photobleached using a high-powered laser beam, and exchange between the

bleached and unbleached populations of fluorescent molecules is then monitored. In a typical FRAP experiment, a region is bleached once and then recovery of fluorescence in the bleached zone is monitored. Quantitative FRAP yields information about the relative mobility of the fluorescent molecules and their exchange at the macromolecular complexes, which is determined by the diffusion rate and binding interactions.

When diffusion is much faster than the kinetics of binding, it results in a diffusion-uncoupled FRAP recovery (Figure 9), where the recovery due to diffusion occurs first and recovery due to binding follows later. In this case, FRAP curve can be separated into two phases. In the initial diffusive phase, the fluorescence of freely diffusing molecules recovers. In bacteria, this phase lasts less than 1 s because diffusion itself is rapid and cells are small. Afterwards, exchange at binding sites occurs over a slower period of seconds to minutes (or longer), leading to the recovery of fluorescence corresponding to bound molecules. Thus, in the diffusion-uncoupled mode, the FRAP curve contains an extremely short initial diffusive phase, followed by a much longer binding phase. Consequently, most of the FRAP curve reflects the binding interactions, and much can be learned about binding by a simple inspection of the course of the recovery curve [159].

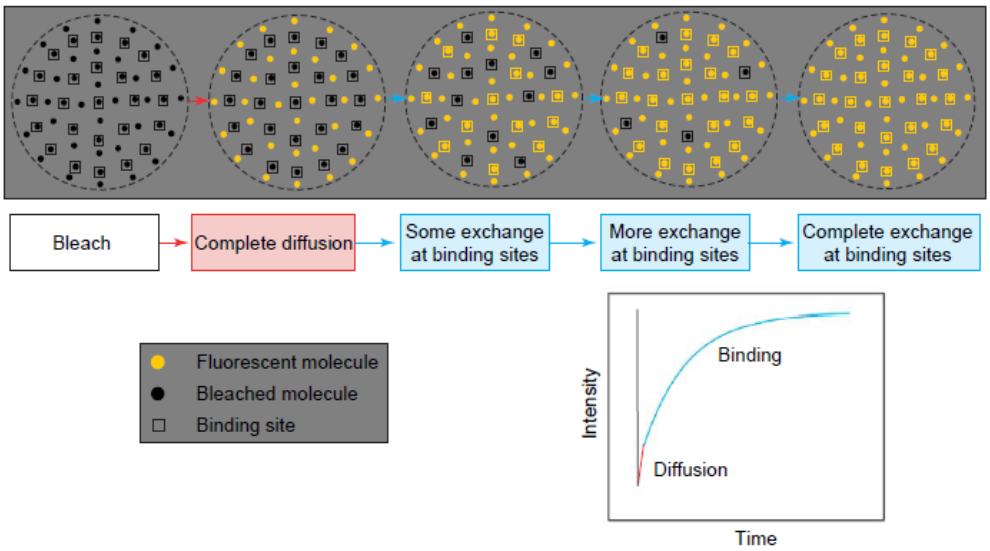

Figure 9: Diffusion-uncoupled FRAP behavior. After the bleach, fluorescent molecules rapidly diffuse throughout the bleach spot. Gradually, these bleached molecules dissociate from their binding site and rapidly leave the spot. Fluorescent molecules then replace the bleached molecules at the binding sites as they become vacant. The diffusion-uncoupled FRAP recovery curve consists of two separable components: the early recovery due to diffusion (red) and the slower recovery due to exchange at binding sites (blue). The figure is taken from [159].

FRAP measurement

FRAP measurements in this work were performed at 20°C on a DeltaVision RT microscope (Applied Precision) equipped with a YFP (Excitation BP 492/18; Emission BP 535/30) filter set, a 100× NA 1.4 objective (Olympus), a CoolSNAP HQ CCD camera (Photometrics), and a 20 mW argon laser, using softWoRx (Applied Precision) software with a FRAP module. Fluorescence of the ROI containing a motor was bleached for 1 s with 488 nm laser line at 10% maximal power; 1 prebleach image and 32 postbleach images sequences were acquired in 512×512 pixels format. Image analyses were subsequently performed using ImageJ software as described before [160].

2.7.9 Studying protein interactions by FRET

Background

To measure protein interactions *in vivo*, FRET (Fluorescence Resonance Energy Transfer) has been widely applied. FRET relies on the energy transfer between two fluorophores, whereby a donor fluorophore in its excited state can transfer energy by a nonradiative, long-range dipole-dipole coupling mechanism to an acceptor fluorophore in close proximity (typically <10 nm). This results in a decrease, or quenching, of the donor emission, and an increase, or sensitization, of the acceptor emission (Figure 10 B). A selection of fluorophore combinations, with the spectral overlap of the donor emission spectrum and the acceptor absorption spectrum, can be used to label proteins for FRET (Figure 10 A). Fusions to fluorescence proteins (FPs) provide a reliable and specific labelling, with cyan and yellow fluorescent proteins (CFP and YFP, respectively) being the most commonly used donor/acceptor pair [161]. A disadvantage of FPs, however, is their relatively large size, which does not allow their fluorescent centers to come into very close proximity, and thus lowers FRET efficiency. The efficiency of energy transfer (E_{FRET}) depends on the donor-to-acceptor separation distance R with an inverse 6^{th} power law due to the dipole-dipole coupling mechanism:

$$E_{FRET} = \frac{1}{1 + \left(\frac{R}{R_0}\right)^6} \qquad Equation\ 1$$

where R_0 is the Förster radius [162], the distance at which the energy is transferred with half-maximal efficiency. R_0 for the CFP/YFP pair in the bacterial cytoplasm is 49 Å (Figure 10 C), about the same size as the diameter of the FPs [12, 163]. The steep dependence of FRET on distance means that very little energy transfer takes place if the

fusions are farther apart than a critical distance of about 100 Å. This makes the probablity of energy transfer through random encounters of non-interacting proteins marginal, and essentially rules out false positive FRET signals. On the other hand, the steep dependence of FRET on the spacing between the FPs in a multiprotein complex can also lead to false negatives.

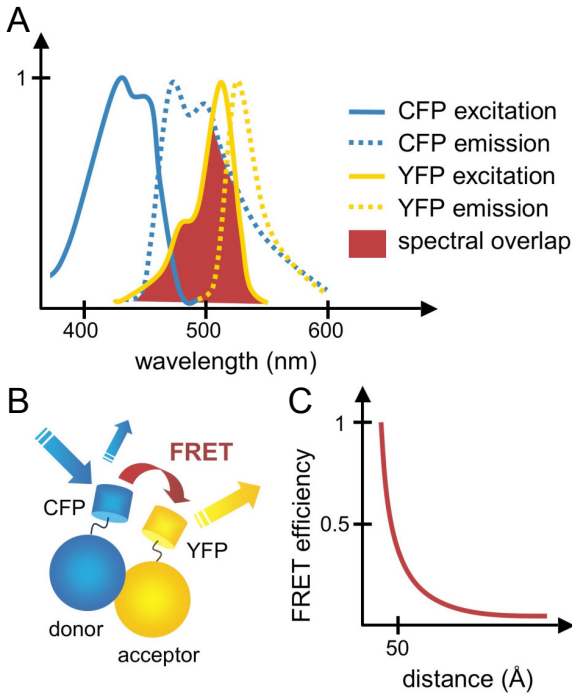

Figure 10: FRET between CFP and YFP. (A) Emission of the CFP donor overlaps with the excitation spectrum of the YFP acceptor. (B) Energy is transferred between two fusion proteins from an excited CFP to YFP. As a result, CFP emission decreases and YFP emission increases. (C) The efficiency of FRET is highly dependent on distance. For CFP and YFP, half-maximal FRET is achieved at a distance of 49 Å. The figure is kindly provided by Dr. D. Kentner.

There are several microscopic techniques for measuring FRET *in vivo*. Generally, one excites the donor fluorophore and monitors donor and/or acceptor fluorescence, or the lifetime of the excited donor, which is shortened by FRET [164]. A relatively simple way to quantify the absolute efficiency of FRET is to selectively photobleach the acceptor, which abolishes energy transfer and results in de-quenching of the donor. The increase in donor emission, calculated from the signal before (CFP_{before}) and after (CFP_{after}) bleaching, is a direct measure of the FRET efficiency:

$$E_{FRET} = 1 - \frac{CFP_{before}}{CFP_{after}} \qquad Equation\ 2$$

To study the dynamic protein interactions, the changes of CFP and/or YFP fluorescence

over time can be followed. In previous work, a system to measure FRET responses to chemotactic stimulation has been set up with FRET pairs CheY/CheZ or CheY/FliM [12, 165] and, in a similar way, to measure receptor/receptor interactions [166, 167]. In a typical experiment, cells expressing CFP and YFP fusions are stimulated with steps of different attractant concentrations, while continuously monitoring the YFP/CFP ratio, from which FRET can be calculated as

$$\mathrm{FRET} = \frac{\Delta R_{Max} - \Delta R}{\alpha + R_0 + \Delta R_{Max} - \Delta R} \qquad Equation\ 3$$

where ΔR is the change in the ratio due to energy transfer, ΔR_{Max} is the maximal change in the ratio to a saturating stimulus and R_0 is the ratio in the absence of FRET. The constant $\alpha = |\Delta YFP / \Delta CFP|$ is the absolute value of the ratio of changes in the fluorescence signal in YFP and CFP channels due to energy transfer, which is dependent on the respective sensitivities of CFP and YFP signal detection.

Acceptor photobleaching FRET measurement

FRET measurements by acceptor photobleaching were performed on a custom-modified Zeiss Axiovert 200 microscope as described before [168]. Briefly, cells expressing YFP and CFP fusions were concentrated about tenfold by centrifugation, resuspended in tethering buffer and applied to a thin agarose pad (1% agarose in tethering buffer). Excitation light from a 75 XBO lamp, attenuated by a ND60 (0.2) neutral-density filter, passed through a band-pass (BP) 436/20 filter and a 495DCSP dichroic mirror and was reflected on the specimen by a Z440/532 dual-band beamsplitter (transmission 465-500 and 550-640 nm; reflexion 425-445 and 532 nm). Bleaching of YFP was accomplished by a 20 sec illumination with a 532 nm diode laser (Rapp OptoElectronic), reflected by the 495DCSP dichroic mirror into the light path. Emission from the field of view, which was narrowed with a diaphragm to the area bleached by the laser, passed through a BP 485/40 filter onto a H7421-40 photon counter (Hamamatsu). For each measurement point, photons were counted over 0.5 s using a counter function of the PCI-6034E board, controlled by a custom-written LabView 7.1 program (both from National Instruments). CFP emission was recorded before and after bleaching of YFP, and FRET was calculated as the CFP signal increase divided by the total signal after bleaching (Equation 2).

Stimulus-dependent FRET measurement

In this work, CheY and CheZ were used as previously described [153] to monitor FRET responses to chemotactic stimulation. The FRET pair was expressed from the same

promoter on the plasmid pVS88, where *cheY* was fused to *yfp* and *cheZ* to *cfp*. The fusions to CheZ and CheY interact in a phosphorylation-dependent manner. Attractant inhibits the kinase, leading to a decrease in FRET. This decrease in FRET is observed as a decrease in YFP/CFP ratio due to the reduced numbers of CheY-P-CheZ complexes. Conversely, FRET increases upon removal of attractant. Hence, measuring the YFP/CFP ratio gives a direct readout of kinase activity. Similarly, another pair of proteins, CheY and FliM, was used as previously described [12].

Stimulus-dependent FRET measurements were performed on a custom-modified Zeiss Axiovert 200 microscope as described before [168]. Cells were concentrated about tenfold by centrifugation, resuspended in tethering buffer and applied to a poly-L-lysine-coated coverslip. After 10 min incubation at room temperature, cells were placed in a flow chamber, which was kept under constant flow (500 ml/min) of tethering buffer by a syringe pump (Harvard Apparatus). Excitation was through a BP 436/20 filter and reflected by a 455 dichroic mirror. Emission from a field of 300-500 cells passed through the 455 DC mirror, and was split by a 515 dichroic mirror into two signals, passing through a BP 485/40 cyan filter and a BP 535/30 yellow filter, respectively, on photon multipliers. A PCI-6034E counting board connected to a computer with LabView7/Template software was used for data aquisition as counts of detected photons per second. A stable YFP/CFP ratio was established after approximately 20 minutes (base line). By rapid exchange of the buffer reservoir, solutions of α-methyl-D,L-aspartate (MeAsp) in tethering buffer were added or removed. The change of YFP/CFP ratio was continuously monitored for 1-2 min. FRET was calculated from changes of YFP/CFP ratio by Equation 3, where the factor α is about 1.1 for the experimental set-up used in this work.

3 Results

3.1 Fluorescent protein fusions to flagellar motor and export apparatus proteins

3.1.1 Construction and functionality of fusions

In order to investigate the localization of flagellar motor and export apparatus proteins in *E. coli* cells, we constructed a number of yellow and cyan fluorescent protein (YFP and CFP, respectively) fusions to respective components (Tables 6 and 7). YFP/CFP and target proteins were fused with GGGSV or GSGGG linkers for N-terminal or C-terminal fusions, respectively [150]. The fusion genes were expressed from medium-copy number plasmids under the control of either pTrc or pBAD promoter, with induction levels being adjusted to give expression in the physiological range (Table 6). The extent of protein degradation at these expression levels was verified by immunoblotting (Table 6). Most fusions were stable, although strong degradation was observed for fusions to FlhB, FliP and FliR, which were therefore omitted from further analyses. The majority of stable fusions were functional, as assayed by their ability to complement the respective knock-out strains for swimming in liquid medium and for chemotaxis-driven spreading on soft agar plates (Table 7 and Figure 11). Exceptions were fusions to FliG that did not complement for swimming, and fusions to FliH and MotA, as well as the N-terminal fusions to FliN and FliM that complemented only for swimming but not for chemotaxis.

Table 6 Localization, expression level and stability of fluorescent fusions

YFP Fusions	Localization[a]		Induction level of IPTG (µM)	Expression level (×10^3 molecules per cell)[b]	Presence of full-length fusions[c] in *wt* strain	Percentage of degradation[c] in *wt* strain
	wt	Δ*flhC*				
FliF-YFP	+	–/+	1	3.4	+	26.5%
FliM-YFP	+	– (C)	10	2.4	+	9.2%
YFP-FliM	+	– (C)	10	2.8	+	14.1%
FliN-YFP	+	– (C)	0	4.7	+	0
YFP-FliN	+	– (C)	5	2.2	+	0.6%
FliG-YFP	+	– (C)	1	3.0	+	4.1%
YFP-FliG	+	– (C)	10	3.0	+	0
FlhA- YFP	+	+	10	3.3	+	13.9%
FlhB-YFP	– (C)	– (C)	30	2.0	–	100%
FliO-YFP	– (M)	– (M)	1	1.9	+	1.1%
FliP-YFP	– (C)	– (C)	20	1.8	–	100%
FliR-YFP	– (C)	– (C)	20	2.7	–	100%
FliH-YFP	+	– (C)	20	2.8	+	0
YFP-FliH	+	– (C)	30	2.2	+	14.3%
FliI-YFP	+	– (C)	20	3.7	+	1.2%
YFP-FliI	+	– (C)	10	3.3	+	18.8%
FliJ-YFP	– (C)	– (C)	50	2.2	+	21.1%
YFP-FliJ	– (C)	– (C)	5	1.4	+	3.8%
FliL-YFP	– (C)	– (C)	50	1.9	+	7.6%
YFP-FliL	– (M)	– (M)	10	1.9	+	9.7%
CFP Fusions	**Localization[a]**		**Induction levels of arabinose (%)**	**Expression levels (×10^3 molecules per cell)[b]**	**Presence of full-length fusions[c] in *wt* strain**	**Percentage of degradation[c] in *wt* strain**
	wt	**Δ*flhC***				
FliF-CFP	+	–/+	0.01	0.4	+	22.9%
FliM-CFP	+	– (C)	0.001	4.4	+	7.5%
CFP-FliM	+	– (C)	0.01	2.6	+	11.2%
FliN-CFP	+	– (C)	0.0005	12.8	+	0
CFP-FliN	+	– (C)	0.01	5.1	+	0
FliG-CFP	+	– (C)	0.001	6.0	+	0
CFP-FliG	+	– (C)	0.01	2.6	+	0
FlhA- CFP	+	+	0.001	2.9	+	9.4%
FliO-CFP	– (M)	– (M)	0.001	1.7	+	0.6%
MotA-CFP	– (M)	– (M)	0.001	4.0	+	0
CFP-FliL	– (M)	– (M)	0.01	3.5	+	4.3%

[a]Localization patterns were classified as follows:

+, Motor-like localization, with several discrete foci (up to 10) distributed more or less evenly along the cell periphery.

–/+, Poor localization, with only few and very weak foci.

– (M), Largely dispersed membrane localization.

– (C), Uniform cytoplasmic localization.

Images for each protein are shown in Figure12.

[b]Quantification of protein expression was performed as described in Materials and Methods.

[c]Determined by immunoblot as described in Materials and Methods.

Table 7 Functionality of fluorescent protein fusions

Swimming[a]				Swarming[b]			
Knock-out strain		**YFP fusion in knock-out strain**		**Knock-out strain**		**YFP fusion in knock-out strain**	
Δ*fliF*	–	FliF-YFP	+	Δ*fliF*	–	FliF-YFP	+
Δ*fliM*	–	FliM-YFP	+	Δ*fliM*	–	FliM-YFP	+
		YFP-FliM	+			YFP-FliM	+/–
Δ*fliN*	–	FliN-YFP	+/–	Δ*fliN*	–	FliN-YFP	–
		YFP-FliN	+			YFP-FliN	+ +
Δ*fliG*	–	FliG-YFP	–	Δ*fliG*	–	FliG-YFP	–
		YFP-FliG	–			YFP-FliG	–
Δ*flhA*	–	FlhA-YFP	+	Δ*flhA*	–	FlhA-YFP	+ +
Δ*fliO*	+	FliO-YFP	+	Δ*fliO*	+ +	FliO-YFP	+ +
Δ*fliH*	–	FliH-YFP	+	Δ*fliH*	–	FliH-YFP	–
		YFP-FliH	+			YFP-FliH	–
Δ*fliI*	–	FliI-YFP	+	Δ*fliI*	–	FliI-YFP	+
		YFP-FliI	+			YFP-FliI	+ +
Δ*fliJ*	–	FliJ-YFP	+	Δ*fliJ*	–	FliJ-YFP	+ +
		YFP-FliJ	+			YFP-FliJ	+ +
Δ*fliL*	+	FliL-YFP	+	Δ*fliL*	+ +	FliL-YFP	+ +
		YFP-FliL	+			YFP-FliL	+ +
Δ*motA*	–	MotA-YFP	+/–	Δ*motA*	–	MotA-YFP	–

[a] Complementation for swimming was defined by the swimming fraction as follows: –, non-motile; +/–, <50%; +, ≥50%.

[b] Complementation for swarming was defined by the ratio of the size of the outer swarm ring of the complementation strain to the size of the outer swarm ring of the wild-type strain (see Figure 11), as follows: –, <0.15; +/–, 0.15-0.5; +, 0.5-0.7; + +, >0.7.

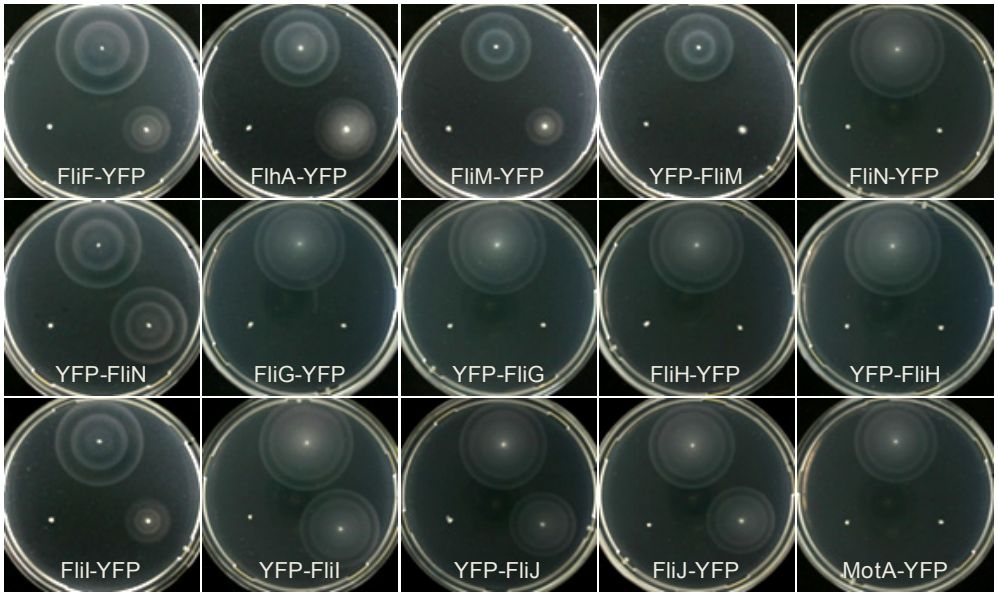

Figure 11: Soft-agar plate complementation assay for protein fusions. Plates were inoculated with parent wild-type (top) and the respective knock-out mutant (bottom left) cells carrying the empty vector, and with the knock-out mutant cells expressing an indicated fusion (bottom right). RP437 was used as wild type for FliM and MG1655 for all other protein fusions. Expression was induced by following levels of IPTG: 1 μM for FliG-YFP and MotA-YFP, 5 μM for YFP-FliJ, 10 μM for FliF-YFP, FlhA-YFP, YFP-FliM, YFP-FliI and YFP-FliG, 30 μM for FliM-YFP, YFP-FliN, FliN-YFP, YFP-FliH and FliH-YFP, and 50 μM for FliI-YFP and FliJ-YFP.

3.1.2 Background-dependent localization of fusions

We next investigated *in-vivo* localization of constructed fluorescent fusions in the wild-type strain background (Figure 12, Tables 6 and 8). Similar punctuate pattern of localization was observed for the membrane components FliF and FlhA and for the cytoplasmic components FliM, FliN, FliG, FliH and FliI, where up to 10 discrete foci were distributed more or less randomly along the cell periphery. Notably, fusions to FliG and FliH showed the same pattern of localization as other fusions, suggesting that they become efficiently incorporated into the motor assembly despite the defects in their functionality. FliO showed a largely dispersed membrane localization, consistent with the expectation that its copy number in a motor is small [18]. MotA-YFP showed a similarly dispersed membrane localization, possibly indicating that it was not efficiently incorporated in the motors when expressed separately from MotB and in a background of endogenous MotA. This result is consistent with its poor functionality and with previous biochemical analyses [4]. The punctuate distribution of most motor components reflects the previously observed pattern of motor localization [91, 144, 169], suggesting that these

structures indeed represent either fully or partially assembled motors distributed over the cell surface. Partially assembled motors, which could be distinguished by their high mobility in time-lapse experiments, represented a significant fraction of the observed fluorescent foci (~60%) for all fusions, consistent with the previous study for FliG [169]. Brighter fluorescent foci were observed at the poles of some cells, particularly for the fusions of the switch components FliM, FliN and FliG, as reported before [144, 169]. This apparent aggregation was not due to the protein overexpression, since the aggregates were present in the strain with the chromosomal *fliM-yfp* fusion (Figure 13 A). Formation of larger aggregates was previously observed for the native switch proteins in *Salmonella* cells [170]. Moreover, these aggregates include all switch proteins (Figure 13 B) and are dynamic as seen in FRAP experiments (Figure 13 C), suggesting that they could represent repositories of semi-assembled motors.

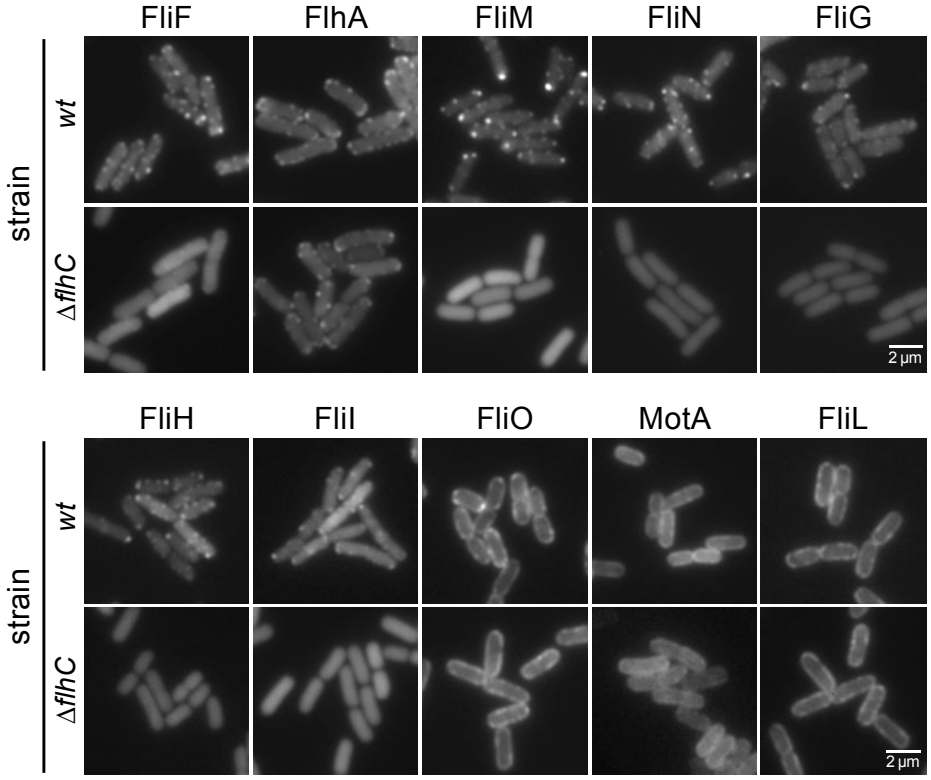

Figure 12: Localization of flagellar motor proteins. Fusions to YFP of indicated proteins were transformed into wild-type strain RP437 (*wt*) or into non-flagellated Δ*flhC* strain VS116. Induction levels of all fusions are summarized in Table 6.

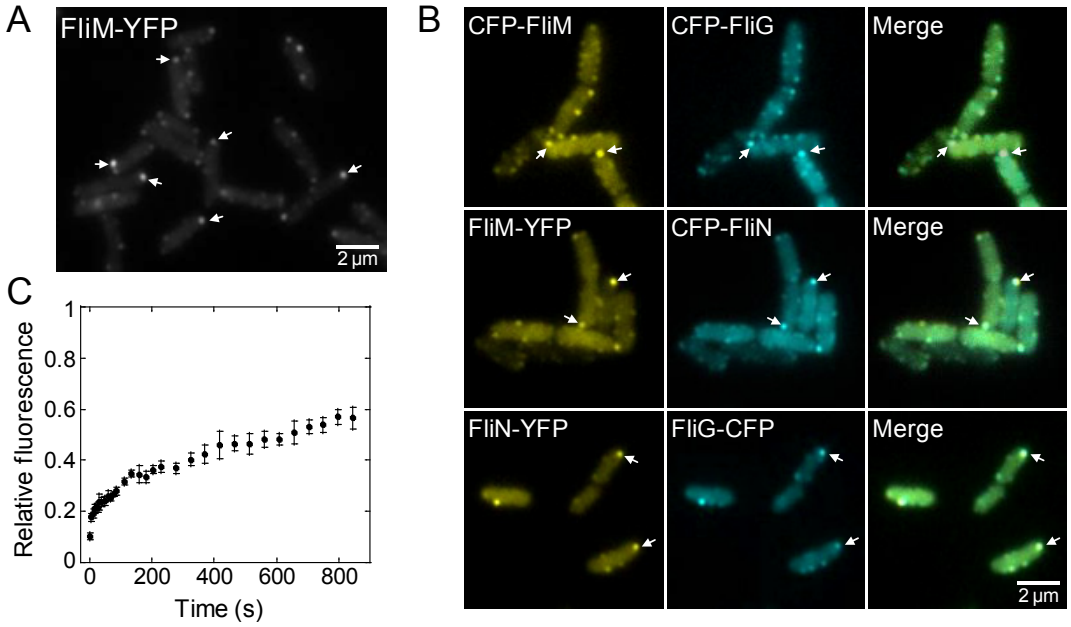

Figure 13: FliM-YFP localization and exchange at the large polar complexes. (A) Localization of FliM-YFP in strain expressing the fusion from the native chromosomal position of *fliM* gene. Large polar aggregates are indicated by arrows. (B) Colocalization of indicated YFP/CFP fusions to FliM, FliN and FliG (C) Kinetics of fluorescence recovery for YFP fusion to FliM at the large polar complexes in the wild type, measured by FRAP.

Confirming specificity of the localization observed in the wild type, most fusions did not show any punctuate localization in Δ*flhC* strain, which is deleted for the master regulator of flagellar gene expression and consequently does not synthesise any endogenous flagellar proteins (Figure 12). Surprisingly, poor localization was also observed for the MS-ring protein FliF, which has been previously postulated to nucleate the motor assembly (Figure 12). FliF thus appears to be unable to form stable oligomers in the absence of other flagellar motor proteins. The only protein that showed a clear motor-like localization pattern in Δ*flhC* strain was the export apparatus component FlhA (Figure 12), suggesting that it forms oligomers independent of other flagellar motor proteins and indicating that oligomerization of FlhA rather than of FliF might be the first step in flagellar motor assembly. Further investigation of protein localization in absence of individual flagellar proteins (Table 8 and Figure 14) confirmed that FlhA showed motor-like localization in all mutant strains. In contrast, FliF appears to require FlhA and other proteins for the normal oligomer formation, although residual localization was observed in any of the individual knockout strains, in agreement with a previous study [90]. FliG showed cytoplasmic localization in Δ*fliF* strain, meaning the assembly of the FliG complex requires FliF. Nevertheless, the localization of FliF was markedly reduced

in the absence of FliG and other switch components, indicating that the switch assembles after the MS-ring, but also in turn stabilizes the latter. Similarly, FliM assembly requires and stabilizes FliG localization to the motor. The assembly of the motor structures therefore appears to be cooperative rather than strictly sequential (see Discussion). FliN localization required both FliM and FliG, but not the cytoplasmic proteins of export apparatus, FliH and FliI. These latter proteins localized in cytoplasm in all mutant strains, indicating that they are the last to associate with the assembling cytoplasmic motor structure.

Table 8 Localization of selected fusion proteins in wild-type (*wt*) and knock-out strains[a]

Strain	Fusion						
	FlhA -YFP	FliF -YFP	YFP -FliG	YFP -FliM	YFP -FliN	YFP -FliH	FliI -YFP
wt	+	+	+	+	+	+	+
Δ*flhC*	+	–/+	– (C)	– (C)	– (C)	– (C)	– (C)
Δ*flhA*	+	+/–	+/–	+/–	+/–	+/–	+/–
Δ*fliF*	+	+	– (C)	– (A)	– (A)	– (C)	– (C)
Δ*fliM*	+	+/–	+/–	+	– (C)	– (C)	– (C)
Δ*fliM* Δ*fliN*	+	+/–	+/–	+/–	– (C)	– (C)	– (C)
Δ*fliM* Δ*fliG*	+	+/–	+/–	– (A)	– (C)	– (C)	– (C)
Δ*fliH*	+	+/–	+/–	+/–	+/–	– (A)	– (C)
Δ*fliI*	+	+/–	+/–	+/–	+/–	– (C)	+

[a]Localization patterns were classified as follows:
+, Motor-like localization, with several discrete foci (up to 10) distributed more or less evenly along the cell periphery (see Figure 12).
+/–, Suboptimal motor-like localization with fewer and less intense foci.
–/+, Poor localization, with only few and very weak foci.
– (C), Uniform cytoplasmic localization.
– (A), Cytoplasmic localization along with larger aggregates.
Representative images for each localization pattern are shown in Figure 14.

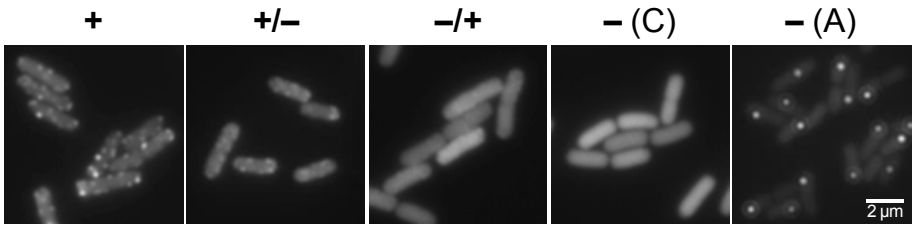

Figure 14: Examples of proteins localization patterns defined in Table 8. Localization of flagellar motor proteins was classified into 5 different patterns: +, represented by FliF-YFP in *wt* strain (See Figure 12); +/–, represented by FliF-YFP in Δ*fliM* Δ*fliN* strain; –/+, represented by FliF-YFP in Δ*flhC* strain (See Figure 12); – (C), represented by YFP-FliM in Δ*flhC* strain (See Figure 12); – (A), represented by YFP-FliM in Δ*fliF* strain.

3.2 Assembly of FliF oligomers is conditional

3.2.1 Assembly of FliF oligomers depends on the expression level

Assumption that the MS-ring is the first structure to assemble primarily came from the previous observation that FliF forms the MS-ring by self-assembly when it is overexpressed [91]. We therefore investigated the effects of expression level on the oligomerization of FliF-YFP (Figure 15 A). Indeed, while essentially no localization of FliF was visible in the Δ*flhC* strain at low induction levels, fluorescent foci could be observed at the highest levels of induction (30 to 100 μM IPTG). However, these expression levels were clearly unphysiological, corresponding to 30 to 50 thousands protein copies per cell. In contrast, FlhA-YFP localized well both in the wild type and in Δ*flhC* strain at all expression levels (Figure 15 B). A slightly better localization of FlhA-YFP in the wild type at the lowest expression level may be explained by the higher overall expression level of FlhA than in Δ*flhC* strain, due to the additional contribution of the endogenous protein, and/or by the additional stabilization of the FlhA oligomers upon assembly of subsequent motor structures. Overall, these results suggest that while FliF can potentially self-assemble into oligomers, it does so very inefficiently and only at high expression levels. In contrast, FlhA oligomerizes well at the physiological levels of expression, and its self-assembly is thus likely to represent the first step in the motor assembly.

3.2.2 FliF oligomerization is promoted by FlhA and FliG

Poor localization of FliF in Δ*flhC* and other mutant strains (Table 8 and Figure 14) suggests that the MS-ring formation is promoted by not only FlhA, but also by components of the switch complex and export apparatus. This later stabilization is most likely to be mediated by FliG, which directly interacts with FliF [109, 171] (see below) and itself requires FliF for assembly. To directly test this, FlhA-CFP or CFP-FliG was co-expressed with FliF-YFP in absence of other flagellar proteins, whereby expression levels of FlhA-CFP and CFP-FliG varied and the level of FliF-YFP was kept constant (Figure 16 A and B). Higher expression of either FlhA or FliG indeed induced FliF localization in a dosage-dependent manner, although neither of them was sufficient to bring the oligomer formation to the wild-type level. To verify the coassembly of FliF-YFP with FlhA-CFP, we investigated the colocalization of these proteins in more

detail (Figure 16 C). In the absence of other flagellar components, which anchor motors in the cell wall, many assemblies of FlhA and FliF showed high lateral mobility in the membrane. Therefore, faster imaging is required to investigate the colocalization of FliF-YFP and FlhA-CFP. We observed that while the number of FlhA-CFP foci was substantially higher than that of FliF-YFP foci, all the FliF-YFP foci localized to FlhA-CFP, consistent with our model that FlhA assembles first and recruits FliF. In contrast, despite its effect on the FliF oligomerization CFP-FliG itself remained almost exclusively cytoplasmic, even in presence of FliF. This observation indicates that FliG catalyzes the FliF oligomer formation rather than stabilizing it in a stoichiometric manner, and other switch components are required to stabilize the localization of FliG.

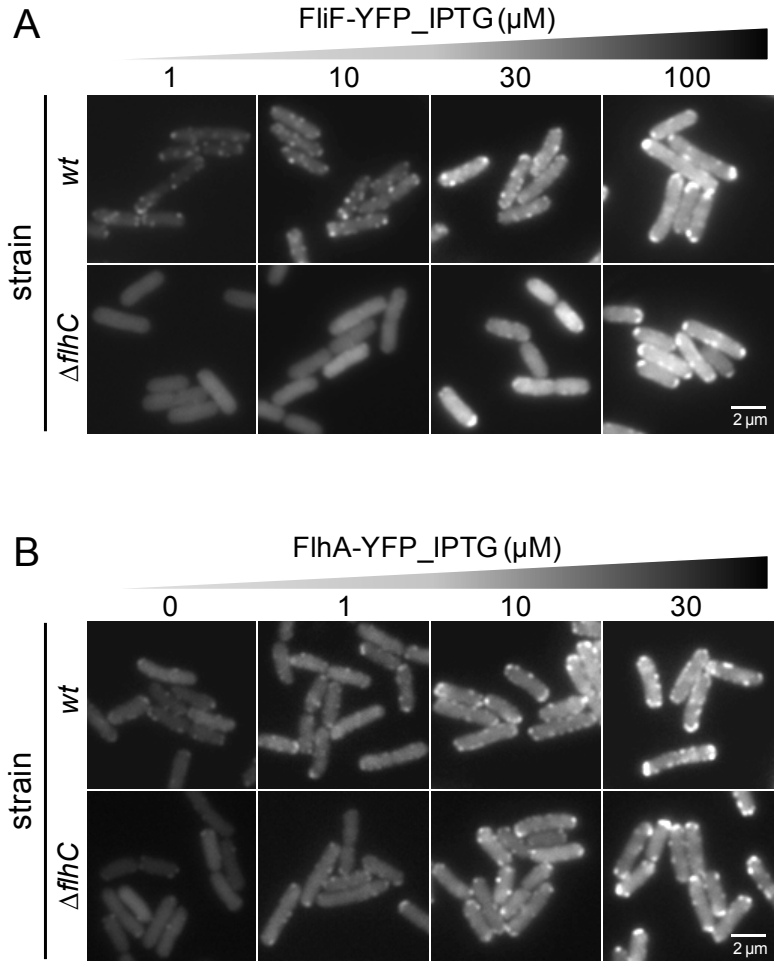

Figure 15: Dependence of FliF localization on expression level. Localization of FliF-YFP (A) and FlhA-YFP (B) at different induction levels in the wild type or in Δ*flhC* strain. The average expression levels ($\times 10^3$ molecules per cell) at a given induction, measured as described in Materials and Methods, were 3.4 (1 μM IPTG), 10.2 (10 μM IPTG), 27.8 (30 μM IPTG) and 49.5 (100 μM IPTG) for FliF-YFP; and 0.9 (0 μM IPTG), 1.0 (1 μM IPTG), 3.3 (10 μM IPTG) and 9.1 (30 μM IPTG) for FlhA-YFP.

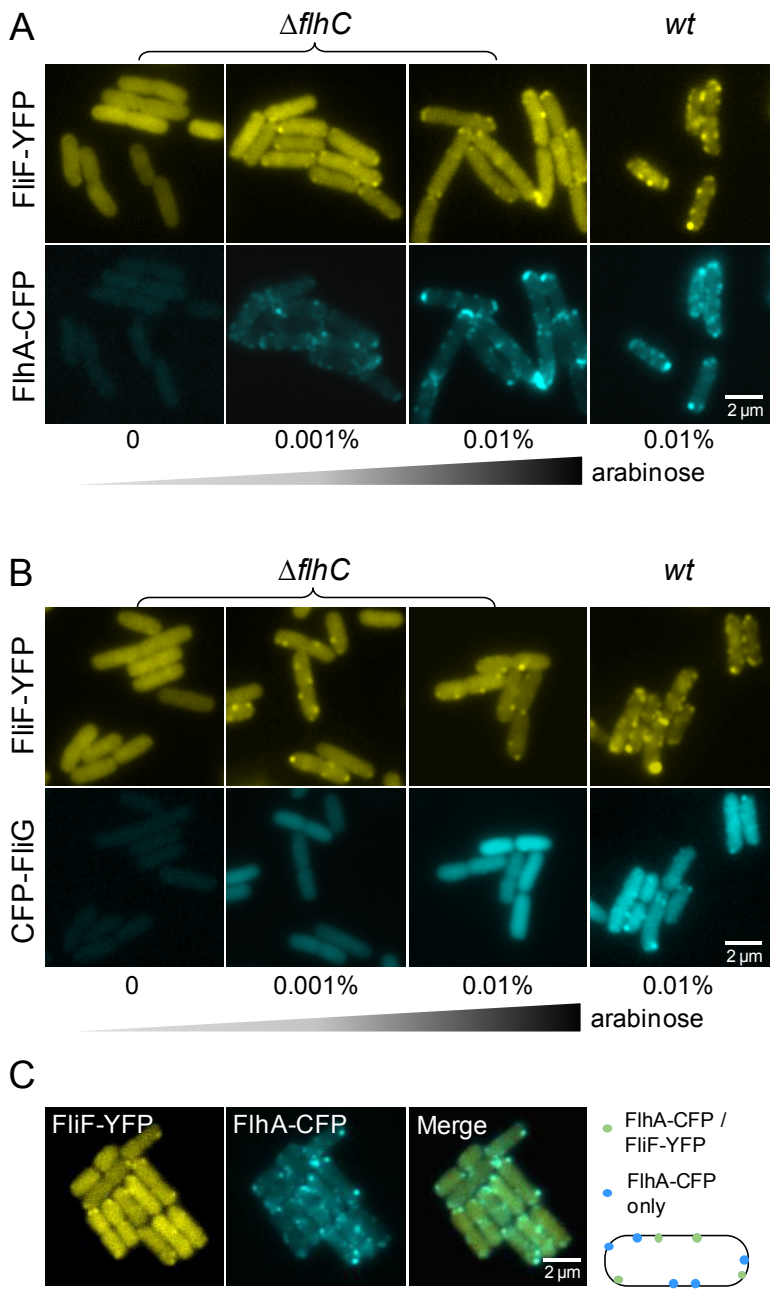

Figure 16: Promotion of FliF oligomerization by coexpression of FlhA or FliG. Localization of FliF-YFP in Δ*flhC* or in the wild-type cells coexpressing FlhA-CFP (A) or FliG-CFP (B) at the indicated levels of arabinose induction. Expression of FliF-YFP was invariably induced by 1 µM IPTG. (C) Colocalization of FliF-YFP (induced by 1 µM IPTG) and FlhA-CFP (induced by 0.001% arabinose) in Δ*flhC* strain. Images in CFP and YFP channel were taken at the highest time resolution allowed by our microscope and cell fluorescence, with a delay of about 1 sec. Cartoon illustrates the observed colocalization pattern.

3.3 FlhA stoichiometry at the motor

Relative brightness of the FlhA-YFP foci indicated that the number of FlhA subunits at the motor may be higher than the few subunits that would be expected to fit into the pore of the MS-ring [18]. To obtain a more precise estimate, we measured fluorescence intensity of FlhA-YFP foci corresponding to individual motors in Δ*flhA* background strain and compared it to similarly measured fluorescence intensities of FliM-YFP and FliF-YFP foci in respective knock-out strains (Figure 17 A). In all cases the intensity distribution for individual foci was relatively broad, despite the presumed fixed numbers of protein subunits in the assembled motors. This apparent variation is likely to be due to the imperfect localization of some fluorescent foci in the focal imaging plane, which would effectively reduce their intensity. Moreover, the number of photons collected from individual YFP molecules during image acquisition varies, and some YFPs may be in the non-fluorescent state during this time. However, these effects influence fluorescence of all fusions to the same extent, and relative values of mean intensities for different fusions must reflect their relative copy number at the motor. Consistent with that, the relative mean intensities of FliM-YFP and FliF-YFP foci were in good agreement with their known stoichiometry at the motor, 34 for FliM and 26 for FliF [24, 172-174]. Using these values as references allowed us to estimate that the copy number of FlhA at the motor is about 20 (Figure 17 B). Such number of FlhA subunits cannot be accommodated inside the MS-ring, suggesting that FlhA must localize outside it (see Discussion). We further confirmed that FlhA-YFP foci of this intensity correspond to functional motors, by showing their localization to the rotation axis of tethered cells (Figure 18).

A

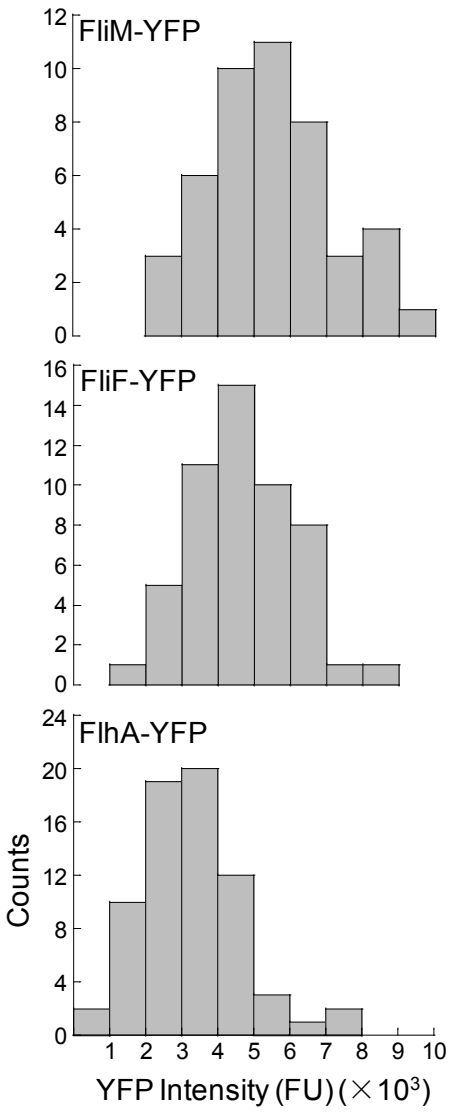

B

Reference (subunits)	Estimated FlhA number	
	Experiment1	Experiment2
FliM (34)	21	19
FliF (26)	18	20

Figure 17: Quantification of FlhA copy number. (A) Distribution of fluorescence intensities of FliM-YFP, FliF-YFP or FlhA-YFP at single motors, expressed in arbitrary fluorescence units (FU). The data are from one representative experiment. (B) Estimated copy number of FlhA-YFP molecules per motor from two experiments, using FliM-YFP or FliF-YFP as references. The copy number of FlhA was estimated as the mean fluorescence of FlhA foci divided by the relative fluorescence corresponding to a single YFP at the motor. The latter was calculated by dividing mean fluorescence of FliM-YFP or FliF-YFP foci by the expected number of subunits at the motor (shown in brackets). The calculations were performed independently for each experiment and fusion.

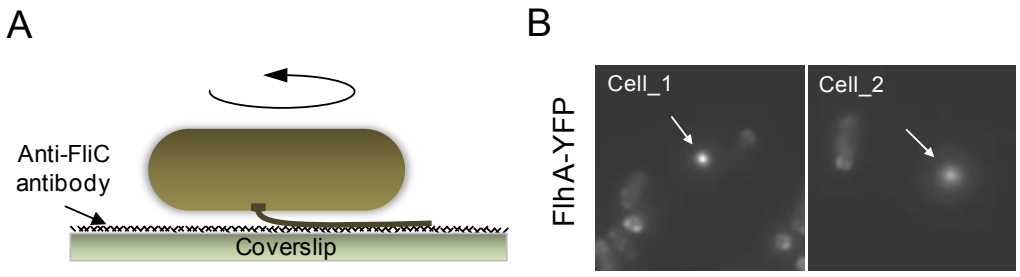

Figure 18: Fluorescent imaging of tethered FlhA-YFP cells. (A) Cartoon illustrating an antibody-mediated tethering assay of cell rotation. (B) Fluorescent images showing two rotating tethered cells that express FlhA-YFP as well as nearby stuck cells. Rotation axes of the tethered cells are indicated by arrows, with one FlhA-YFP spot at the motor that correspond to the centre of rotation in each tethered cell.

3.4 Complex formation enhances stability of FliF and FlhA *in vivo*

Surprisingly, we observed that FliF and FlhA fusions were significantly more stable against proteolysis in the wild-type background than in Δ*flhC* strain (Figure 19 A). This stability enhancement was specific for these membrane motor proteins, since control YFP fusions to the membrane chemoreceptor Tar and to FliG were not affected by the strain background. It indicates that the stability of FliF and FlhA is enhanced by assembly into the oligomeric complexes. The effect was particularly pronounced for the FliF fusion, in an apparent correspondence with its poor self-assembly in absence of other flagellar proteins. As another support for the hypothesis of assembly-dependent protection against degradation, stability of FliF-YFP was markedly improved by the coexpression of FliG or FlhA (Figure 19 B), both of which also promoted FliF oligomerization (Figure 16 A and B). FliF stability was also enhanced by its overexpression (data not shown). To confirm that the observed destabilization of FlhA and FliF in absence of assembled motors is not due to the influence of YFP fusions, we confirmed the result for the untagged proteins. Thereby FlhA and FliF were expressed in respective knock-out (Δ*flhA* for FlhA and Δ*fliF* for FliF) and Δ*flhC* strains and their levels were quantified using mass spectrometry (Figure 20). Mirroring our results for the fusion proteins, the amounts of FlhA and particularly of FliF were significantly higher when expressed in presence of other motor proteins.

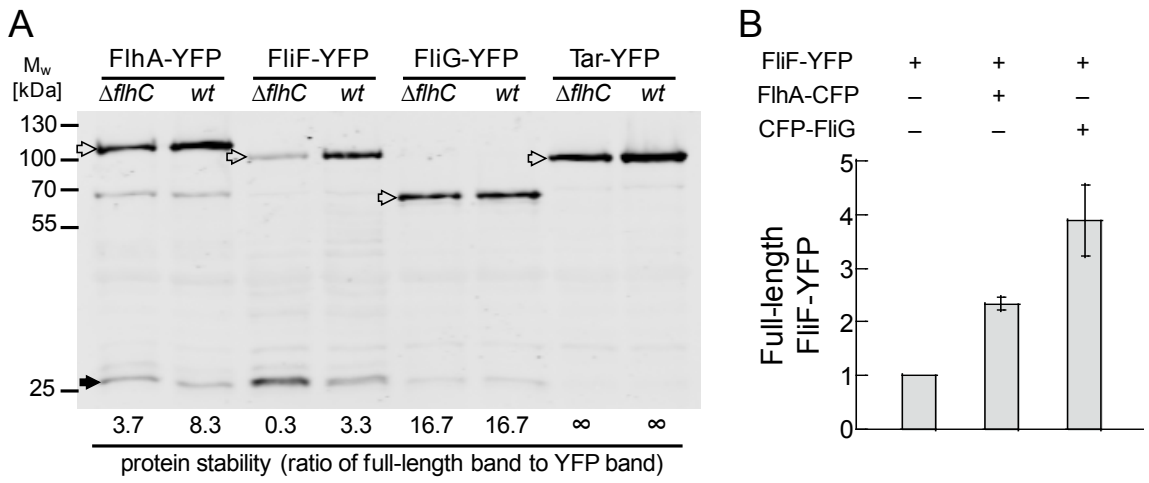

Figure 19: Assembly-dependent stabilization of FliF-YFP and FlhA-YFP against proteolitic degradation. (A) Extent of degradation of FliF-YFP and FlhA-YFP in Δ*flhC* strain or in the wild type. Full-length fusions to YFP (open arrows) and the degradation product corresponding to the size of monomeric YFP (solid arrow) were detected using immunoblot analysis with anti-GFP primary antibody. Fusions to a cytoplasmic motor component FliG and to a chemotaxis receptor Tar were used as controls. Expression was induced by 10 μM IPTG for FlhA-YFP and Tar-YFP and 1 μM IPTG for FliF-YFP and FliG-YFP. Similar total amounts of YFP were loaded in each lane, as quantified by the FACS-measured expression level of YFP and by the OD_{600} of the culture. Numbers underneath the blot indicate protein stability in corresponding lanes, defined as the ratio of full-length fusion band to the YFP band. (B) Stability of the full-length FliF-YFP fusion in Δ*flhC* strain is improved by the coexpression with FlhA-CFP or CFP-FliG. Samples with an identical total amount of YFP, as determined by FACS and by the OD_{600} of the culture, were evaluated by immonoblotting. The intensity of the full-length FliF-YFP band in each experiment was normalized to that in Δ*flhC* strain expressing only FliF-YFP. Error bars indicate standard errors.

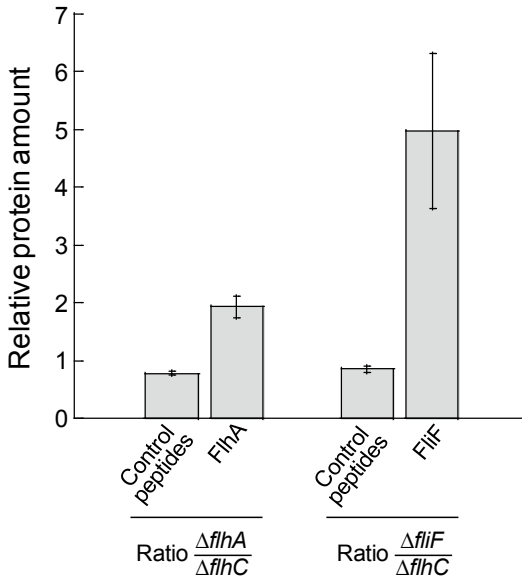

Figure 20: Assembly-dependent stabilization of untagged FliF and FlhA against proteolitic degradation. Relative abundance of untagged FlhA and FliF in the membrane fractions of a respective knock-out strain (Δ*flhA* for FlhA and Δ*fliF* for FliF) and in Δ*flhC* strain, measured by mass spectrometry. Expression was induced with 1 µM IPTG for FliF and 10 µM IPTG for FlhA. Peptides from three housekeeping membrane-localized proteins were used as control. Error bars indicate standard errors. See Table 9 for details.

Table 9 Mass-spectrometry quantification of FlhA and FliF in different strain backgrounds

Protein		**Peptide**[a]	**Relative abundance Δ*flhA*/Δ*flhC***	**Relative abundance Δ*fliF*/Δ*flhC***
Flagellar proteins	FlhA	GVEIGSGDAYPGR	1.8	
		LLAQTQEALSR	1.7	
		IAEVGAR	2.3	
	FliF	ALEGELSR		2.9
		TIETIGPVK		4.1
		EEVEDAVEVR		7.2
Controls[b]	ATP synthase subunit b, GN=atpF	(K)ASATDQLKK(A)	0.7	0.8
		(K)QVAILAVAGAEK(I)	0.8	0.9
		(R)SVDEAANSDIVDK(L)	0.9	0.8
	Outer membrane protein A, GN=ompA	(K)SDVLFNFNK(A)	0.7	1.0
		(K)GIKDVVTQPQA(-)	0.8	1.1
		(K)DGSVVVLGYTDR(I)	1.0	1.1
		(R)IGSDAYNQGLSER(R)	0.7	0.9
	2-oxoglutarate dehydrogenase E1 component, GN=sucA	(R)YSSTISDPDTNVK(Q)	0.7	0.7
		(R)ISTVPEAVEMQSR(V)	0.7	0.5
		(K)QQQDLVNDALNVE(-)	0.8	0.7

[a]The best-detected peptides were taken for quantification.

[b]Three housekeeping membrane-localized proteins were chosen as controls.

3.5 Measurements of proteins exchange at the functional motor

To investigate the stability of motor assembly, we performed FRAP experiments for YFP fusions to FliF, FlhA, FliM and FliH (Figure 21 A-D). In a typical FRAP experiment, fluorescence of the fusion protein of interest was bleached in a region of a cell (region of interest or ROI) that contained flagellar motor, and the recovery of fluorescence in the ROI was followed over time. Only assembled flagellar motors that were anchored in the cell wall and therefore immobile in the whole series of images were used for further analyses. Because bleached ROI always contained both cytoplasmic and motor-associated fusion proteins, the kinetics of fluorescence recovery showed two phases. The initial fast recovery resulted from a diffusion-driven exchange of the cytoplasmic fluorescent proteins in the ROI. The subsequent phase of slower recovery reflected the exchange of fusion proteins between the motor and the cytoplasm and was therefore fusion-specific. Although no recovery was observed for the motor-associated FliF fusion (Figure 21 A), we observed a slow recovery in all other cases. Motor-associated fusions to FlhA and FliM recovered to 50% of the initial relative fluorescence on the time scale of 10 min (Figure 21 B and C), whereas fusion to FliH showed even slower recovery, with the halftime of over 15 min (Figure 21 D). An overview of motor stability based on our work and on two recent studies [175, 176] is shown in Figure 21 E.

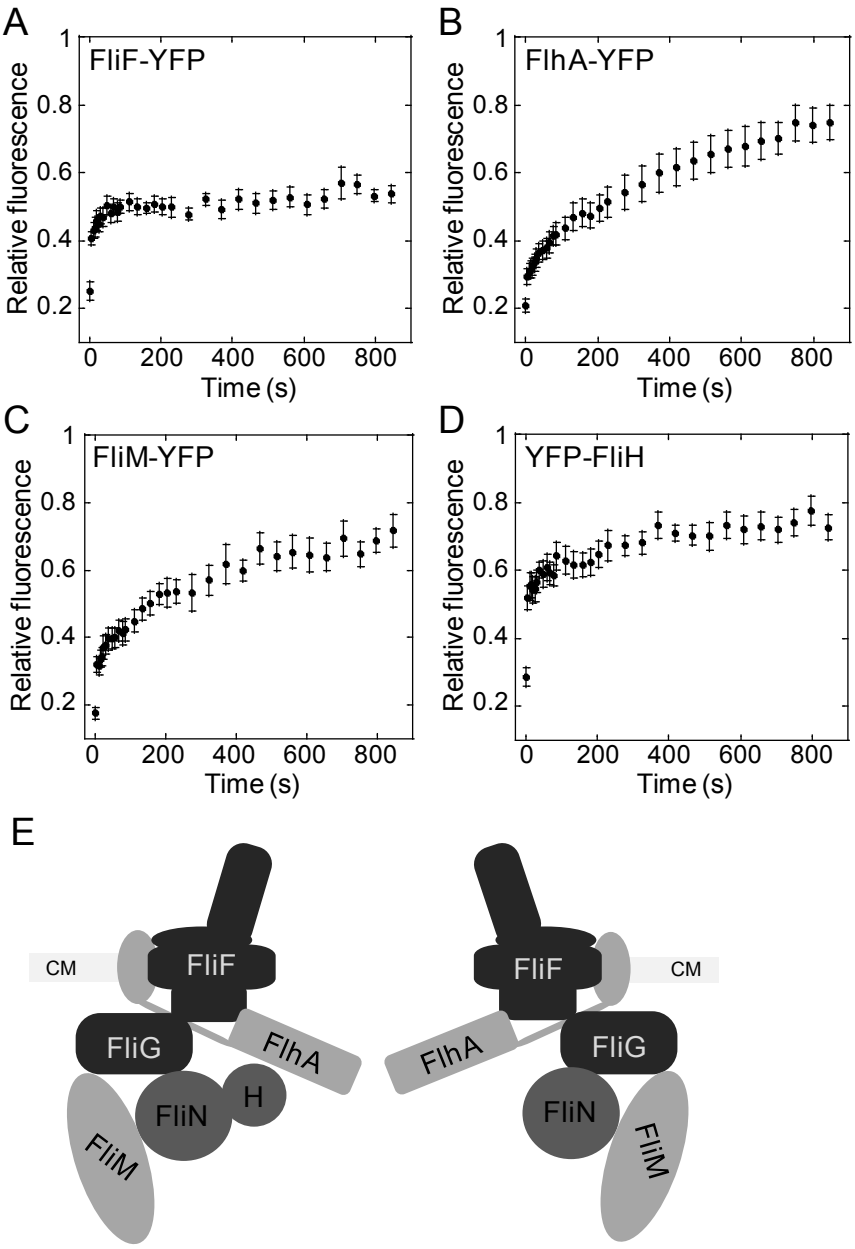

Figure 21: Protein exchange at flagellar motor. Kinetics of fluorescence recovery in FRAP experiments performed in wild-type cells expressing YFP fusions to FliF (A), FlhA (B), FliM (C) or FliH (D) for the ROI containing a cell-wall anchored flagellar motor. Error bars indicate standard errors. (E) Schematic representation of flagellar motor stability, including results of two related studies [175, 176]. Grayscale indicates stability of protein association with flagellar motor structure, with darker shading corresponding to more stable association.

3.6 FRET mapping of protein interactions at the motor

3.6.1 Interactions of motor proteins *in vivo*

To detect intracellular interactions of motor proteins, we measured FRET between CFP and YFP fusions using acceptor photobleaching [168] (Figure 22). FRET reports proximity of protein termini at distances of less than 10 nm, and therefore allows detecting both direct interactions and close proximities of proteins in the complexes. It is particularly useful to measure *in-vivo* interactions of membrane proteins, which are difficult to access otherwise.

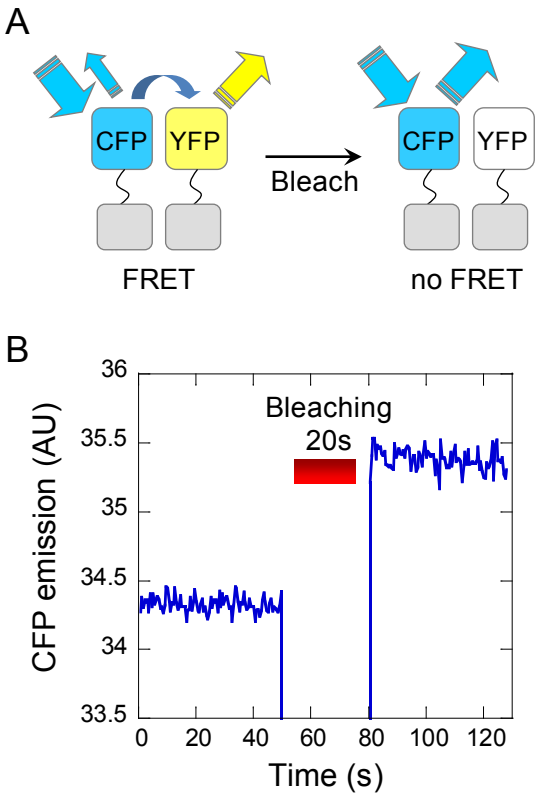

Figure 22: FRET measurement by acceptor photobleaching. (A) Cartoon illustrating FRET detection by acceptor photobleaching. FRET quenches emission of the CFP donor through energy transfer to the YFP acceptor. Bleaching of YFP eliminates FRET, causing an increase in CFP emission. (B) FRET experiment was performed for FliN-CFP/FliN-YFP pair expressed in Δ*flhC* strain. Positive FRET is seen as an increase in CFP emission upon bleaching of YFP for 20 sec using a 532 nm laser. Summary of FRET results is shown in Figure 23 A and in Tables 10 and 11.

We tested the interaction between pairs of proteins in the motor and export apparatus proteins for both wild type and Δ*flhC* strains (Figure 23 A, Tables 10 and 11). This experiment enabled us to distinguish between direct interactions, which do not depend on

other proteins, and close proximities in the assembled motor structure. Many FRET signals were indeed observed only in the wild-type background, but a number of direct interactions, which are expected to contribute to the motor assembly, were also detected. All direct interactions were consistent with our localization studies: FlhA interacts with itself and with FliF, and FliG interacts with FliF, FliM and FliN. At physiological expression levels, FRET signal between two FliF molecules was detected only in the wild type, confirming that FliF does not normally self-assemble. A direct interaction with itself could only be seen at extremely high expression levels of FliF (data not shown), again confirming locaization studies. Observed self-association of FliN, FliO and FliL might further contribute to the motor assembly. Moreover, we could confirm direct interactions of YcgR, H-NS, HtpG and FRDA with motor components, which may play a role in motor regulation and/or assembly.

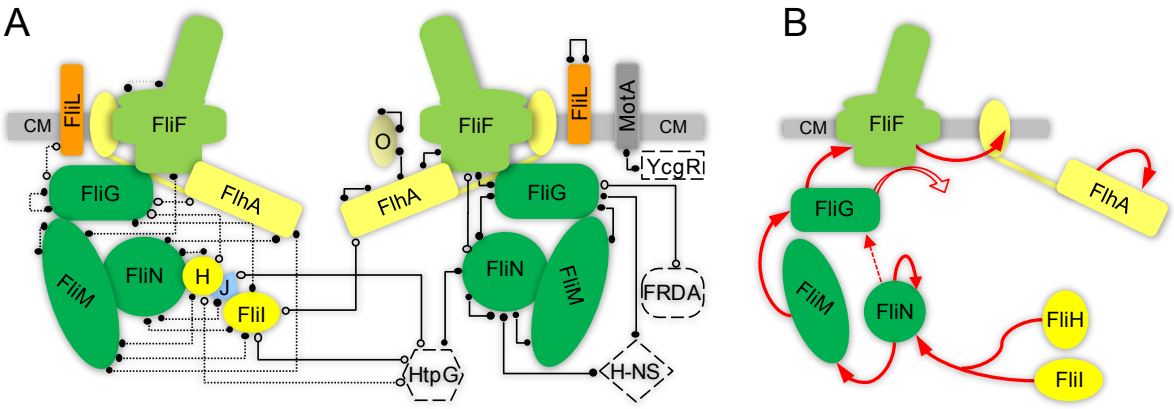

Figure 23: Interactome analysis and assembly of flagellar motor and export apparatus. (A) FRET-based interaction map of flagellar motor and export apparatus. The MS-ring and the switch complex are shown in green; the export apparatus is shown in yellow; FliJ is shown in blue; FliL is shown in orange; MotA is shown in dark grey; HtpG, H-NS, YcgR and FRDA are shown in white; cytoplasmic membrane (CM) is shown in grey. Interactions among proteins were measured by acceptor photobleaching, whereby FRET efficiency for individual pairs was determined as a fractional change in the CFP fluorescence upon YFP bleaching (see Tables 10 and 11 for the summary of FRET efficiencies). FRET pairs that were positive (FRET ≥ 0.5%) in Δ*flhC* strain indicate direct interactions (solid lines), while those positive only in the wild type reflect close protein proximity (< 10 nm) in the assembled motor (dotted lines). Positive pairs were further classified into weakly positive (open circles, 0.5%≤ FRET <1%) and strongly positive (filled circles, FRET ≥ 1%). Interactions involving DnaK, FRDB, FRDC and FRDD shown in Tables 10 and 11 were omitted for simplicity. (B) The proposed order of motor assembly, indicated by solid arrows. Open arrow indicates that FliG acts as a catalyst of FliF assembly. Dashed arrow corresponds to possible stabilization of FliG assembly by the direct binding of FliN.

Table 10 FRET mapping of protein interactions in wild-type strain RP437[a]

	FliM-CFP	CFP-FliM	FliN-CFP	CFP-FliN	FliG-CFP	CFP-FliG	FliF-CFP	FlhA-CFP	FliO-CFP	MotA-CFP	CFP-FliL	DnaK-CFP	HtpG-CFP
FliM-YFP	0.7± 0.44		0.73± 0.03										
YFP-FliM	0.62± 0.27	1.87± 0.82	1										
FliN-YFP			2.99± 0.35										
YFP-FliN	1.35± 0.37	3.1± 0.82	0.68	1.94± 0.17									
FliG-YFP	0	1.41± 0.15	0.4	1± 0.43	0.6± 0.01								
YFP-FliG	0	1.19± 0.3	0.46	0.89± 0.1	0	1.11± 0.12							
FliF-YFP	0.44	2.7± 0.11	0.81	0.68± 0.01	0	8.44± 0.13	2.98± 0.8	1.44± 0.11				0	0.4
FlhA-YFP	1.26	0.56± 0.04	0.72± 0.1	1.58± 0.09	0.25	0.67± 0.02		3.97± 2.7				0	0
FliI-YFP	1.23	1.26± 0.67	0	1.42	1.67		0	0.50± 0.2				0	0
YFP-FliI								0					0.54± 0.03
FliH-YFP	2.16± 0.04	5.93± 1.05	0.69± 0.5	1.27± 0.39	0.56		0	0				0.67± 0.07	0
YFP-FliH			1.03± 0.01	2.74± 0.12								0	0.9± 0.1
FliO-YFP	0	0	0	0	0	0	0	1.11± 0.28	7.1± 0.39			0	0
YFP-FliL	0	0	0	0	0	0.52	0	0			12.4± 0.54	0	0
FliJ-YFP	0	0.29	0	0.76± 0.29	0.35							0.62± 0.37	0
YFP-FliJ												0	0.52± 0.01
DnaK-YFP	0	0.75± 0.04	0.63	0.65± 0.05	0.3	0.63							
HtpG-YFP	0	0.4	1.1± 0.46	0.67± 0.15	0	0							
YFP-HtpG				0.65± 0.29									
YcgR-YFP	0	0	0	0	0	0				0			
YFP-YcgR	0	0	0	0	0	0				0			
H-NS-YFP	0	0	1.31± 0.05	1.27± 0.13	1± 0.01	0.6± 0.13							
FRDA-YFP					0.37	0							
YFP-FRDA					0	0.54± 0.03							
FRDB-YFP					0	0							
YFP-FRDB					0	0.59± 0.22							
FRDC-YFP					0	0							
FRDD-YFP					0	0							

[a]The mean of two to three experiments and a standard error are shown for most measured pairs. Data without error bar are from a single measurement, typically for pairs where FRET was already observed for the inverse

combination of YFP and CFP fusions. Empty cells correspond to pairs that were not analyzed, either because FRET was already observed for the inverse combination of YFP and CFP fusions or because no interaction was expected. FRET efficiency (E) for a given pair was determined as a fractional change in CFP fluorescence. We define $E \geq 1\%$ as strong FRET (blue), $0.5\% \leq E < 1\%$ as weak FRET (yellow) and $E < 0.5\%$ as negative (white). Note that the apparent FRET efficiency reported here is substantially lower than the theoretical FRET efficiency for the same pair, due to the signal reduction by cellular autofluorescence in the CFP channel.

Table 11 FRET mapping of protein interactions in Δ*flhC* strain VS116[a]

	FliM-CFP	CFP-FliM	FliN-CFP	CFP-FliN	FliG-CFP	CFP-FliG	FliF-CFP	FlhA-CFP	FliO-CFP	MotA-CFP	CFP-FliL	DnaK-CFP	HtpG-CFP
FliM-YFP	0		0.46										
YFP-FliM	0	0.25	0.79										
FliN-YFP			3.08										
YFP-FliN	0.53 ± 0.13	2.32± 0.03	0.82	1.84									
FliG-YFP	0	0	0	0.39	0					0			
YFP-FliG	0	3.36± 0.17	0.75± 0.06	1.19± 0.1	0	0				0			
FliF-YFP	0	0	0.67± 0.02	0	0	4.46± 0.22	0	1.4± 0.11		0		0.11	0.44
FlhA-YFP	0	0	0	0	0	0		3.4± 1.5		0		0	
FliI-YFP	0			0.2	0		0	0.5 ± 0.1				0	
YFP-FliI								0				0	0.57± 0.06
FliH-YFP	0	0	0	0			0	0				0	
YFP-FliH			0	0								0	0
FliO-YFP	0	0	0	0	0	0	0	2.03± 0.62	7.03± 0.42			0	
YFP-FliL	0	0	0	0	0	0	0	0		0	12.8± 0.32	0	
FliJ-YFP				0.11								0	
YFP-FliJ												0	0.5± 0.01
DnaK-YFP	0	0.75 ± 0.4	0.51± 0.06	0.4	0.37	0							
HtpG-YFP	0		1.46± 0.36		0								
YFP-HtpG													
YFP-YcgR										1.1± 0.03			
H-NS-YFP			1.22± 0.06	2.01± 0.09	0.54± 0.08	1.7± 0.07							
FRDA-YFP					0.21								
YFP-FRDA						0.51± 0.01							
FRDB-YFP													
YFP-FRDB						0							
FRDC-YFP													
FRDD-YFP													

[a]See Table 10 for labeling details.

3.6.2 HtpG interaction with flagellar motor and chemotaxis proteins

The observed interactions of HtpG with motor components indicate that it might be involved in bacterial motor assembly. Moreover, since Hsp90 in eukaryotes is frequently involved in assembly of signalling complexes, we speculated that HtpG may interact with components of the chemotaxis pathway. To further investigate the effects of HtpG on chemotaxis, soft-agar plate assay was performed with wild-type strain MG1655 and two genomic mutant strains, Δ*htpG* and *htpG*(E34A) in MG1655 (Figure 24). The *htpG*(E34A) is a point mutantion in the nucleotide binding domain of HtpG that slows down the ATP hydrolysis. Since ATP hydrolysis is necessary for the substrate release, HtpG(E34A) binds substrates more tightly. In order to induce higher expression of endogenous HtpG, experiment was performed at 39 °C in addition to 30 °C and 34 °C. At higher temperature, the *htpG*(E34A) mutant showed about 30% less efficient spreading than wild type (Figure 24), confirming that HtpG affects chemotaxis and/or motility.

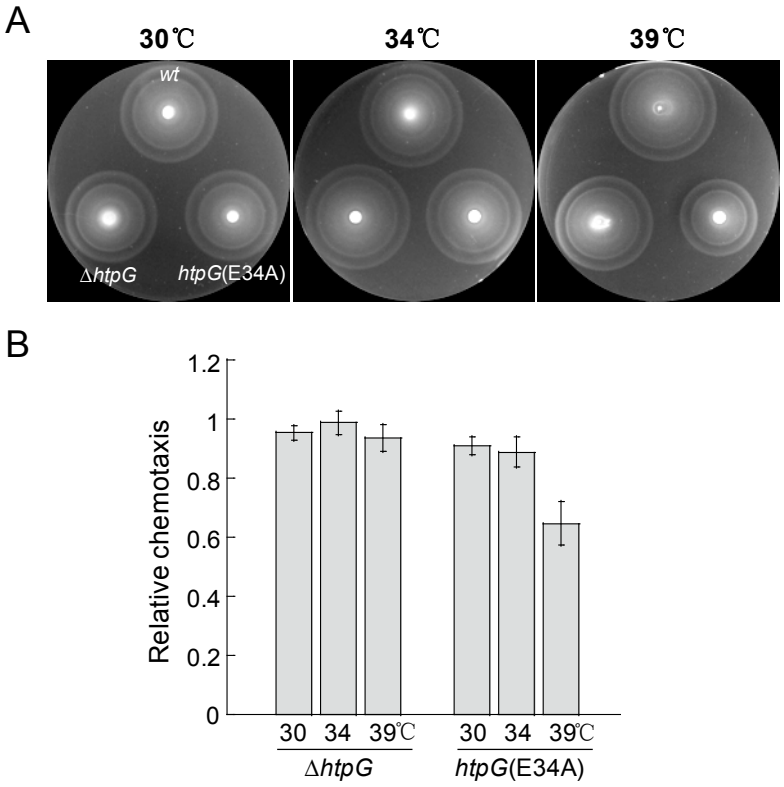

Figure 24: Soft-agar plate assay for wild type and Δ*htpG* and *htpG*(E34A) mutant strains. (A) Plates were inoculated with the same amount of wild-type MG1655 (top), the Δ*htpG* mutant (bottom left) and the *htpG*(E34A) mutant cells and incubated at indicated temperatures for 6 hr. (B) Relative chemotaxis of Δ*htpG* and *htpG*(E34A) mutants, compared to wild type, at indicated temperatures, quantified by the diameter of their swarm rings. Error bars indicate standard errors.

To investigate the effect HtpG on chemotaxis, the interactions of core chemotaxis proteins including Tar, CheA, CheB, CheR, CheW, CheY and CheZ with HtpG were tested by acceptor photobleaching FRET (Figure 25). HtpG(E34A) binds substrates more tightly than HtpG, so a stronger FRET signal is expected. Therefore, HtpG(E34A) instead of HtpG, was chosen for the initial screening for HtpG substrates *in vivo*. We found strong interactions of HtpG(E34A) with Tar, CheA and CheZ, all of which form either homodimers or heterodimers. Tar (Figure 25 B) forms homodimers that can be divided into a periplasmic ligand-binding domain and cytoplasmic signalling and adaptation domains, connected by a transmembrane segment. The interactions of HtpG(E34A) with Tar were mapped to the cytoplasmic signalling and adaptation domains (Figure 25 D). CheA forms homodimer and heterodimer co-existed *in vivo* [177], each of which consist of five functionally distinct domains (Figure 25 A and C): the phosphorylation domain P1 is autophosphorylated at His 48; the response regulator-binding domain P2 interacts with CheY and CheB; the dimerization domain P3 binds the partner monomer; the catalytic domain P4 phosphorylates P1 using ATP; the regulatory domain P5, which binds receptors and CheW, is required for regulation of kinase activity. The *cheA* gene contains an alternative start codon, from which a short protein version, $CheA_S$, lacking the first 97 amino acids is expressed (Figure 25 C). Our results showed that the P3 dimerization domain of CheA was required for the interactions with HtpG(E34A). Altogether, the results suggest HtpG interacts with oligomeric components of the chemotaxis pathway and could help the assembly of chemoreceptor clusters, but is not essential for chemotaxis.

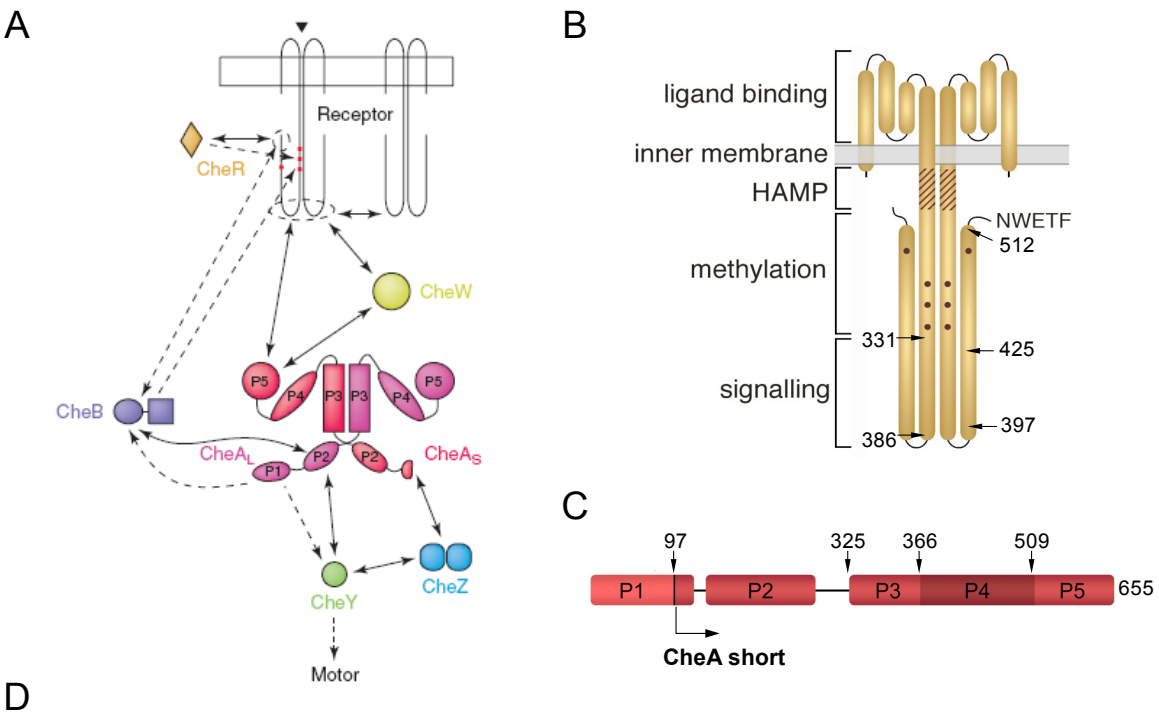

D

	HtpG(E34A)-FP	
	wt	Δ*flhC*
CheW-FP	++	-
FP-CheW	++	+
CheZ-FP	/	++
CheY-FP	/	+
CheR-FP	/	+
CheB-FP	/	+

	HtpG(E34A)-FP	
	wt	Δ*flhC*
CheA-FP	++	++
FP-CheA	+	-
FP-CheAs(97-655)	/	++
FP-CheA(325-655)	/	++
FP-CheA(366-655)	/	-
FP-CheA(509-655)	/	-

	HtpG(E34A)-FP	
	wt	Δ*flhC*
Tar-FP	/	-
Tar(1-512)-FP	/	++
Tar(1-425)-FP	/	-
Tar(1-397)-FP	/	-
Tar(1-386)-FP	/	+
Tar(1-331)-FP	/	+

Figure 25: Interactions of HtpG(E34A) with chemotaxis proteins. (A) Chemotaxis pathway. Receptors and CheZ are present as homodimers; $CheA_S$ and $CheA_L$ can form homodimer or heterodimer and are depicted as a heterodimer. (B) Organization of a receptor dimer. Ligands bind to the periplasmic receptor domain. Within the cytoplasmic domain, a HAMP region (shaded), a methylation and a signalling region can be distinguished. Methylation sites are indicated by filled circles. The NWETF sequence at the C terminal of major receptors serves as a tether for adaptation enzymes. Used truncated protein fusions are indicated by arrows. (C) Domain organization of CheA. Full-length $CheA_L$ is a 73 kD protein with five domains P1 to P5. $CheA_S$ misses the first 97 amino acids. Used truncated protein fusions are indicated by arrows. (D) FRET efficiency for indicated pairs measured by acceptor photobleaching FRET in *wt* and Δ*flhC* strains. FRET ≥ 1% is shown as strong FRET (++, blue), 0.5% ≤ FRET < 1% is shown as weak FRET (+, yellow) and E < 0.5% is shown as negative (-, white).

To further investigate whether HtpG directly affects activity of the chemotaxis pathway, activity of CheA in wild-type and genomic Δ*htpG* and *htpG*(E34A) mutant strains was measured *in vivo* by stimulus-dependent FRET, using the CheY-YFP/CheZ-CFP pair as a reporter. FRET of this pair is proportional to the concentration of phospho-CheY in the cell, which is a direct indicatior of kinase activity [153]. Upon stimulation with 100 µM α-methyl-D,L-aspartate (MeAsp), a saturating attractant stimulus that is known to inhibit kinase activity to zero, no significant difference in response between the wild type and the Δ*htpG* mutant was found at either 34 °C or 39 °C (Figure 26 C). However, 20% decrease of CheA kinase activity in *htpG*(E34A) mutant was observed at 39 °C (Figure 26 C). This result is consistent with the soft-agar plate assay (Figure 24), indicating that the effect of HtpG(E34A) on chemotaxis at higher temperature might be at least partly related to the reduction of kinase activity.

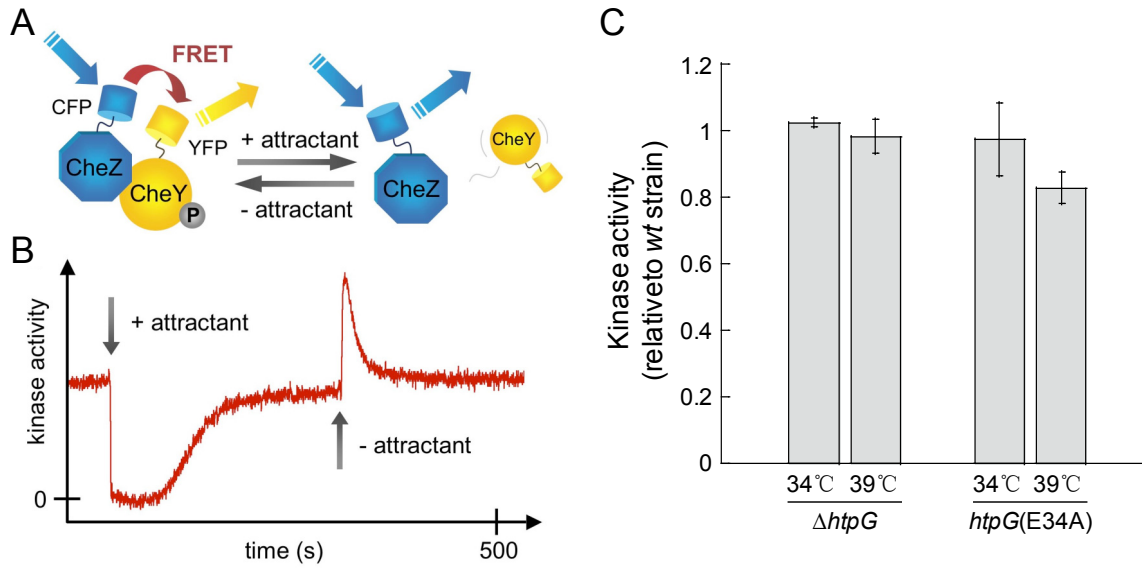

Figure 26: The *htpG*(E34A) mutant strain shows decreased kinase activity at 39 °C. (A) Stimulus-dependent FRET assay of the kinase activity using fusions to CheZ and CheY. Fusions to CheZ and CheY interact in a phosphorylation-dependent manner. Attractant inhibits the kinase, leading to a decrease in FRET. Conversely, FRET increases upon removal of attractant. (B) Time course of the FRET response to attractant addition and removal. The initial response down to zero kinase activity is followed by CheR/CheB-dependent adaptation to the pre-stimulus level of kinase activity. (C) Change in FRET between CheY-YFP and CheZ-CFP upon stimulation with a saturating concentration of attractant (100 µM MeAsp), measured in the wild-type, Δ*htpG* and *htpG*(E34A) mutant strains. FRET is an indicator of kinase activity. Cells were grown at different temperatures as indicated. Relative kinase activity was determined by normalizing the level of kinase activity in Δ*htpG* or *htpG*(E34A) mutant to the level in the wild type. Error bars indicate standard errors.

We further tested whether the overexpression of proteins that were shown to interact with HtpG could compensate for the chemotaxis defect in *htpG*(E34A) mutant strain on soft-agar plates. Expression of these proteins was induced gradually in both wild type and the *htpG*(E34A) mutant at 39 °C. The chemotaxis of each strain was quantified by measuring the diameter of the swarm ring. Chemotaxis of the same strains with an empty vector was used for normalization. The complementation was then quantified by calculating the relative chemotaxis of the *htpG*(E34A) mutant to wild type, represented as green lines for individual proteins (Figure 27). For FliN, Tar and CheA, the value of green line is above one, meaning positive complementation (Figure 27 A, C and E). However, neither of FliM nor Tsr showed complementaion (Figure 27 B and D), in agreement with an absence of their interaction with HtpG (Tables 9 and 10). Interestingly, overexpression of FliN promoted the chemotaxis in both wild-type and *htpG*(E34A) mutant strains, the mechanism of which needs to be further studied.

Next, we investigated the time course of HtpG interaction with FliN and CheA. Flagellar motors and chemoreceptor clusters are assembled at different time points, with the motor components being expressed and assembled earlier. If HtpG is involved in the assembly process of these structures, the interaction of HtpG with the two proteins should be temporally dynamic and correspond to the order of structure assembly. Indeed, the interaction of HtpG with $CheA_S$ peaked at OD_{600} 0.3, whereas the interaction with FliN peaked at OD_{600} 0.2 (Figure 28 A). Moreover, the interactions of HtpG(E34A) with both proteins were stronger and delayed compared to the binding of wild-type HtpG, consistent with the stronger binding of HtpG(E34A) to substrates (Figure 28 A). The peak of interaction of HtpG with FliN appears to correlate with the onset of cell motility, corresponding to the time when about 90% cells started swimming (Figure 28 B). Since the interactions of DnaK with some motor components were also observed in wild-type strain (Table 10), DnaK may be also involved along with HtpG in the structure assembly. For the Hsp70/Hsp90 chaperon machinery, substrates are delivered to the Hsp70 complex via Hsp40, and then enter the Hsp90 pathway. In *E. coli*, Hsp40 proteins are DnaJ and its homologue CbpA. Consistent with that, the interactions of HtpG with FliN or CheAs disappeared in the Δ*cbpA* Δ*dnaJ* strain (data not shown), suggesting that FliN and CheA are indeed delivered by DnaJ and CbpA to DnaK and then to the HtpG machinery.

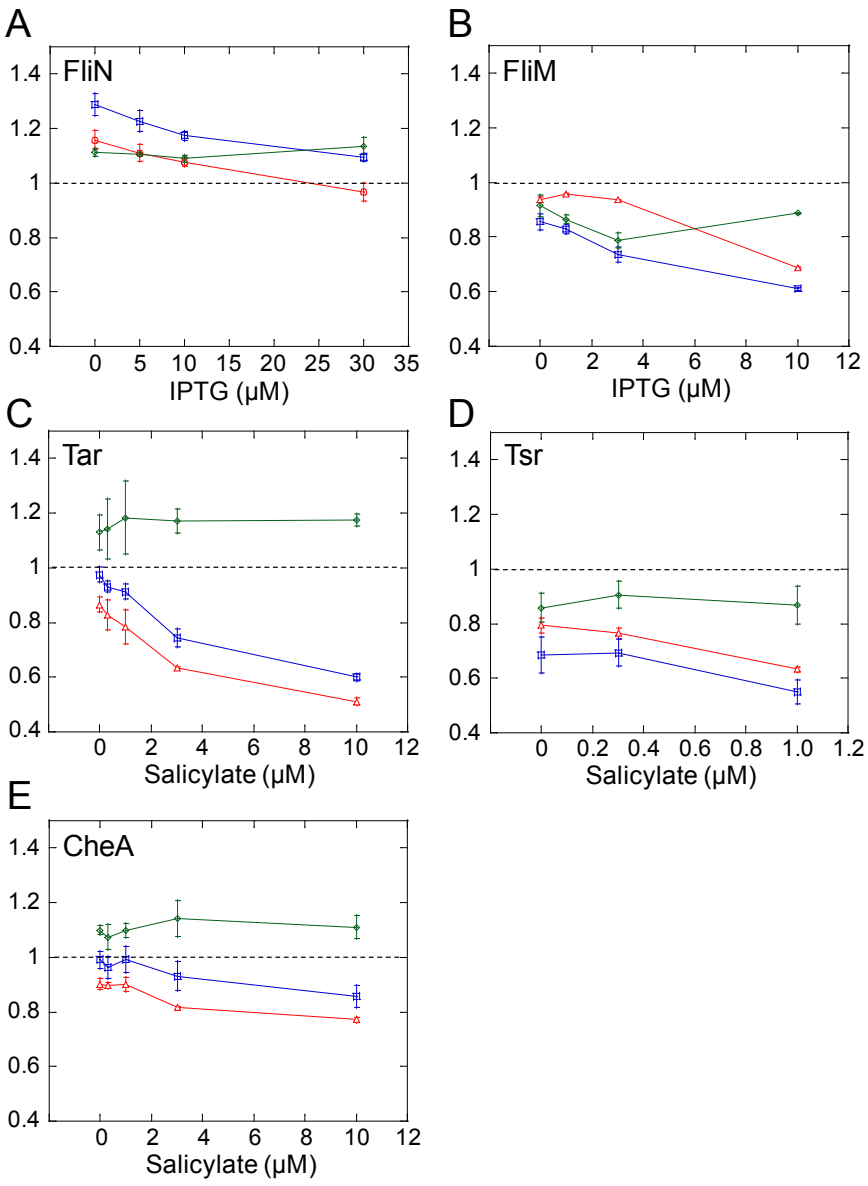

Figure 27: Complementation of chemotaxis defect in *htpG*(E34A) mutant by expression of flagellar and chemotaxis proteins. Indicated proteins were expressed at different levels above the endogenous levels in the wild type and *htpG*(E34A) mutant at varying induction of IPTG or salicylate (vector means no overexpression). Soft-agar plate assay was performed at 39 °C and the chemotaxis of each strain was quantified by measuring the diameter of its swarm ring. The chemotaxis of each strains was normalized to the strains with empty vector, represented as red line for wild type and blue line for *htpG*(E34A) mutant, respectively. The complementation of chemotaxis defect in *htpG*(E34A) mutant was then quantified by further dividing chemotaxis of *htpG*(E34A) mutant by that of the wild type, represented as green line. The value of green line above one indicates positive complementation. Error bars indicate standard errors.

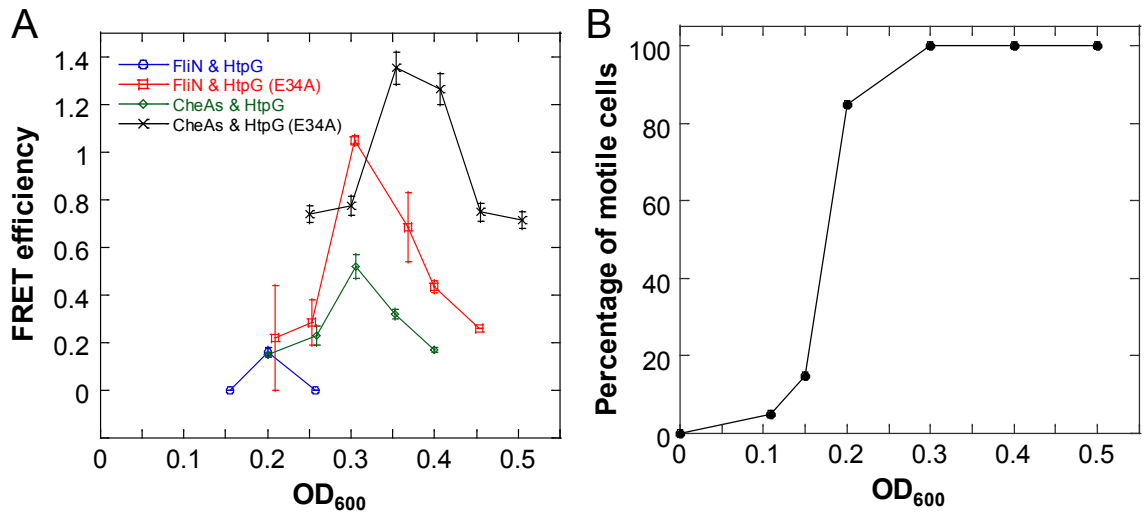

Figure 28: Growth-stage dependence of interaction of HtpG with FliN and CheAs. (A) Efficiency of FRET between HtpG-YFP or HtpG(E34A)-YFP and FliN-CFP or CFP-CheAs as a function of growth stage (indicated by OD_{600} value), measured by acceptor photobleaching. The measurements were performed on the same day. Error bars indicate standard errors. (B) Growth-stage dependence of motility. Percentage of motile cells at different growth stages (indicated by OD_{600} value) was estimated from the microscopy movies of swimming cells. The experiment was performed in derivatives of RP437 strain, which are non-motile above 37°C. Cells were grown over night in TB medium at 37 °C to completely inhibit their motility. After diluted in fresh TB medium to OD_{600} 0.01, cells were grown at 34 °C for measurements.

3.6.3 YcgR interaction with flagellar motor

To explore how YcgR controls motility, spontaneous motile suppressors of the Δ*yhjH* mutant were isolated by the Jenal's group in Basel. This approach is based on the idea that specific mutations in the direct molecular target of YcgR could disrupt this interaction thereby rendering the target blind for high levels of c-di-GMP. Four different suppressor mutations altering two specific residues of the stator protein MotA were isolated several times independently [152]. Three suppressors had exchanged glycine 93 to glutamate, valine, or arginine, respectively, while one suppressor had replaced serine 96 to leucine (Figure 29 A). G93 and S96 are in the immediate vicinity of two highly conserved residues of MotA (R90 and E98) that are involved in electrostatic interactions with conserved residues (D289, D288, and R281) of the rotor protein FliG (Figure 29 A) [178]. This MotA-FliG interaction is believed to be crucial for torque generation of the flagellar motor. All four motA mutations caused strong suppression of the Δ*yhjH* motility defect in motility test plates, with swarm sizes ranging from 68% to 82% of the WT swarm sizes (Δ*yhjH* shows swarm sizes below 40% of the WT, Figure 30). When the swimming speed of individual cells of these four suppressor mutants was analyzed with the help of video tracking, differences between the mutants became apparent. The *motA*(G93E) mutant displayed WT speed, the *motA*(G93R) mutant intermediate speed, and the *motA*(G93V) and *motA*(S96L) mutants Δ*yhjH*-like swimming velocities (Figure 29 B). Since all four suppressors performed well in motility plates, we speculate that *motA*(G93V) and *motA*(S96L) might only display their enhanced swimming capability at increased viscosity, conditions that more closely mimic the situation on motility plates. Indeed, when medium viscosity was increased by the addition of Ficoll (10%), all suppressor mutants showed higher swimming speeds than the Δ*yhjH* mutant, albeit not reaching the values of WT cells under these conditions (Figure 29 B). Thus, the differences in swimming velocity between the Δ*yhjH* mutant and the motile suppressors are more pronounced under conditions of increased viscosity. Although these results suggest that c-di-GMP and YcgR control swimming speed, we wanted to test the possibility of a direct effect of c-di-GMP on chemotaxis. For this, we used *in vivo* FRET measurements to quantitatively probe the stimulation-dependent interaction between CheY-YFP and the switch complex protein CFP-FliM. No significant difference in the response amplitude was observed between the WT and the Δ*yhjH* mutant (Figure 31), providing additional support for the idea that c-di-GMP governs cell motility primarily by

modulating swimming velocity rather than by affecting binding of CheY to FliM.

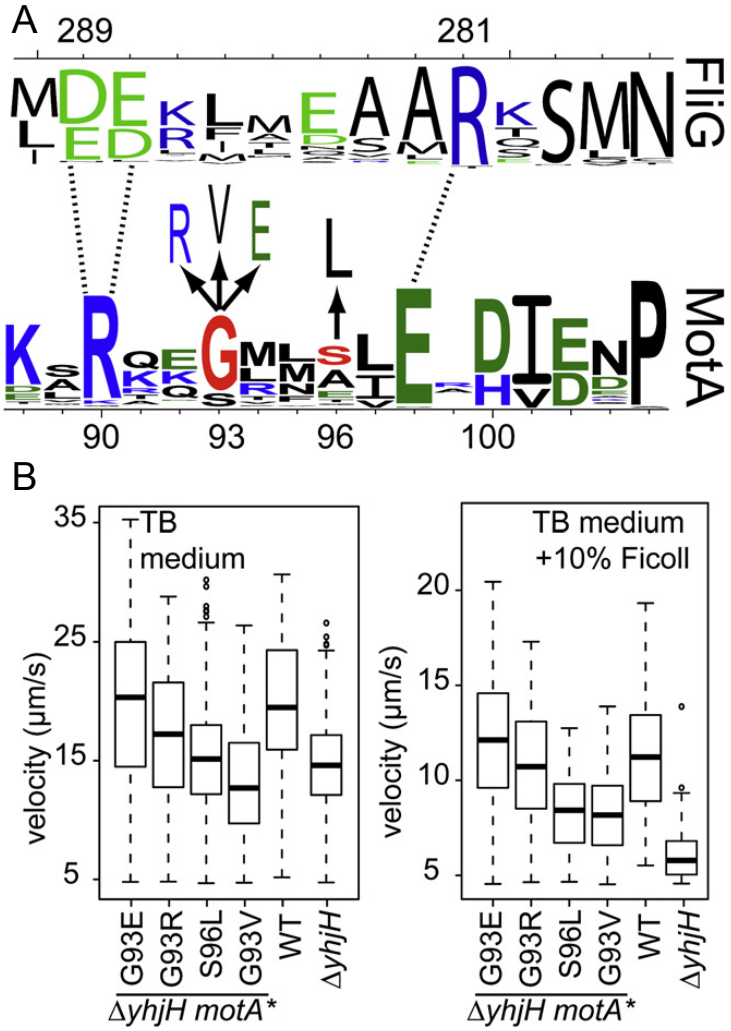

Figure 29: Mutations in MotA facilitate swimming at high c-di-GMP concentrations. (A) Motile suppressors carry exchanges in the FliG-MotA interface. A''Weblogo'' [179] representing sequence conservation among several hundred MotA and FliG homologs is shown. Numbers are according to the E. coli sequences, with positive (blue) and negative charges (green) highlighted. Residues exchanged in the motile suppressors are indicated in red. Dashed lines indicate postulated electrostatic interactions between stator (MotA) and rotor (FliG) residues [178]. (B) The swimming velocities of suppressor mutants and control strains were recorded at different viscosities (with and without 10% Ficoll). The velocity of the Δ*yhjH* mutant is significantly different from the velocities of all other strains at high viscosity (right). At low viscosity, the velocities of the suppressors harboring the S96L and G93V alleles are not significantly different from the Δ*yhjH* mutant (left). The figure is taken from [152].

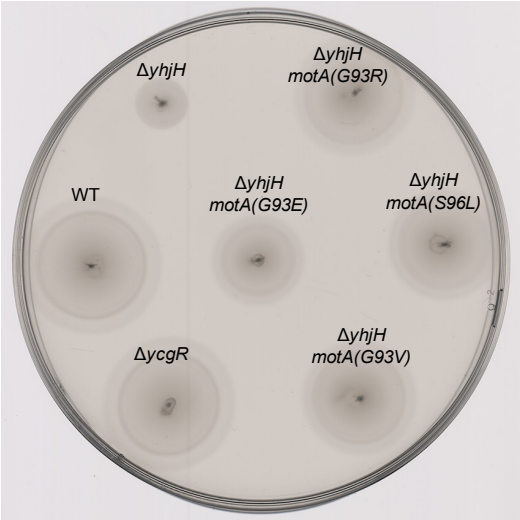

Figure 30: Suppressor mutants perform well in the soft-agar plate. Motility behaviour of the four suppressor mutants is compared to wild type, a Δ*yhjH* and a Δ*ycgR* mutant in tryptone motility test plates (plate diameter = 150 mm, incubation time ca. 7h at 7°C). The figure is taken from [152].

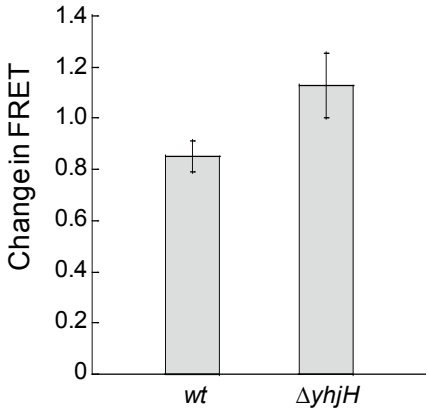

Figure 31: The Δ*yhjH* mutant shows normal interaction of CheY-P and the switch FliM. Change in FRET, expressed as % fractional change of CFP fluorescence, between CheY-YFP and CFP-FliM for the wild type and Δ*yhjH* mutant upon saturating stimulation with 30µM methyl-D,L-aspartate.

On the basis of the above observations, it appeared plausible that YcgR directly interacts with MotA in a c-di-GMP-dependent fashion. To test this idea, we first sought to analyze the subcellular localization of YcgR with the help of *yfp-ycgR* fusion expressed from a plasmid. As a marker for the localization of flagellar basal bodies, we coexpressed a *cfp-fliM* fusion [12]. When expressed in the Δ*yhjH* mutant, both fusion proteins localized to randomly distributed foci in the cell envelope. The majority of Δ*yhjH* mutant cells showed at least two distinct YFP-YcgR foci, while some cells displayed up to eight foci (Figure 32 A). Whereas in the Δ*yhjH* mutant most of the YcgR foci colocalized with CFP-FliM foci, strains that either harbor a WT copy of *yhjH* (*yhjH*+) or a deletion of *motA* (Δ*yhjH* Δ*motA*) displayed irregular, patchy YFP-YcgR fluorescence that was not cell envelope associated and did not colocalize with CFP-FliM (Figure 32 A). Thus, YcgR (but not FliM) focus formation was only observed at elevated c-di-GMP (in the presence of Δ*yhjH*) and in the presence of MotA (Figure 32 A). When WT *motA* was replaced by the *motA* suppressor alleles, the number of YcgR foci was strongly reduced in the absence of YhjH. The few YcgR foci still visible in the motA suppressor strains generally colocalized with FliM (Figure 32 A). Together, these findings suggest that YcgR, upon binding of c-di-GMP, localizes to the flagellar motors, where it interacts with WT MotA. However, this interaction is less efficient than the interaction with MotA harboring exchanges of G93 or S96. To provide evidence for a direct interaction of YcgR and MotA *in vivo*, we measured FRET between MotA-CFP and YFP-YcgR fusion proteins via acceptor photobleaching [168]. Consistent with the delocalized pattern of YcgR in WT cells, no FRET signal was observed in the presence of the phosphodiesterase (PDE) YhjH. In contrast, the Δ*yhjH* mutant showed a pronounced FRET signal that was further increased in a strain lacking additional PDEs, thus displaying an even higher cellular level of c-di-GMP (Figure 32 B). Importantly, FRET signals between YcgR and MotA variants harboring exchanges of G93 or S96 were strongly reduced or completely abolished (Figure 32 B). Taken together, these experiments suggest that YcgR directly interacts with MotA complexes assembled at flagellar basal bodies and that the efficiency of this interaction correlates with the cellular level of c-di-GMP. MotA variants that fail to interact with YcgR and facilitate flagellar function at high c-di-GMP levels harbor exchanges in or close to the FliG-MotA interface, suggesting that YcgR binding might interfere with motor function by modulating the stator-rotor interaction.

A

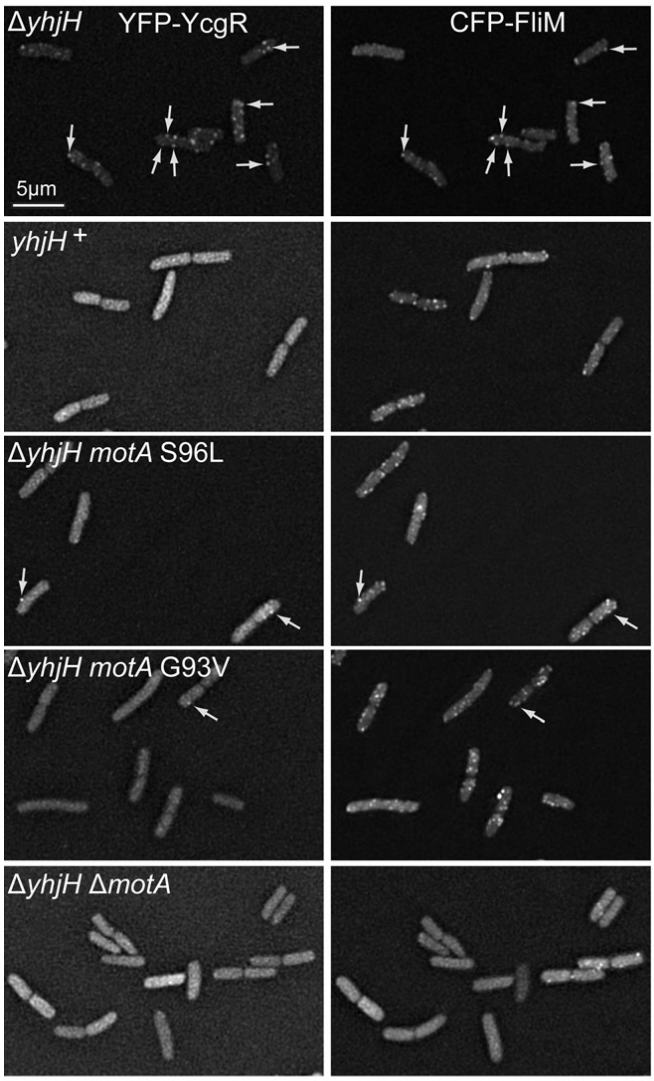

B

relevant genotype	YcgR-MotA FRET (%)	c-di-GMP (pmol/mg)
WT	0	< detection
Δ*yhjH motA*(WT)	1.48 +/- 0.031	22.5 +/- 1.4
Δ*yhjH motA*(G93E)	0	
Δ*yhjH motA*(G93V)	0.20 +/- 0.025	
Δ*yhjH motA*(G93R)	0	
Δ*yhjH motA*(S96L)	0.34 +/- 0.024	
Δ*yhjH* Δ6PDE	2.09 +/- 0.020	28.9 +/- 3.9

Figure 32: YcgR binds to MotA in flagellar basal bodies in a c-di-GMP dependent manner. (A) Fluorescence micrographs of WT and mutant cells coexpressing *yfp-ycgR* (left) and *cfp-fliM* (right). Images are projections of deconvolved micrographs spanning six Z positions. Arrows indicate representative fluorescent foci. (B) Summary of in vivo acceptor photobleaching FRET experiments with YFP-YcgR and MotA-CFP. FRET values, defined as fractional change in the CFP fluorescence upon YFP bleaching, are displayed as percent above baseline with standard deviations. The figure is taken from [152].

4 Discussion

Flagellar motor is a formidable example of self-assembly, involving more than ten different proteins that must form a highly ordered and complex structure. While the extracellular flagellar structure has been well studied using electron microscopy, less is known about the intracellular part of the motor. Here we systematically applied a combination of fluorescence microscopy techniques to get a more comprehensive view of assembly, structure, stability and protein interactions at the flagellar motor. Due to their high similarity with the flagellar export apparatus, we expect our findings to similarly apply to other type III secretion systems.

4.1 Order of the early steps in motor assembly

It is commonly believed that flagellar motor assembly is primed by the insertion of integral membrane components through the Sec-dependent pathway and by their subsequent oligomerization. Membrane oligomers anchor the growing structure in the cytoplasmic membrane and create a base for assembly of cytoplasmic motor components [18]. Our results are consistent with this general view, however they suggest that FlhA rather than FliF is likely to be the first motor component to form the membrane-embedded structure. It is indicated by the fact that at the physiological expression levels FlhA was the only studied protein to show the motor-like localization pattern in the absence of all other motor components. Moreover, we observed direct interaction between FlhA molecules independent of the strain background. In contrast, oligomerization of FliF required assistance of other flagellar proteins, except at very high expression levels that are unlikely to represent the native conditions, and no direct interaction between FliF molecules expressed at the physiological level could be observed in the flagella-less background. Coexpression of FlhA was sufficient to promote the oligomerization of FliF at the physiological expression levels, indicating that the MS-ring formation may be a second step after FlhA in the motor assembly (Figure 23 B). It is supported by the observed interaction between FlhA and FliF and by the previous intergenic suppression data [54]. An additional membrane component of the export apparatus, FliO, was observed to interact with FlhA and with itself, suggesting that it may also be recruited, and oligomerize, at the early stage of the motor assembly. Consistent with a number of previous studies [109, 180-183], subsequent assembly of the switch

complex and its association with the MS-ring are likely to be mediated by multiple observed interactions among FliF, FliG, FliM and FliN. The localization studies in the knock-out strains suggest that FliG is the first protein to associate with the growing motor, followed by FliM and then by FliN. Observed direct interaction between FliN molecules is consistent with the model that FliN binds to the motor in a tetrameric form [184, 185]. The cytoplasmic components of the export apparatus, FliH and FliI, required all of FlhA, the MS-ring and the switch complex to localize, suggesting that they assemble as the last part of the structure. FRET between FliH or FliI and the switch proteins, observed in the wild-type strain, confirmed recent suggestions that FliH/FliI complex docks to the switch complex of the motor [45, 186]. The direct interaction between FliH and FliN, which was observed in a previous *in-vitro* study [67], was not seen in this work, possibly due to the unfavourable position or orientation of YFP and CFP molecules.

4.2 Cooperativity of motor assembly

Although the sequential steps of protein assembly into the growing motor could be relatively defined, our results also suggest there is a degree of cooperativity between the steps of assembly process. FliH and FliI apparently only localized to the motor as a complex, in agreement with a recent study [186], which may explain the absence of interactions of either FliH or FliI with the individual switch proteins in Δ*flhC* background. The MS-ring formation is apparently assisted not only by the FliF interaction with FlhA, but also by the presence of FliG. Interestingly, neither stoichiometric amounts nor localization of FliG is required for the FliG-dependent promotion of the FliF oligomerization, indicating that FliG acts as a catalyst of assembly. We propose that both FlhA and FliG stabilize FliF in the conformation that favors oligomerization. Similarly, FliG localization at the motor was stabilized by FliM and FliN, and the assembly of FliM was stabilized by FliN, as observed before [144]. Binding of FliM and FliN also appeared to stabilize – either directly or indirectly – the MS-ring. The resulting model of assembly suggests that each subsequent step in a sequential assembly can stabilize the preassembled structure. We speculate that this may be a common characteristic of the self-assembly mechanisms of large intracellular structures.

4.3 Additional protein interactions at the motor

In addition to mapping the interactions involved in the assembly of the export apparatus,

the MS-ring and the switch complex, we observed several other interactions that might be involved in assembly and regulation of the motor. FliL was observed to oligomerize in the membrane and to locate proximally to FliG in a functional motor, in agreement with a recent study [187]. We confirmed interaction of H-NS with FliG [109] and observed an further interaction with FliN, providing additional evidence that H-NS binding to the motor is specific. Specific binding of the fumarate reductase to the motor [107] could also be confirmed and mapped to interaction between FRDA and FliG. Extending our previous observation that YcgR shows FRET with the stator component MotA in motile cells [152], we confirmed here that this binding is direct. We further observed interactions of several cytoplasmic motor components with DnaK (Hsp70) and HtpG (Hsp90), indicating involvement of these general chaperones into assembly of the motor. Interestingly, there were direct interactions detected between HtpG and FliN or FliI, both of which are oligomeric proteins. Eukaryotic Hsp90 is known to play a role in assembly and regulation of oligomeric complexes, thus bacterial HtpG might have a similar function (see session 4.6 for more detailed discussion).

4.4 Structure and stability of the motor

Our study of the protein exchange revealed that even the assembled motor is a relatively dynamic structure. While the MS-ring at the base of the motor was stable over 15 min measurement time, the switch complex component FliM, as well as FliH and FlhA components of the export apparatus showed clear exchange, with the half-time of 10 to 15 min. Faster exchange of FlhA compared to FliF and even to FliH was surprising, demonstrating that the motor dynamics is not directly related to the order of assembly, and confirming that individual proteins can exchange without compromising the integrity of the overall structure. Our results are consistent with recent FRAP-based observations of the switch complex protein turnover [175, 176] and provide an overall view of the motor stability, where FliF and FliG form a stable core and other proteins exchange on time scales of 10 to 20 minutes (Figure 21 E). Similar dynamics was observed for MotB molecules in the stator complex [188].

These finding allowed us to revise the structural model of the motor and change our view of the protein export by type III secretion system. Stability of FliH association with the motor switch complex means that FliH does not undergo a cycle of exchange between the cytoplasm and the motor while feeding substrates into the export channel, as has been postulated before [45, 186]. Moreover, the dynamics of FlhA exchange implies that the

oligomeric membrane-embedded core of the FlhA structure – presumably a ring – is formed outside, rather than inside, the MS-ring (Figure 23). Assuming such protein arrangement is also required to explain how 20 FlhA subunits with a total of 160 (20×8) membrane helices can be accommodated at the motor, given that the inner size of the MS-ring only allows incorporation of ~70 transmembrane helices [18, 53]. The estimated total size of these helices is sufficient to form an FlhA oligomer outside of the MS-ring, but the two structures may also partly intercalate, since FliF has only two transmembrane helices. Whatever the exact arrangement of the FlhA oligomer outside of the MS-ring, FlhA dynamics observed by FRAP may allow efficient insertion of membrane proteins by the general secretion machinery inside this structure, resolving an apparent paradox of how the export apparatus can assemble inside the stable MS-ring [18]. Moreover, the linker region between the transmembrane and C-terminal domains of FlhA is sufficiently long (34 amino acids) to span the MS-ring or the junction between the MS-ring and the switch complex, to enable interactions of the C-terminal domain with other components of the export apparatus and with export substrates. According to the recently published crystal structure of the C-terminal domain of FlhA [57, 189], 20 domains of such size can be accommodated in the C-ring but not in the MS-ring. We therefore propose that the C-terminal domains of individual FlhA subunits may move between the two structures, accepting the export substrates at the C-ring through the interaction with FliH [186] that is stably bound there, and then bringing the substrates to the export channel. This model is in agreement with recent data that indicate a more active role of FlhA in the export process [57, 190].

4.5 Regulation of protein stability by the complex formation

It is well established in eukaryotes that the unassembled subunits of some multimeric complexes are degraded by the ER-associated degradation (ERAD) pathway [191]. An increase in protein stability upon complex formation may stem from a general decrease in the conformational dynamics or from protection of the amino acid sequences that are recognized by the degradation machinery. Our results for the membrane components of the motor indicate that a similar mechanism of quality control may be functional in bacteria, although the identity of the degradation machinery and the details of the protein recognition remain unknown. FliF and FlhA were clearly stabilized against proteolysis under conditions that favored their oligomerization. The effect was particularly

pronounced for FliF, consistent with its poor self-assembly into oligomers in the absence of other motor proteins. Although the generality of the observed assembly-dependent regulation of membrane protein degradation in bacteria remains to be established, it is likely that assembly of other multimeric complexes at the inner membrane relies on a similar control mechanism.

4.6 Involvement of DnaK/HtpG machinery in assembly of flagellar motor and chemosensory complexes

The DnaK (Hsp70) chaperone binds non-specifically to many unfolded polypeptides and also binds selectively to specific substrates. Although its involvement in assisting proper folding of proteins is well documented, less is known about its role in regulating the folded polypeptides. Takaya *et al.* [192] demonstrated that DnaK regulates the expression of the *Salmonella* flagellar regulon by activating native $FlhD_2C_2$ complex into a regulator of flagellar regulon expression, suggesting the involvement of the DnaK chaperone machinery in activating folded oligomerized proteins. We observed interactions of DnaK with several cytoplasmic motor components, such as the ATPase complex proteins FliI and FliJ in the wild type, suggesting DnaK may have a similar function to keep the ATPase complex active, as in the case of the $FlhD_2C_2$ complex. Weak direct interaction of DnaK with C-ring proteins indicates the involvement of DnaK in motor assembly.

Even more interesting were the observed interactions of HtpG. Although HtpG is a general Hsp90 chaperone in *E. coli* and other bacteria, its substrates remain unknown. We found that HtpG interacts directly with motor components FliN and FliI, as well as with chemotaxis components Tar, CheA or CheZ, all of which are oligomeric proteins and could thus be potential substrates of HtpG in *E.coli*. By investigating the interactions of HtpG(E34A) with truncated Tar, we found the interacting domains of Tar are the cytoplasmic signalling and adaptation domains (Figure 25 D). Similarly, we found that P3 domain of CheA that is responsible for the dimerization of CheA was required for the interactions with HtpG(E34A) (Figure 25 D). These results suggest that HtpG may be involved in assembly of chemosensory complexes by interacting with its oligomeric components, similar to the involvement of the eukaryotic Hsp90 in assembly of signalling complexes. The role of HtpG in chemotaxis was also indicated by the chemotaxis defects of the *htpG*(E34A) mutant strain at 39 °C. At 34 °C, however, no relavant difference of chemotaxis and kinase activity between wild type and *htpG*(E34A) mutant was observed,

indicating the effects of HtpG on chemotaxis only become pronounced at higher temperature. Furthermore, complementation experiments showed that the defect in chemotaxis of the *htpG*(E34A) mutant strain can be partially compensated by the overexpression of Tar or CheA. Similar partial compensation was observed upon overexpression of FliN, HtpG binding partner at the motor. Moreover, the interaction of HtpG with FliN and CheA, which are expressed and assembled at different time points of the cell culture growth, showed differences in temporally dynamics. The observed temporal order corresponded to the expected order of assembly of motors and chemoreceptor clusters, and the peak of interaction of HtpG with FliN appeared to correlate with the development of cell motility. This result indicates that HtpG is involved in the whole process of motor and receptor cluster assembly. Moreover, the disappearance of interactions between HtpG and FliN or CheA in the absence of DnaJ and CbpA indicates that these proteins might be delivered to the DnaK complex via DnaJ and then transferred to HtpG machinery, as usual pathways in the Hsp70/Hsp90 chaperone machinery in eukaryotes (Figure 8).

4.7 Cyclic di-GMP regulates bacterial flagellar motor

Cyclic di-GMP is the molecule of the moment in bacteriology. It is synthesized from two molecules of GTP by diguanylate cyclase domains and is broken down by phosphodiesterase domains. This ubiquitous secondary messenger has been implicated in many processes, from pathogenicity to biofilm formation [74]. Our results reveal the direct involvement of cyclic di-GMP in the regulation of flagellar movement and bacterial swimming. Cyclic di-GMP activates YcgR, which then binds directly to the flagellar motor, causing the motor to slow down. By controlling the expression and activity of YcgR, diguanylate cyclases, and the phosphodiesterase YhjH, bacteria can reduce their swimming speed when cyclic di-GMP levels increase. By fusing YcgR to fluorescent proteins, we found that YcgR colocalized with the flagellar motor when the phosphodiesterase YhjH was inactivated. In collaboration with Jenal's group in Basel, we found specific mutations in the stator protein MotA that resulted in fast swimming even in the presence of high levels of cyclic di-GMP. FRET data supported existence of direct interactions between fluorescently labeled MotA and YcgR proteins, with a strong signal in the presence of cyclic di-GMP and a weak signal in its absence. Thus, the YcgR protein appears to act on the motor via direct interaction with MotA and not indirectly

through motor assembly, as thought previously [114]. The braking action of YcgR appears to occur as the bacteria enter starvation or stationary growth conditions, when it may be advantageous to slow down and locate a surface to attach to and initiate biofilm formation [74]. Our results demonstrate that bacteria can modulate flagellar motor output and thus swimming velocity in response to environmental cues.

5 References

1. Namba, K. and F. Vonderviszt, *Molecular architecture of bacterial flagellum.* Q Rev Biophys, 1997. **30**(1): p. 1-65.
2. Berry, R.M. and J.P. Armitage, *The bacterial flagella motor.* Adv Microb Physiol, 1999. **41**: p. 291-337.
3. Berg, H.C., *The rotary motor of bacterial flagella.* Annu Rev Biochem, 2003. **72**: p. 19-54.
4. Kojima, S. and D.F. Blair, *Solubilization and purification of the MotA/MotB complex of Escherichia coli.* Biochemistry, 2004. **43**(1): p. 26-34.
5. Berg, H.C. and D.A. Brown, *Chemotaxis in Escherichia coli analysed by three-dimensional tracking.* Nature, 1972. **239**(5374): p. 500-4.
6. Turner, L., W.S. Ryu, and H.C. Berg, *Real-time imaging of fluorescent flagellar filaments.* J Bacteriol, 2000. **182**(10): p. 2793-801.
7. Macnab, R.M. and D.E. Koshland, Jr., *The gradient-sensing mechanism in bacterial chemotaxis.* Proc Natl Acad Sci U S A, 1972. **69**(9): p. 2509-12.
8. Sourjik, V., *Receptor clustering and signal processing in E. coli chemotaxis.* Trends Microbiol, 2004. **12**(12): p. 569-76.
9. Falke, J.J., et al., *The two-component signaling pathway of bacterial chemotaxis: a molecular view of signal transduction by receptors, kinases, and adaptation enzymes.* Annu Rev Cell Dev Biol, 1997. **13**: p. 457-512.
10. Gegner, J.A., et al., *Assembly of an MCP receptor, CheW, and kinase CheA complex in the bacterial chemotaxis signal transduction pathway.* Cell, 1992. **70**(6): p. 975-82.
11. Cluzel, P., M. Surette, and S. Leibler, *An ultrasensitive bacterial motor revealed by monitoring signaling proteins in single cells.* Science, 2000. **287**(5458): p. 1652-5.
12. Sourjik, V. and H.C. Berg, *Binding of the Escherichia coli response regulator CheY to its target measured in vivo by fluorescence resonance energy transfer.* Proc Natl Acad Sci U S A, 2002. **99**(20): p. 12669-74.
13. Segall, J.E., A. Ishihara, and H.C. Berg, *Chemotactic signaling in filamentous cells of Escherichia coli.* J Bacteriol, 1985. **161**(1): p. 51-9.
14. Wolfe, A.J., et al., *Reconstitution of signaling in bacterial chemotaxis.* J Bacteriol, 1987. **169**(5): p. 1878-85.
15. McNally, D.F. and P. Matsumura, *Bacterial chemotaxis signaling complexes: formation of a CheA/CheW complex enhances autophosphorylation and affinity for CheY.* Proc Natl Acad Sci U S A, 1991. **88**(14): p. 6269-73.
16. Djordjevic, S., et al., *Structural basis for methylesterase CheB regulation by a phosphorylation-activated domain.* Proc Natl Acad Sci U S A, 1998. **95**(4): p. 1381-6.
17. Anand, G.S. and A.M. Stock, *Kinetic basis for the stimulatory effect of phosphorylation on the methylesterase activity of CheB.* Biochemistry, 2002. **41**(21):

p. 6752-60.
18. Macnab, R.M., *How bacteria assemble flagella.* Annu Rev Microbiol, 2003. **57**: p. 77-100.
19. Berg, H.C. and R.A. Anderson, *Bacteria swim by rotating their flagellar filaments.* Nature, 1973. **245**(5425): p. 380-2.
20. Macnab, R.M., *Flagella and motility in Escherichia coli and Salmonella typhimurium.* Cellular and Molecular Biology (ed. Ingraham, J. L. & Neidhardt, F. C.), 1996. **ASM, Washington, DC**: p. 123-145.
21. Khan, I.H., T.S. Reese, and S. Khan, *The cytoplasmic component of the bacterial flagellar motor.* Proc Natl Acad Sci U S A, 1992. **89**(13): p. 5956-60.
22. Xing, J., et al., *Torque-speed relationship of the bacterial flagellar motor.* Proc Natl Acad Sci U S A, 2006. **103**(5): p. 1260-5.
23. Francis, N.R., et al., *Isolation, characterization and structure of bacterial flagellar motors containing the switch complex.* J Mol Biol, 1994. **235**(4): p. 1261-70.
24. Thomas, D.R., D.G. Morgan, and D.J. DeRosier, *Rotational symmetry of the C ring and a mechanism for the flagellar rotary motor.* Proc Natl Acad Sci U S A, 1999. **96**(18): p. 10134-9.
25. Thomas, D.R., et al., *The three-dimensional structure of the flagellar rotor from a clockwise-locked mutant of Salmonella enterica serovar Typhimurium.* J Bacteriol, 2006. **188**(20): p. 7039-48.
26. DePamphilis, M.L. and J. Adler, *Attachment of flagellar basal bodies to the cell envelope: specific attachment to the outer, lipopolysaccharide membrane and the cyoplasmic membrane.* J Bacteriol, 1971. **105**(1): p. 396-407.
27. DePamphilis, M.L. and J. Adler, *Fine structure and isolation of the hook-basal body complex of flagella from Escherichia coli and Bacillus subtilis.* J Bacteriol, 1971. **105**(1): p. 384-95.
28. DePamphilis, M.L. and J. Adler, *Purification of intact flagella from Escherichia coli and Bacillus subtilis.* J Bacteriol, 1971. **105**(1): p. 376-83.
29. Ueno, T., K. Oosawa, and S. Aizawa, *M ring, S ring and proximal rod of the flagellar basal body of Salmonella typhimurium are composed of subunits of a single protein, FliF.* J Mol Biol, 1992. **227**(3): p. 672-7.
30. Suzuki, H., K. Yonekura, and K. Namba, *Structure of the rotor of the bacterial flagellar motor revealed by electron cryomicroscopy and single-particle image analysis.* J Mol Biol, 2004. **337**(1): p. 105-13.
31. Lloyd, S.A., et al., *Torque generation in the flagellar motor of Escherichia coli: evidence of a direct role for FliG but not for FliM or FliN.* J Bacteriol, 1996. **178**(1): p. 223-31.
32. Kojima, S. and D.F. Blair, *Conformational change in the stator of the bacterial flagellar motor.* Biochemistry, 2001. **40**(43): p. 13041-50.
33. Blocker, A., K. Komoriya, and S. Aizawa, *Type III secretion systems and bacterial flagella: insights into their function from structural similarities.* Proc Natl Acad Sci U S A, 2003. **100**(6): p. 3027-30.
34. Galan, J.E. and H. Wolf-Watz, *Protein delivery into eukaryotic cells by type III*

secretion machines. Nature, 2006. **444**(7119): p. 567-73.
35. Michiels, T. and G.R. Cornelis, *Secretion of hybrid proteins by the Yersinia Yop export system.* J Bacteriol, 1991. **173**(5): p. 1677-85.
36. Vonderviszt, F., S. Aizawa, and K. Namba, *Role of the disordered terminal regions of flagellin in filament formation and stability.* J Mol Biol, 1991. **221**(4): p. 1461-74.
37. Parsot, C., C. Hamiaux, and A.L. Page, *The various and varying roles of specific chaperones in type III secretion systems.* Curr Opin Microbiol, 2003. **6**(1): p. 7-14.
38. Akeda, Y. and J.E. Galan, *Chaperone release and unfolding of substrates in type III secretion.* Nature, 2005. **437**(7060): p. 911-5.
39. Minamino, T. and K. Namba, *Distinct roles of the FliI ATPase and proton motive force in bacterial flagellar protein export.* Nature, 2008. **451**(7177): p. 485-8.
40. Paul, K., et al., *Energy source of flagellar type III secretion.* Nature, 2008. **451**(7177): p. 489-92.
41. Iino, T., *Polarity of flagellar growth in salmonella.* J Gen Microbiol, 1969. **56**(2): p. 227-39.
42. Namba, K., I. Yamashita, and F. Vonderviszt, *Structure of the core and central channel of bacterial flagella.* Nature, 1989. **342**(6250): p. 648-54.
43. Morgan, D.G., et al., *Domain organization of the subunit of the Salmonella typhimurium flagellar hook.* J Mol Biol, 1993. **229**(1): p. 79-84.
44. Yonekura, K., S. Maki-Yonekura, and K. Namba, *Complete atomic model of the bacterial flagellar filament by electron cryomicroscopy.* Nature, 2003. **424**(6949): p. 643-50.
45. Minamino, T., K. Imada, and K. Namba, *Mechanisms of type III protein export for bacterial flagellar assembly.* Mol Biosyst, 2008. **4**(11): p. 1105-15.
46. Minamino, T. and R.M. Macnab, *Components of the Salmonella flagellar export apparatus and classification of export substrates.* J Bacteriol, 1999. **181**(5): p. 1388-94.
47. Yokoseki, T., et al., *Functional analysis of the flagellar genes in the fliD operon of Salmonella typhimurium.* Microbiology, 1995. **141 (Pt 7)**: p. 1715-22.
48. Fraser, G.M., J.C. Bennett, and C. Hughes, *Substrate-specific binding of hook-associated proteins by FlgN and FliT, putative chaperones for flagellum assembly.* Mol Microbiol, 1999. **32**(3): p. 569-80.
49. Auvray, F., et al., *Flagellin polymerisation control by a cytosolic export chaperone.* J Mol Biol, 2001. **308**(2): p. 221-9.
50. Bennett, J.C., et al., *Substrate complexes and domain organization of the Salmonella flagellar export chaperones FlgN and FliT.* Mol Microbiol, 2001. **39**(3): p. 781-91.
51. Aldridge, P., J. Karlinsey, and K.T. Hughes, *The type III secretion chaperone FlgN regulates flagellar assembly via a negative feedback loop containing its chaperone substrates FlgK and FlgL.* Mol Microbiol, 2003. **49**(5): p. 1333-45.
52. Aldridge, P.D., et al., *The flagellar-specific transcription factor, sigma28, is the Type III secretion chaperone for the flagellar-specific anti-sigma28 factor FlgM.*

Genes Dev, 2006. **20**(16): p. 2315-26.
53. Fan, F., et al., *The FliP and FliR proteins of Salmonella typhimurium, putative components of the type III flagellar export apparatus, are located in the flagellar basal body.* Mol Microbiol, 1997. **26**(5): p. 1035-46.
54. Kihara, M., et al., *Intergenic suppression between the flagellar MS ring protein FliF of Salmonella and FlhA, a membrane component of its export apparatus.* J Bacteriol, 2001. **183**(5): p. 1655-62.
55. Minamino, T. and R.M. MacNab, *Interactions among components of the Salmonella flagellar export apparatus and its substrates.* Mol Microbiol, 2000. **35**(5): p. 1052-64.
56. Ghelardi, E., et al., *Requirement of flhA for swarming differentiation, flagellin export, and secretion of virulence-associated proteins in Bacillus thuringiensis.* J Bacteriol, 2002. **184**(23): p. 6424-33.
57. Bange, G., et al., *FlhA provides the adaptor for coordinated delivery of late flagella building blocks to the type III secretion system.* Proc Natl Acad Sci U S A, 2010. **107**(25): p. 11295-300.
58. Williams, A.W., et al., *Mutations in fliK and flhB affecting flagellar hook and filament assembly in Salmonella typhimurium.* J Bacteriol, 1996. **178**(10): p. 2960-70.
59. Kutsukake, K., *Hook-length control of the export-switching machinery involves a double-locked gate in Salmonella typhimurium flagellar morphogenesis.* J Bacteriol, 1997. **179**(4): p. 1268-73.
60. Minamino, T. and R.M. Macnab, *Domain structure of Salmonella FlhB, a flagellar export component responsible for substrate specificity switching.* J Bacteriol, 2000. **182**(17): p. 4906-14.
61. Fraser, G.M., et al., *Substrate specificity of type III flagellar protein export in Salmonella is controlled by subdomain interactions in FlhB.* Mol Microbiol, 2003. **48**(4): p. 1043-57.
62. Vogler, A.P., et al., *Salmonella typhimurium mutants defective in flagellar filament regrowth and sequence similarity of FliI to F0F1, vacuolar, and archaebacterial ATPase subunits.* J Bacteriol, 1991. **173**(11): p. 3564-72.
63. Minamino, T. and R.M. Macnab, *FliH, a soluble component of the type III flagellar export apparatus of Salmonella, forms a complex with FliI and inhibits its ATPase activity.* Mol Microbiol, 2000. **37**(6): p. 1494-503.
64. Minamino, T., et al., *Role of FliJ in flagellar protein export in Salmonella.* J Bacteriol, 2000. **182**(15): p. 4207-15.
65. Evans, L.D., et al., *An escort mechanism for cycling of export chaperones during flagellum assembly.* Proc Natl Acad Sci U S A, 2006. **103**(46): p. 17474-9.
66. Fraser, G.M., et al., *Interactions of FliJ with the Salmonella type III flagellar export apparatus.* J Bacteriol, 2003. **185**(18): p. 5546-54.
67. Gonzalez-Pedrajo, B., et al., *Interactions between C ring proteins and export apparatus components: a possible mechanism for facilitating type III protein export.* Mol Microbiol, 2006. **60**(4): p. 984-98.

68. McMurry, J.L., J.W. Murphy, and B. Gonzalez-Pedrajo, *The FliN-FliH interaction mediates localization of flagellar export ATPase FliI to the C ring complex.* Biochemistry, 2006. **45**(39): p. 11790-8.
69. Paul, K., J.G. Harmon, and D.F. Blair, *Mutational analysis of the flagellar rotor protein FliN: identification of surfaces important for flagellar assembly and switching.* J Bacteriol, 2006. **188**(14): p. 5240-8.
70. McCarter, L.L., *Regulation of flagella.* Curr Opin Microbiol, 2006. **9**(2): p. 180-6.
71. Lehnen, D., et al., *LrhA as a new transcriptional key regulator of flagella, motility and chemotaxis genes in Escherichia coli.* Mol Microbiol, 2002. **45**(2): p. 521-32.
72. Macnab, R.M., *Escherichia coli and Salmonella.* Cellular and Molecular Biology (ed. Ingraham, J. L. & Neidhardt, F. C.), 1996. **ASM, Washington, DC**: p. 123-142.
73. Landini, P. and A.J. Zehnder, *The global regulatory hns gene negatively affects adhesion to solid surfaces by anaerobically grown Escherichia coli by modulating expression of flagellar genes and lipopolysaccharide production.* J Bacteriol, 2002. **184**(6): p. 1522-9.
74. Hengge, R., *Principles of c-di-GMP signalling in bacteria.* Nat Rev Microbiol, 2009. **7**(4): p. 263-73.
75. Kutsukake, K., Y. Ohya, and T. Iino, *Transcriptional analysis of the flagellar regulon of Salmonella typhimurium.* J Bacteriol, 1990. **172**(2): p. 741-7.
76. Liu, X. and P. Matsumura, *The FlhD/FlhC complex, a transcriptional activator of the Escherichia coli flagellar class II operons.* J Bacteriol, 1994. **176**(23): p. 7345-51.
77. Pruss, B.M., et al., *FlhD/FlhC-regulated promoters analyzed by gene array and lacZ gene fusions.* FEMS Microbiol Lett, 2001. **197**(1): p. 91-7.
78. Chilcott, G.S. and K.T. Hughes, *Coupling of flagellar gene expression to flagellar assembly in Salmonella enterica serovar typhimurium and Escherichia coli.* Microbiol Mol Biol Rev, 2000. **64**(4): p. 694-708.
79. Kalir, S. and U. Alon, *Using a quantitative blueprint to reprogram the dynamics of the flagella gene network.* Cell, 2004. **117**(6): p. 713-20.
80. Kitano, H., *Biological robustness.* Nat Rev Genet, 2004. **5**(11): p. 826-37.
81. Li, M. and G.L. Hazelbauer, *Cellular stoichiometry of the components of the chemotaxis signaling complex.* J Bacteriol, 2004. **186**(12): p. 3687-94.
82. Ohnishi, K., et al., *A novel transcriptional regulation mechanism in the flagellar regulon of Salmonella typhimurium: an antisigma factor inhibits the activity of the flagellum-specific sigma factor, sigma F.* Mol Microbiol, 1992. **6**(21): p. 3149-57.
83. Hughes, K.T., et al., *Sensing structural intermediates in bacterial flagellar assembly by export of a negative regulator.* Science, 1993. **262**(5137): p. 1277-80.
84. Mytelka, D.S. and M.J. Chamberlin, *Escherichia coli fliAZY operon.* J Bacteriol, 1996. **178**(1): p. 24-34.
85. Kutsukake, K., T. Ikebe, and S. Yamamoto, *Two novel regulatory genes, fliT and fliZ, in the flagellar regulon of Salmonella.* Genes Genet Syst, 1999. **74**(6): p. 287-92.

86. Saini, S., et al., *FliZ Is a posttranslational activator of FlhD4C2-dependent flagellar gene expression.* J Bacteriol, 2008. **190**(14): p. 4979-88.
87. Yamamoto, S. and K. Kutsukake, *FliT acts as an anti-FlhD2C2 factor in the transcriptional control of the flagellar regulon in Salmonella enterica serovar typhimurium.* J Bacteriol, 2006. **188**(18): p. 6703-8.
88. Suzuki, T., et al., *Incomplete flagellar structures in nonflagellate mutants of Salmonella typhimurium.* J Bacteriol, 1978. **133**(2): p. 904-15.
89. Suzuki, T. and Y. Komeda, *Incomplete flagellar structures in Escherichia coli mutants.* J Bacteriol, 1981. **145**(2): p. 1036-41.
90. Kubori, T., et al., *Morphological pathway of flagellar assembly in Salmonella typhimurium.* J Mol Biol, 1992. **226**(2): p. 433-46.
91. Katayama, E., et al., *Geometry of the flagellar motor in the cytoplasmic membrane of Salmonella typhimurium as determined by stereo-photogrammetry of quick-freeze deep-etch replica images.* J Mol Biol, 1996. **255**(3): p. 458-75.
92. Aizawa, S.I., *Flagellar assembly in Salmonella typhimurium.* Mol Microbiol, 1996. **19**(1): p. 1-5.
93. Jones, C.J. and R.M. Macnab, *Flagellar assembly in Salmonella typhimurium: analysis with temperature-sensitive mutants.* J Bacteriol, 1990. **172**(3): p. 1327-39.
94. Kubori, T., S. Yamaguchi, and S. Aizawa, *Assembly of the switch complex onto the MS ring complex of Salmonella typhimurium does not require any other flagellar proteins.* J Bacteriol, 1997. **179**(3): p. 813-7.
95. Blair, D.F. and H.C. Berg, *Restoration of torque in defective flagellar motors.* Science, 1988. **242**(4886): p. 1678-81.
96. Homma, M., et al., *FlgB, FlgC, FlgF and FlgG. A family of structurally related proteins in the flagellar basal body of Salmonella typhimurium.* J Mol Biol, 1990. **211**(2): p. 465-77.
97. Minamino, T., K. Imada, and K. Namba, *Molecular motors of the bacterial flagella.* Curr Opin Struct Biol, 2008. **18**(6): p. 693-701.
98. Muller, V., et al., *Characterization of the fliE genes of Escherichia coli and Salmonella typhimurium and identification of the FliE protein as a component of the flagellar hook-basal body complex.* J Bacteriol, 1992. **174**(7): p. 2298-304.
99. Minamino, T., S. Yamaguchi, and R.M. Macnab, *Interaction between FliE and FlgB, a proximal rod component of the flagellar basal body of Salmonella.* J Bacteriol, 2000. **182**(11): p. 3029-36.
100. Nambu, T., et al., *Peptidoglycan-hydrolyzing activity of the FlgJ protein, essential for flagellar rod formation in Salmonella typhimurium.* J Bacteriol, 1999. **181**(5): p. 1555-61.
101. Hirano, T., T. Minamino, and R.M. Macnab, *The role in flagellar rod assembly of the N-terminal domain of Salmonella FlgJ, a flagellum-specific muramidase.* J Mol Biol, 2001. **312**(2): p. 359-69.
102. Nambu, T. and K. Kutsukake, *The Salmonella FlgA protein, a putativeve periplasmic chaperone essential for flagellar P ring formation.* Microbiology, 2000. **146 (Pt 5)**: p. 1171-8.

103. Dailey, F.E. and H.C. Berg, *Mutants in disulfide bond formation that disrupt flagellar assembly in Escherichia coli.* Proc Natl Acad Sci U S A, 1993. **90**(3): p. 1043-7.
104. Schoenhals, G.J. and R.M. Macnab, *Physiological and biochemical analyses of FlgH, a lipoprotein forming the outer membrane L ring of the flagellar basal body of Salmonella typhimurium.* J Bacteriol, 1996. **178**(14): p. 4200-7.
105. Ikeda, T., et al., *Localization and stoichiometry of hook-associated proteins within Salmonella typhimurium flagella.* J Bacteriol, 1987. **169**(3): p. 1168-73.
106. Emerson, S.U., K. Tokuyasu, and M.I. Simon, *Bacterial flagella: polarity of elongation.* Science, 1970. **169**(941): p. 190-2.
107. Cohen-Ben-Lulu, G.N., et al., *The bacterial flagellar switch complex is getting more complex.* EMBO J, 2008. **27**(7): p. 1134-44.
108. Prasad, K., S.R. Caplan, and M. Eisenbach, *Fumarate modulates bacterial flagellar rotation by lowering the free energy difference between the clockwise and counterclockwise states of the motor.* J Mol Biol, 1998. **280**(5): p. 821-8.
109. Marykwas, D.L., S.A. Schmidt, and H.C. Berg, *Interacting components of the flagellar motor of Escherichia coli revealed by the two-hybrid system in yeast.* J Mol Biol, 1996. **256**(3): p. 564-76.
110. Ko, M. and C. Park, *Two novel flagellar components and H-NS are involved in the motor function of Escherichia coli.* J Mol Biol, 2000. **303**(3): p. 371-82.
111. Bertin, P., et al., *The H-NS protein is involved in the biogenesis of flagella in Escherichia coli.* J Bacteriol, 1994. **176**(17): p. 5537-40.
112. Donato, G.M. and T.H. Kawula, *Enhanced binding of altered H-NS protein to flagellar rotor protein FliG causes increased flagellar rotational speed and hypermotility in Escherichia coli.* J Biol Chem, 1998. **273**(37): p. 24030-6.
113. Ryjenkov, D.A., et al., *The PilZ domain is a receptor for the second messenger c-di-GMP: the PilZ domain protein YcgR controls motility in enterobacteria.* J Biol Chem, 2006. **281**(41): p. 30310-4.
114. Wolfe, A.J. and K.L. Visick, *Get the message out: cyclic-Di-GMP regulates multiple levels of flagellum-based motility.* J Bacteriol, 2008. **190**(2): p. 463-75.
115. Jenal, U. and J. Malone, *Mechanisms of cyclic-di-GMP signaling in bacteria.* Annu Rev Genet, 2006. **40**: p. 385-407.
116. Schirmer, T. and U. Jenal, *Structural and mechanistic determinants of c-di-GMP signalling.* Nat Rev Microbiol, 2009. **7**(10): p. 724-35.
117. Galperin, M.Y., *A census of membrane-bound and intracellular signal transduction proteins in bacteria: bacterial IQ, extroverts and introverts.* BMC Microbiol, 2005. **5**: p. 35.
118. Frye, J., et al., *Identification of new flagellar genes of Salmonella enterica serovar Typhimurium.* J Bacteriol, 2006. **188**(6): p. 2233-43.
119. Girgis, H.S., et al., *A comprehensive genetic characterization of bacterial motility.* PLoS Genet, 2007. **3**(9): p. 1644-60.
120. Pesavento, C., et al., *Inverse regulatory coordination of motility and curli-mediated adhesion in Escherichia coli.* Genes Dev, 2008. **22**(17): p. 2434-46.

121. Mayer, M.P. and B. Bukau, *Hsp70 chaperones: cellular functions and molecular mechanism.* Cell Mol Life Sci, 2005. **62**(6): p. 670-84.
122. Meimaridou, E., S.B. Gooljar, and J.P. Chapple, *From hatching to dispatching: the multiple cellular roles of the Hsp70 molecular chaperone machinery.* J Mol Endocrinol, 2009. **42**(1): p. 1-9.
123. Wegele, H., L. Muller, and J. Buchner, *Hsp70 and Hsp90--a relay team for protein folding.* Rev Physiol Biochem Pharmacol, 2004. **151**: p. 1-44.
124. Mayer, M.P. and B. Bukau, *Molecular chaperones: the busy life of Hsp90.* Curr Biol, 1999. **9**(9): p. R322-5.
125. Joab, I., et al., *Common non-hormone binding component in non-transformed chick oviduct receptors of four steroid hormones.* Nature, 1984. **308**(5962): p. 850-3.
126. Wilhelmsson, A., et al., *The specific DNA binding activity of the dioxin receptor is modulated by the 90 kd heat shock protein.* EMBO J, 1990. **9**(1): p. 69-76.
127. Oppermann, H., W. Levinson, and J.M. Bishop, *A cellular protein that associates with the transforming protein of Rous sarcoma virus is also a heat-shock protein.* Proc Natl Acad Sci U S A, 1981. **78**(2): p. 1067-71.
128. Stancato, L.F., et al., *Raf exists in a native heterocomplex with hsp90 and p50 that can be reconstituted in a cell-free system.* J Biol Chem, 1993. **268**(29): p. 21711-6.
129. Aligue, R., H. Akhavan-Niak, and P. Russell, *A role for Hsp90 in cell cycle control: Wee1 tyrosine kinase activity requires interaction with Hsp90.* EMBO J, 1994. **13**(24): p. 6099-106.
130. Cutforth, T. and G.M. Rubin, *Mutations in Hsp83 and cdc37 impair signaling by the sevenless receptor tyrosine kinase in Drosophila.* Cell, 1994. **77**(7): p. 1027-36.
131. Dai, K., R. Kobayashi, and D. Beach, *Physical interaction of mammalian CDC37 with CDK4.* J Biol Chem, 1996. **271**(36): p. 22030-4.
132. Chen, C.F., et al., *A new member of the hsp90 family of molecular chaperones interacts with the retinoblastoma protein during mitosis and after heat shock.* Mol Cell Biol, 1996. **16**(9): p. 4691-9.
133. Sepehrnia, B., et al., *Heat shock protein 84 forms a complex with mutant p53 protein predominantly within a cytoplasmic compartment of the cell.* J Biol Chem, 1996. **271**(25): p. 15084-90.
134. Jakob, U., et al., *Transient interaction of Hsp90 with early unfolding intermediates of citrate synthase. Implications for heat shock in vivo.* J Biol Chem, 1995. **270**(13): p. 7288-94.
135. Itoh, T., H. Matsuda, and H. Mori, *Phylogenetic analysis of the third hsp70 homolog in Escherichia coli; a novel member of the Hsc66 subfamily and its possible co-chaperone.* DNA Res, 1999. **6**(5): p. 299-305.
136. Schroder, H., et al., *DnaK, DnaJ and GrpE form a cellular chaperone machinery capable of repairing heat-induced protein damage.* EMBO J, 1993. **12**(11): p. 4137-44.
137. Szabo, A., et al., *The ATP hydrolysis-dependent reaction cycle of the Escherichia coli Hsp70 system DnaK, DnaJ, and GrpE.* Proc Natl Acad Sci U S A, 1994. **91**(22): p. 10345-9.

138. Herbst, R., K. Gast, and R. Seckler, *Folding of firefly (Photinus pyralis) luciferase: aggregation and reactivation of unfolding intermediates.* Biochemistry, 1998. **37**(18): p. 6586-97.
139. Borkovich, K.A., et al., *hsp82 is an essential protein that is required in higher concentrations for growth of cells at higher temperatures.* Mol Cell Biol, 1989. **9**(9): p. 3919-30.
140. Bardwell, J.C. and E.A. Craig, *Ancient heat shock gene is dispensable.* J Bacteriol, 1988. **170**(7): p. 2977-83.
141. Spence, J. and C. Georgopoulos, *Purification and properties of the Escherichia coli heat shock protein, HtpG.* J Biol Chem, 1989. **264**(8): p. 4398-403.
142. Spence, J., A. Cegielska, and C. Georgopoulos, *Role of Escherichia coli heat shock proteins DnaK and HtpG (C62.5) in response to nutritional deprivation.* J Bacteriol, 1990. **172**(12): p. 7157-66.
143. Parkinson, J.S. and S.E. Houts, *Isolation and behavior of Escherichia coli deletion mutants lacking chemotaxis functions.* J Bacteriol, 1982. **151**(1): p. 106-13.
144. Sourjik, V. and H.C. Berg, *Localization of components of the chemotaxis machinery of Escherichia coli using fluorescent protein fusions.* Mol Microbiol, 2000. **37**(4): p. 740-51.
145. Blattner, F.R., et al., *The complete genome sequence of Escherichia coli K-12.* Science, 1997. **277**(5331): p. 1453-74.
146. Baba, T., et al., *Construction of Escherichia coli K-12 in-frame, single-gene knockout mutants: the Keio collection.* Mol Syst Biol, 2006. **2**: p. 2006 0008.
147. Datsenko, K.A. and B.L. Wanner, *One-step inactivation of chromosomal genes in Escherichia coli K-12 using PCR products.* Proc Natl Acad Sci U S A, 2000. **97**(12): p. 6640-5.
148. Amann, E., B. Ochs, and K.J. Abel, *Tightly regulated tac promoter vectors useful for the expression of unfused and fused proteins in Escherichia coli.* Gene, 1988. **69**(2): p. 301-15.
149. Guzman, L.M., et al., *Tight regulation, modulation, and high-level expression by vectors containing the arabinose pBAD promoter.* J Bacteriol, 1995. **177**(14): p. 4121-30.
150. Kentner, D., et al., *Determinants of chemoreceptor cluster formation in Escherichia coli.* Mol Microbiol, 2006. **61**(2): p. 407-17.
151. Cherepanov, P.P. and W. Wackernagel, *Gene disruption in Escherichia coli: Tc^R and Km^R cassettes with the option of Flp-catalyzed excision of the antibiotic-resistance determinant.* Gene, 1995. **158**(1): p. 9-14.
152. Boehm, A., et al., *Second messenger-mediated adjustment of bacterial swimming velocity.* Cell, 2010. **141**(1): p. 107-16.
153. Sourjik, V. and H.C. Berg, *Receptor sensitivity in bacterial chemotaxis.* Proc Natl Acad Sci U S A, 2002. **99**(1): p. 123-7.
154. Zacharias, D.A., et al., *Partitioning of lipid-modified monomeric GFPs into membrane microdomains of live cells.* Science, 2002. **296**(5569): p. 913-6.
155. Berg, H.C. and P.M. Tedesco, *Transient response to chemotactic stimuli in*

Escherichia coli. Proc Natl Acad Sci U S A, 1975. **72**(8): p. 3235-9.
156. Kollmann, M., et al., *Design principles of a bacterial signalling network.* Nature, 2005. **438**(7067): p. 504-7.
157. Vladimirov, N., et al., *Dependence of bacterial chemotaxis on gradient shape and adaptation rate.* PLoS Comput Biol, 2008. **4**(12): p. e1000242.
158. Keller, A., et al., *Empirical statistical model to estimate the accuracy of peptide identifications made by MS/MS and database search.* Anal Chem, 2002. **74**(20): p. 5383-92.
159. Sprague, B.L. and J.G. McNally, *FRAP analysis of binding: proper and fitting.* Trends Cell Biol, 2005. **15**(2): p. 84-91.
160. Schulmeister, S., et al., *Protein exchange dynamics at chemoreceptor clusters in Escherichia coli.* Proc Natl Acad Sci U S A, 2008. **105**(17): p. 6403-8.
161. Miyawaki, A., *Visualization of the spatial and temporal dynamics of intracellular signaling.* Dev Cell, 2003. **4**(3): p. 295-305.
162. Foerster, T., *Zwischen Energiewanderung und Fluoreszenz.* Annalen der Physik, 1948. **6**(2).
163. Tsien, R.Y. and A. Miyawaki, *Seeing the machinery of live cells.* Science, 1998. **280**(5371): p. 1954-5.
164. Wouters, F.S. and P.I. Bastiaens, *Imaging protein-protein interactions by fluorescence resonance energy transfer (FRET) microscopy.* Curr Protoc Cell Biol, 2001. **Chapter 17**: p. Unit 17 1.
165. Sourjik, V., et al., *In vivo measurement by FRET of pathway activity in bacterial chemotaxis.* Methods Enzymol, 2007. **423**: p. 365-91.
166. Vaknin, A. and H.C. Berg, *Osmotic stress mechanically perturbs chemoreceptors in Escherichia coli.* Proc Natl Acad Sci U S A, 2006. **103**(3): p. 592-6.
167. Vaknin, A. and H.C. Berg, *Physical responses of bacterial chemoreceptors.* J Mol Biol, 2007. **366**(5): p. 1416-23.
168. Kentner, D. and V. Sourjik, *Dynamic map of protein interactions in the Escherichia coli chemotaxis pathway.* Mol Syst Biol, 2009. **5**: p. 238.
169. Fukuoka, H., et al., *Visualization of functional rotor proteins of the bacterial flagellar motor in the cell membrane.* J Mol Biol, 2007. **367**(3): p. 692-701.
170. Zhao, R., et al., *FliG and FliM distribution in the Salmonella typhimurium cell and flagellar basal bodies.* J Bacteriol, 1996. **178**(1): p. 258-65.
171. Oosawa, K., T. Ueno, and S. Aizawa, *Overproduction of the bacterial flagellar switch proteins and their interactions with the MS ring complex in vitro.* J Bacteriol, 1994. **176**(12): p. 3683-91.
172. Jones, C.J., et al., *Stoichiometric analysis of the flagellar hook-(basal-body) complex of Salmonella typhimurium.* J Mol Biol, 1990. **212**(2): p. 377-87.
173. Young, H.S., et al., *Variable symmetry in Salmonella typhimurium flagellar motors.* Biophys J, 2003. **84**(1): p. 571-7.
174. Brown, P.N., et al., *Mutational analysis of the flagellar protein FliG: sites of interaction with FliM and implications for organization of the switch complex.* J Bacteriol, 2007. **189**(2): p. 305-12.

175. Delalez, N.J., et al., *Signal-dependent turnover of the bacterial flagellar switch protein FliM.* Proc Natl Acad Sci U S A, 2010. **107**(25): p. 11347-51.
176. Fukuoka, H., et al., *Exchange of rotor components in functioning bacterial flagellar motor.* Biochem Biophys Res Commun, 2010. **394**(1): p. 130-5.
177. Kott, L., et al., *Distributed subunit interactions in CheA contribute to dimer stability: a sedimentation equilibrium study.* Biochim Biophys Acta, 2004. **1696**(1): p. 131-40.
178. Zhou, J., S.A. Lloyd, and D.F. Blair, *Electrostatic interactions between rotor and stator in the bacterial flagellar motor.* Proc Natl Acad Sci U S A, 1998. **95**(11): p. 6436-41.
179. Crooks, G.E., et al., *WebLogo: a sequence logo generator.* Genome Res, 2004. **14**(6): p. 1188-90.
180. Francis, N.R., et al., *Localization of the Salmonella typhimurium flagellar switch protein FliG to the cytoplasmic M-ring face of the basal body.* Proc Natl Acad Sci U S A, 1992. **89**(14): p. 6304-8.
181. Thomas, D., D.G. Morgan, and D.J. DeRosier, *Structures of bacterial flagellar motors from two FliF-FliG gene fusion mutants.* J Bacteriol, 2001. **183**(21): p. 6404-12.
182. Tang, H., T.F. Braun, and D.F. Blair, *Motility protein complexes in the bacterial flagellar motor.* J Mol Biol, 1996. **261**(2): p. 209-21.
183. Toker, A.S. and R.M. Macnab, *Distinct regions of bacterial flagellar switch protein FliM interact with FliG, FliN and CheY.* J Mol Biol, 1997. **273**(3): p. 623-34.
184. Brown, P.N., et al., *Crystal structure of the flagellar rotor protein FliN from Thermotoga maritima.* J Bacteriol, 2005. **187**(8): p. 2890-902.
185. Paul, K. and D.F. Blair, *Organization of FliN subunits in the flagellar motor of Escherichia coli.* J Bacteriol, 2006. **188**(7): p. 2502-11.
186. Minamino, T., et al., *Roles of the extreme N-terminal region of FliH for efficient localization of the FliH-FliI complex to the bacterial flagellar type III export apparatus.* Mol Microbiol, 2009. **74**(6): p. 1471-83.
187. Attmannspacher, U., B.E. Scharf, and R.M. Harshey, *FliL is essential for swarming: motor rotation in absence of FliL fractures the flagellar rod in swarmer cells of Salmonella enterica.* Mol Microbiol, 2008. **68**(2): p. 328-41.
188. Leake, M.C., et al., *Stoichiometry and turnover in single, functioning membrane protein complexes.* Nature, 2006. **443**(7109): p. 355-8.
189. Saijo-Hamano, Y., et al., *Structure of the cytoplasmic domain of FlhA and implication for flagellar type III protein export.* Mol Microbiol, 2010. **76**(1): p. 260-8.
190. Minamino, T., et al., *Role of the C-terminal cytoplasmic domain of FlhA in bacterial flagellar type III protein export.* J Bacteriol, 2010. **192**(7): p. 1929-36.
191. Vembar, S.S. and J.L. Brodsky, *One step at a time: endoplasmic reticulum-associated degradation.* Nat Rev Mol Cell Biol, 2008. **9**(12): p. 944-57.
192. Takaya, A., et al., *The DnaK chaperone machinery converts the native FlhD2C2 hetero-tetramer into a functional transcriptional regulator of flagellar regulon*

expression in Salmonella. Mol Microbiol, 2006. **59**(4): p. 1327-40.

6 Publications

Some of the results presented in this work have been previously included in the following papers:

1. Alex Boehm, Matthias Kaiser, **Hui Li**, Christian Spangler, Christoph Alexander Kasper, Martin Ackermann, Volkhard Kaever, Victor Sourjik, Volker Roth and Urs Jenal
   "Second messenger-mediated adjustment of bacterial swimming velocity"
   Cell, 2010, **141**(1): 107-16
   (see attached paper)

2. **Hui Li** and Victor Sourjik
   "Assembly order and stability of flagellar motor in *Escherichia coli*"
   submitted

Cell

Second Messenger-Mediated Adjustment of Bacterial Swimming Velocity

Alex Boehm,[1,*] Matthias Kaiser,[1] Hui Li,[2] Christian Spangler,[3] Christoph Alexander Kasper,[1] Martin Ackermann,[4,5] Volkhard Kaever,[3] Victor Sourjik,[2] Volker Roth,[6] and Urs Jenal[1]
[1]Biozentrum, University of Basel, CH-4056 Basel, Switzerland
[2]Zentrum für Molekulare Biologie der Universität Heidelberg, DKFZ-ZMBH Alliance, D-69120 Heidelberg, Germany
[3]Institute of Pharmacology, Hannover Medical School, 30625 Hannover, Germany
[4]Department of Environmental Sciences, ETH Zurich, CH-8092 Zürich, Switzerland
[5]Department of Environmental Microbiology, EAWAG, CH-8092 Zürich, Switzerland
[6]Department of Computer Science, University of Basel, CH-4056 Basel, Switzerland
*Correspondence: alexander.boehm@unibas.ch
DOI 10.1016/j.cell.2010.01.018

SUMMARY

Bacteria swim by means of rotating flagella that are powered by ion influx through membrane-spanning motor complexes. *Escherichia coli* and related species harness a chemosensory and signal transduction machinery that governs the direction of flagellar rotation and allows them to navigate in chemical gradients. Here, we show that *Escherichia coli* can also fine-tune its swimming speed with the help of a molecular brake (YcgR) that, upon binding of the nucleotide second messenger cyclic di-GMP, interacts with the motor protein MotA to curb flagellar motor output. Swimming velocity is controlled by the synergistic action of at least five signaling proteins that adjust the cellular concentration of cyclic di-GMP. Activation of this network and the resulting deceleration coincide with nutrient depletion and might represent an adaptation to starvation. These experiments demonstrate that bacteria can modulate flagellar motor output and thus swimming velocity in response to environmental cues.

INTRODUCTION

Actively moving cells can direct their migration toward favorable conditions by decoding extracellular gradients of metabolites either spatially or temporally (Stephens et al., 2008). Information about the environment can be translated into changing motor speed and/or directionality. *Escherichia coli* and related bacteria move by swimming through liquid environments with the help of six to eight rotating flagella that are anchored via basal bodies at randomly distributed positions in the cell envelope. When all flagellar motors simultaneously rotate in the counterclockwise (CCW) direction, the individual flagellar filaments are combined into a bundle and the cell is propelled forward in a straight run. These runs are interrupted by tumbles, short episodes of clockwise (CW) flagellar rotation, leading to bundle dispersal and a random reorientation of the cell. Tumbles are suppressed when cells happen to swim into a favorable direction. In the presence of a chemical gradient, this behavior transmits into a biased random walk that directs net migration and thus allows the bacterial cell to perform chemotaxis. Tumble events are initiated by binding of the phosphorylated form of CheY to the flagellar switch complex. The phosphorylation status of CheY and thus tumble frequency is controlled by a well-understood signal processing machinery that is able to sense, respond, and adapt to chemical gradients (Hazelbauer et al., 2008).

Flagellar rotation is powered by proton flux across inner membrane channels composed of a heterohexameric complex of the motor proteins MotA and MotB (stoichiometry $MotA_4MotB_2$) (Kojima and Blair, 2004). Eleven such stator complexes align the outside of the flagellar C ring, the cytoplasmic part of the flagellar rotor, which consists of multiple copies of the FliG, FliM and FliN proteins (Reid et al., 2006). Transformation of chemical energy from proton influx into torque is believed to involve direct electrostatic interactions between MotA and FliG, while switching from CCW to CW rotation requires interaction of phosphorylated CheY with FliM (Berg, 2003; Sowa and Berry, 2008). The stator complexes function independently of each other with a single active stator complex being sufficient to spin a flagellar filament. However, under conditions of high load (that is when high viscous drag is exerted on the filament), submaximal numbers of active stator complexes lead to intermediate rotation frequencies (Blair and Berg, 1988). When grown in batch culture, *E. coli* modulates its swimming speed, which peaks in late exponential phase and declines upon entry into stationary phase despite full flagellation (Amsler et al., 1993). Because it is known that motor speed is proportional to proton motive force (Gabel and Berg, 2003; Meister et al., 1987), it was speculated that speed variation is based on changes in proton motive force. Although different bacteria are able to swim at different maximal speeds, it is not known whether bacterial motor output is a hardwired trait or whether bacteria can modulate their velocity deliberately in response to environmental cues.

Recent reports suggested that the second messenger cyclic di-GMP (c-di-GMP) inhibits motility in bacteria (Ryjenkov et al., 2006; Wolfe and Visick, 2008). This compound is produced by a family of enzymes called diguanylate cyclases (DGCs) and is

degraded by specific phosphodiesterases (PDEs). DGCs typically harbor a C-terminal GGDEF output domain that catalyzes c-di-GMP production and an N-terminal signal input domain that regulates the activity of the catalytic domain. PDEs harbor a catalytic C-terminal EAL domain and an N-terminal signal input domain (Hengge, 2009; Jenal and Malone, 2006; Schirmer and Jenal, 2009). Whereas the catalytic mechanisms of DGCs and PDEs are relatively well understood, the nature of the signals controlling their activity is only known in a few cases. GGDEF and EAL domain proteins are found in most bacteria, and in most cases a single bacterial genome encodes many different members of these protein families (Galperin, 2005). The response to fluctuating cellular levels of c-di-GMP is mediated by a variety of specific effector proteins or RNAs that control specific cellular processes (Schirmer and Jenal, 2009). The most prevalent example of such effectors are c-di-GMP-binding proteins harboring a PilZ domain (Amikam and Galperin, 2006). YcgR, a PilZ domain protein from *E. coli*, was shown to bind c-di-GMP in vitro and to somehow interfere with *E. coli* motility upon genetic inactivation of the PDE YhjH (Ko and Park, 2000; Ryjenkov et al., 2006). Interestingly, *yhjH* and *ycgR* are coregulated with the flagellar and chemotaxis genes (Frye et al., 2006; Ko and Park, 2000). Together, these observations led to a simple model in which YhjH limits the cellular c-di-GMP concentration, thereby preventing YcgR activation by c-di-GMP, and consequently allowing for unrestricted motility. Although some DGCs were genetically linked to YcgR-mediated motility control (Girgis et al., 2007; Pesavento et al., 2008), the full network of DGCs and PDEs responsible for this behavior remained unclear. Moreover, the molecular mechanism of *how* c-di-GMP and YcgR interfere with cell motility is still elusive. While some authors proposed that YcgR regulates motility as such (Ko and Park, 2000; Ryjenkov et al., 2006), others proposed that Δ*yhjH* mutants have a chemotaxis or motor assembly defect (Girgis et al., 2007; Wolfe and Visick, 2008). In the absence of strong experimental evidence for any of these mechanisms, it even remained possible that the effect on motility is indirect, e.g., through the production of cell surface exposed adhesive factors that might slow down bacteria passively. Here, we unravel the molecular mechanism underlying c-di-GMP mediated motility control. We show that YcgR directly interacts with the flagellar motor protein MotA in response to c-di-GMP binding. We present evidence that YcgR gradually reduces flagellar motor function by inactivating individual stator units in a brake-like fashion. We suggest that the YcgR brake mechanism involves electrostatic interactions between MotA and the rotor protein FliG. Furthermore, we identify a network of five c-di-GMP signaling proteins that work synergistically to adjust the concentration of c-di-GMP in *E. coli* cells and thereby fine-tunes bacterial velocity. We propose that one physiological role of this network is to adapt bacterial swimming speed upon nutrient limitation.

RESULTS

A Network of Diguanylate Cyclases Regulates *E. coli* Motility

To test which c-di-GMP signaling components contribute to motility control in *E. coli*, we tested 29 mutants, representing all *E. coli* proteins harboring a GGDEF and/or EAL domain, for their swimming behavior in soft agar plates (0.3% agar). Bacteria in these plates generate a chemical gradient by depletion of nutrients at the site of inoculation. Motile and chemotactic cells can follow this gradient and migrate away from the center, thereby forming a concentric ''swarm'' colony. The size of these swarms is determined by swimming velocity and chemotactic performance. A mutant lacking the YhjH PDE showed a severe phenotype in this assay (Frye et al., 2006; Ko and Park, 2000; Ryjenkov et al., 2006) (Figure 1). In addition, mutational inactivation of YliE, another EAL domain protein, led to a weak motility defect (approximately 90% swarm size compared to the wild-type [WT]), while inactivation of none of the other GGDEF/EAL domain proteins had any effect (data not shown). We focused on YhjH and asked which DGC(s) are involved in blocking motility in the Δ*yhjH* mutant. To this end, the Δ*yhjH* mutation

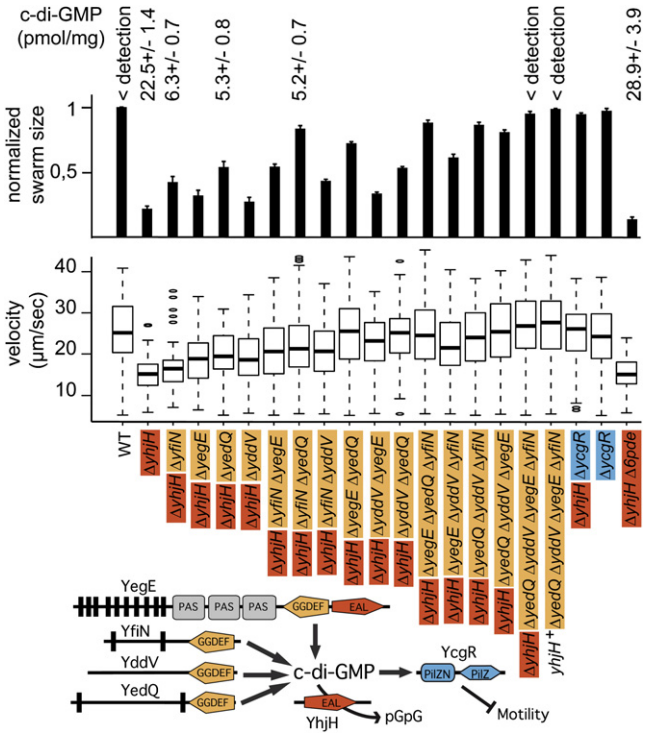

Figure 1. A c-di-GMP Network Fine-Tunes Bacterial Swimming Velocity

Normalized swarm size (with standard error bars) and median swimming velocity of *E. coli* WT and c-di-GMP signaling mutants are shown. Swimming velocities are shown as box plots summarizing velocities of at least 100 individual cells. Boxes enclose the lower and upper quartile, thick horizontal lines represent the median, dashed lines the extreme values, and circles are outliers of individual cells. C-di-GMP concentrations are indicated in pmol per mg total protein. Mutant genotypes are shown, and protein functions are indicated by a color code (orange, DGC; red, PDE; blue, YcgR). "Δ6*pde*" indicates deletion of six predicted PDE coding genes (see Table S2). The network of c-di-GMP signaling proteins is indicated at the bottom of the figure. "pGpG," linear dimeric GMP. Vertical bars represent transmembrane helices. Pairwise comparisons of the WT and the Δ*yhjH* mutant with all other mutants for different median swimming velocities are shown in Table S1. See also Figure S1 and Movie S1.

was individually combined with mutations inactivating all 19 proteins harboring a GGDEF domain. Deletion of the *yedQ*, *yfiN*, *yddV*, or *yegE* genes led to partial restoration of motility in the *yhjH* mutant background. Accumulation of deletions of all four genes restored motility of the Δ*yhjH* mutant strain in an additive manner. This suggested that all four proteins are DGCs that synergistically adjust the cellular c-di-GMP concentration for motility control (Figure 1). Furthermore, a *yhjH*$^+$ strain lacking the four DGCs showed a similar swarm size to the WT, the Δ*ycgR* mutant, or the Δ*yhjH* Δ*ycgR* double mutant. In summary, these data suggest that the four DGCs, YfiN, YegE, YedQ, and YddV, together with the PDE YhjH (and possibly YliE) form a network that regulates cell motility in *E. coli* by modulating cellular levels of c-di-GMP.

Fine-Tuning of Bacterial Swimming Velocity by c-di-GMP Adjustment

Although experiments with motility plates facilitate the analysis of many different mutants, this assay is not well suited to determine whether a mutant has a motility defect or is unable to follow chemical gradients. To distinguish between chemotaxis and velocity defects, we recorded trajectories of individual motile bacteria with the help of dark-field video microscopy. Under the experimental conditions used for these tracking experiments, no chemical gradients exist and cells tumble very rarely (Movie S1 available online; see also the Experimental Procedures). Determination of the swimming velocity of the Δ*yhjH* mutant revealed that this strain swims slowly, with the majority of cells displaying speeds of 12–17 μm/s (median 14.7 μm/s), compared to the WT at 20–31 μm/s (median 24.9 μm/s) or the Δ*yhjH* Δ*ycgR* mutant at 20–29 μm/s (median 25.9 μm/s) (Figure 1, Movie S1). Statistical analysis revealed that this reduction in speed is significant (Table S1). Moreover, as observed macroscopically on swarm plates, the successive deletion of diguanylate cyclases led to intermediate swimming speeds ranging between velocities for the WT and the Δ*yhjH* mutant. Simultaneous removal of all four DGCs or the deletion of *ycgR* led to swimming speeds that are slightly higher than that of the WT (median velocities of 26.5 μm/s and 26.2 μm/s, respectively). Similarly, a *yhjH*$^+$ strain lacking all four DGCs showed slightly increased motility compared to that of the WT (median velocity = 27.4 μm/s). Determination of the cellular levels of c-di-GMP in several of these strains revealed an inverse correlation between the observed swimming speed and internal c-di-GMP (Figure 1). Whereas c-di-GMP concentrations were below the detection limit in WT cells and in cells lacking all four DGCs, c-di-GMP concentrations varied in the other strains within a concentration range that corresponds well with the in vitro affinity of YcgR for its ligand (K_D in the low μM range) (Ryjenkov et al., 2006). Interestingly, deletion of six additional potential PDE coding genes ("Δ*6pde*") led to a further increase of the c-di-GMP concentration and concomitant reduction of swimming velocity and swarm size compared to a Δ*yhjH* single mutant (Figure 1). This indicated that additional components of the *E. coli* c-di-GMP network are involved in swimming speed control.

Comparison of the data obtained with motility plates and with single cell analysis revealed a remarkable congruence of the macroscopic and microscopic measurements, indicating that (1) the c-di-GMP specific PDE YhjH limits a pool of c-di-GMP that is replenished by the synergistic action of the four DGCs, YegE, YfiN, YedQ, and YddV; and that (2) YcgR gradually decreases swimming velocity in dependence of increasing concentrations of c-di-GMP. Although these experiments strongly suggested that c-di-GMP and YcgR control swimming speed, we wanted to test an additional effect of these components on chemotaxis. For this, we used in vivo fluorescence resonance energy transfer (FRET) measurements to quantitatively probe the interaction between CheY-YFP and the switch complex protein CFP-FliM under steady state and stimulatory conditions. No relevant difference between the WT and the Δ*yhjH* mutant was found (Figure S1), providing additional support for the idea that c-di-GMP governs cell motility primarily by modulating swimming velocity.

YcgR Controls Motor Activity through Direct Interaction with the MotA Motor Protein

To expose *how* YcgR controls motility, we isolated spontaneous motile suppressors of the Δ*yhjH* mutant. This approach is based on the idea that specific mutations in the direct molecular target of YcgR could disrupt this interaction and thereby render the target blind for high levels of c-di-GMP. Four different suppressor mutations altering two specific residues of the stator protein MotA were isolated several times independently (Extended Experimental Procedures). Three suppressors had exchanged glycine 93 to glutamate, valine, or arginine, respectively, while one suppressor had replaced serine 96 to leucine (Figure 2A). G93 and S96 are in the immediate vicinity of two highly conserved residues of MotA (R90 and E98) that are involved in electrostatic interactions with conserved residues (D289, D288, and R281) of the rotor protein FliG (Figure 2A) (Zhou et al., 1998). This MotA-FliG interaction is believed to be crucial for torque generation of the flagellar motor. All four *motA* mutations caused strong suppression of the Δ*yhjH* motility defect in motility test plates, with swarm sizes ranging from 68% to 82% of the WT swarm sizes (Δ*yhjH* shows swarm sizes below 40% of the WT; Figure S2A). When the swimming speeds of individual cells of these four suppressor mutants were analyzed with the help of video tracking, differences between the mutants became apparent. The *motA*(G93E) mutant displayed WT speed, the *motA*(G93R) mutant intermediate speed, and the *motA*(G93V) and *motA*(S96L) mutants Δ*yhjH*-like swimming velocities (Figure 2B). Since all four suppressors performed well in motility plates, we speculated that *motA*(G93V) and *motA*(S96L) might only display their enhanced swimming capability at increased viscosity, conditions that more closely mimic the situation on motility plates. Indeed, when medium viscosity was increased by the addition of Ficoll (10%), all suppressor mutants showed higher swimming speeds than the *yhjH* mutant, albeit not reaching the values of WT cells under these conditions (Figure 2B). Thus, the differences in swimming velocity between the Δ*yhjH* mutant and the motile suppressors are more pronounced under conditions of increased viscosity.

The G93 and S96 residues are conserved in MotA proteins (Figure 2A), even among species that do not possess a copy of YcgR. Moreover, the amino acid exchanges identified in this study do not occur in any native MotA sequences in the

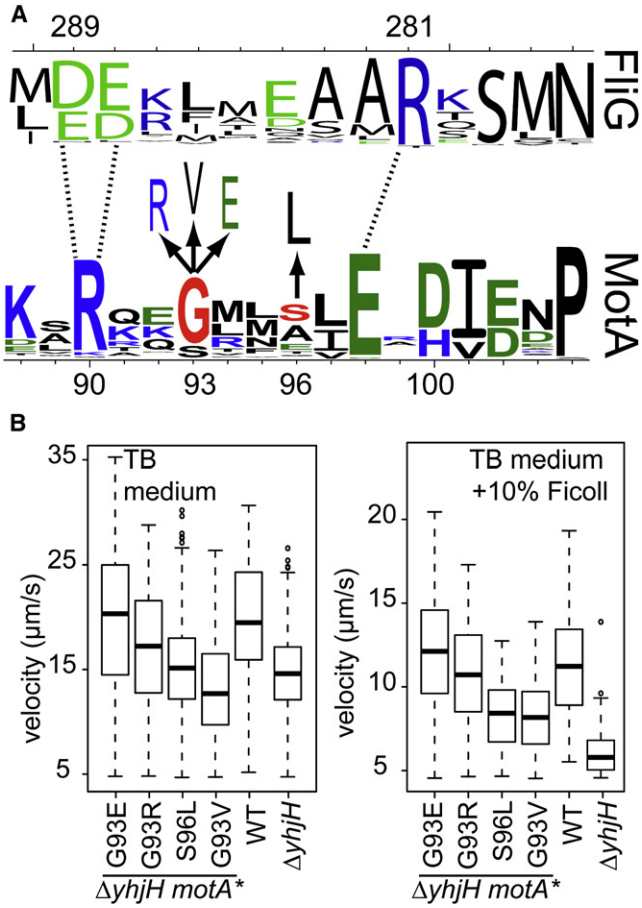

Figure 2. Mutations in *motA* Facilitate Swimming at High c-di-GMP Concentrations

(A) Motile suppressors carry exchanges in the FliG-MotA interface. A "Weblogo" (Crooks et al., 2004) representing sequence conservation among several hundred MotA and FliG homologs is shown. Numbers are according to the *E. coli* sequences, with positive (blue) and negative charges (green) highlighted. Residues exchanged in the motile suppressors are indicated in red. Dashed lines indicate postulated electrostatic interactions between stator (MotA) and rotor (FliG) residues (Zhou et al., 1998).

(B) The swimming velocities of suppressor mutants and control strains were recorded at different viscosities (with and without 10% Ficoll). Velocities of at least 100 individual cells are summarized as for Figure 1. The velocity of the Δ*yhjH* mutant is significantly different from the velocities of all other strains at high viscosity (right). At low viscosity, the velocities of the suppressors harboring the S96L and G93V alleles are not significantly different from the Δ*yhjH* mutant (left). All p values are <0.05. For the behavior of these suppressor mutants in soft agar plates or the effects of the mutations in a *yhjH*$^+$ background, see Figure S2.

databases (470 sequences were checked). This indicates that G93 and S96 might play a role in motility that goes beyond the genetic interaction with *ycgR*. Indeed, we found that two of the suppressor mutants harbor partially defective motors that outperform WT motors only under conditions of elevated c-di-GMP—e.g., in a Δ*yhjH* background—but display inferior motility in a *yhjH*$^+$ background (Figure S2B).

Nevertheless, on the basis of the above observations, it appeared plausible that YcgR directly interacts with MotA in a c-di-GMP-dependent fashion. To test this idea, we first sought to analyze the subcellular localization of YcgR with the help of a *yfp-ycgR* fusion expressed from a plasmid. As a marker for the localization of flagellar basal bodies, we coexpressed a *cfp-fliM* fusion (Sourjik and Berg, 2002). When expressed in the Δ*yhjH* mutant, both fusion proteins localized to randomly distributed foci in the cell envelope. The majority of Δ*yhjH* mutant cells showed at least two distinct YFP-YcgR foci, while some cells displayed up to eight foci (Figure 3A, Movie S2, part A). Whereas in the Δ*yhjH* mutant most of the YcgR foci colocalized with CFP-FliM foci, strains that either harbor a WT copy of *yhjH* (*yhjH*$^+$) or a deletion of *motA* (Δ*yhjH* Δ*motA*) displayed irregular, patchy YFP-YcgR fluorescence that was not cell envelope associated and did not colocalize with CFP-FliM (Figure 3A, Movie S2, parts B and E). Thus, YcgR (but not FliM) focus formation was only observed at elevated c-di-GMP (in the presence of Δ*yhjH*) and in the presence of MotA (Figure 3A). When WT *motA* was replaced by the *motA* suppressor alleles, the number of YcgR foci was strongly reduced in the absence of YhjH. The few YcgR foci still visible in the *motA* suppressor strains generally colocalized with FliM (Figure 3A; Movie S2, parts C and D; and data not shown). Together, these findings suggested that YcgR, upon binding of c-di-GMP, localizes to the flagellar motors, where it interacts with WT MotA, but less efficiently with MotA, harboring exchanges of G93 or S96.

To provide evidence for a direct interaction of YcgR and MotA in vivo, we measured FRET between MotA-CFP and YFP-YcgR fusion proteins coexpressed from plasmids. FRET was determined via acceptor photobleaching (Kentner and Sourjik, 2009) (for a typical FRET measurement, see Figure S3). Consistent with the delocalized pattern of YcgR in WT cells, no FRET signal was observed in the presence of the PDE YhjH. In contrast, the Δ*yhjH* mutant showed a pronounced FRET signal that was further increased in a strain lacking additional PDEs and thus displaying an even higher cellular level of c-di-GMP (Figure 3B). Importantly, FRET signals between YcgR and MotA variants harboring exchanges of G93 or S96 were strongly reduced or completely abolished (Figure 3B). Taken together, these experiments suggested that YcgR directly interacts with MotA complexes assembled at flagellar basal bodies and that the efficiency of this interaction correlates with the cellular level of c-di-GMP. MotA variants that fail to interact with YcgR and facilitate flagellar function at high c-di-GMP levels harbor exchanges in or close to the FliG-MotA interface, suggesting that YcgR binding might interfere with motor function by modulating the stator-rotor interaction.

YcgR Interferes with Individual Stator Units in a Brake-like Fashion

Next, we asked how YcgR controls flagellar-driven cell velocity. In principle it could—in analogy to a clutch—uncouple the stator units from the rotor (Blair et al., 2008). Alternatively, it might function in a brake-like fashion by actively decelerating or preventing flagellar rotation (including passive rotation) (Pilizota et al., 2009). To distinguish between these two possibilities, we compared the behavior of tethered cells in the Δ*yhjH* mutant and in the WT. Cells were attached via a single sheared flagellar filament to the coverslip of a microscopy chamber with the

A

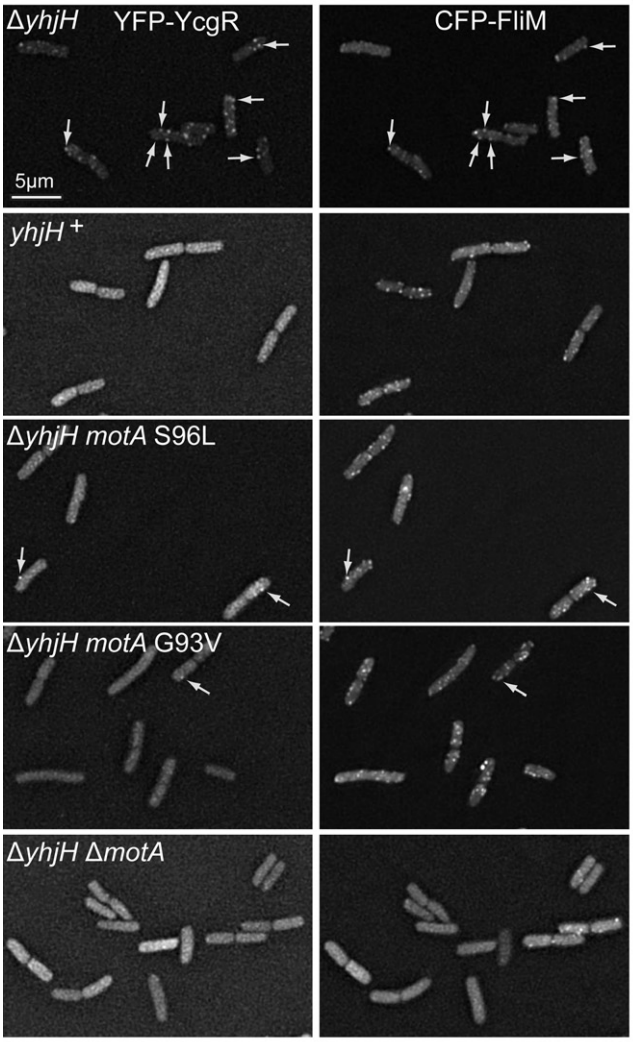

B

relevant genotype	YcgR-MotA FRET (%)	c-di-GMP (pmol/mg)
WT	0	< detection
Δ*yhjH motA*(WT)	1.48 +/- 0.031	22.5 +/- 1.4
Δ*yhjH motA*(G93E)	0	
Δ*yhjH motA*(G93V)	0.20 +/- 0.025	
Δ*yhjH motA*(G93R)	0	
Δ*yhjH motA*(S96L)	0.34 +/- 0.024	
Δ*yhjH* Δ6PDE	2.09 +/- 0.020	28.9 +/- 3.9

Figure 3. YcgR Binds to MotA in Flagellar Basal Bodies in a c-di-GMP Dependent Manner

(A) Fluorescence micrographs of WT and mutant cells coexpressing *yfp-ycgR* (left) and *cfp-fliM* (right). Images are projections of deconvolved micrographs spanning six Z positions. Arrows indicate representative fluorescent foci. Dynamic Z scans of the same samples are shown in Movie S2.

(B) Summary of in vivo acceptor photobleaching FRET experiments with YFP-YcgR and MotA-CFP. FRET values, defined as fractional change in the CFP fluorescence upon YFP bleaching, are displayed as percent above baseline with standard deviations. Typically, values above 0.5% are indicative of positive interaction (Kentner and Sourjik, 2009). Intracellular c-di-GMP concentrations of selected strains are replicated from Figure 1 for comparison. A typical FRET experiment is shown in Figure S3.

help of a flagellin-specific antibody. This allows analyzing the behavior of individual motors by scoring the rotation of the tethered cells. Three categories of cells can be distinguished in these assays: (1) Actively rotating cells ("run"); this category consists of cells that have a working flagellar motor. (2) Passively rotating cells; this category comprises cells that have unlocked stator and rotor ("clutch") *as well as* cells that are not tethered via a flagellum, but via some alternative flexible structure (e.g., a pilus) and thus are rotated passively by flow forces or Brownian motion. (3) Static cells; this category comprises cells that are tethered via a flagellum with a locked motor ("brake") *and* cells that stick to the coverslip via more than one flagellar structure or are attached nonspecifically. The Δ*yhjH* mutant showed significantly more static cells than the WT (60% versus 45%) and a fraction of actively spinning cells that was reduced accordingly (16% versus 30%). Both strains showed comparable numbers of passively rotating cells (Figure 4A). The accumulation of static cells at the expense of rotating cells was dependent on YcgR, since a Δ*yhjH* Δ*ycgR* double mutant showed numbers that were similar to WT cells. Importantly, a Δ*yhjH* Δ*motA* mutant, lacking the stator, showed no actively rotating cells but twice as many passively rotating cells as the Δ*yhjH* mutant. This excludes the possibility that the Δ*yhjH* mutant is generally more sticky and surface adherent, a phenomenon that could mask a clutch-like effect of YcgR in this assay. From this, we conclude that YcgR functions in a brake-like fashion to actively decrease torque generation by the flagellar motor. Since flagellar rotation and proton influx are tightly coupled (Gabel and Berg, 2003) and since individual stators function independently of each other in torque generation (Blair and Berg, 1988), it appears to be likely that YcgR-mediated motor curbing involves a reduction of proton influx. Together with the findings presented in Figure 1, the behavior of tethered cells suggested that, at the c-di-GMP concentrations present in a Δ*yhjH* mutant, not all flagellar motors are completely inactivated by YcgR. This raised the question of whether inactivation of one stator unit is sufficient to inactivate a flagellar motor or whether motor output could be gradually curbed by the inactivation of increasing numbers of stator complexes. To address this question, we coexpressed WT *motA* and the *motA*(G93E) suppressor allele at different relative proportions in a Δ*yhjH* mutant and determined the swimming velocities under these conditions. Five different allele combinations were used: strains that contained (1) only WT *motA*, (2) only *motA*(G93E), (3) WT *motA* in the chromosome and *motA*(G93E) on a plasmid, (4) *motA*(G93E) in the chromosome and WT *motA* on a plasmid, or (5) WT *motA* in the chromosome *and* on a plasmid. In the presence of low L-arabinose inducer concentrations (0,08%) to drive submaximal expression of the plasmid encoded *motA* alleles, four discrete velocity levels were observed (Figure 4B). When only WT MotA was present, cells displayed the slowest velocities (the small difference in median velocities between these two strains is not statistically significant). When *motA*(G93E) was expressed from the chromosome and WT *motA* from the plasmid, cells showed a small but

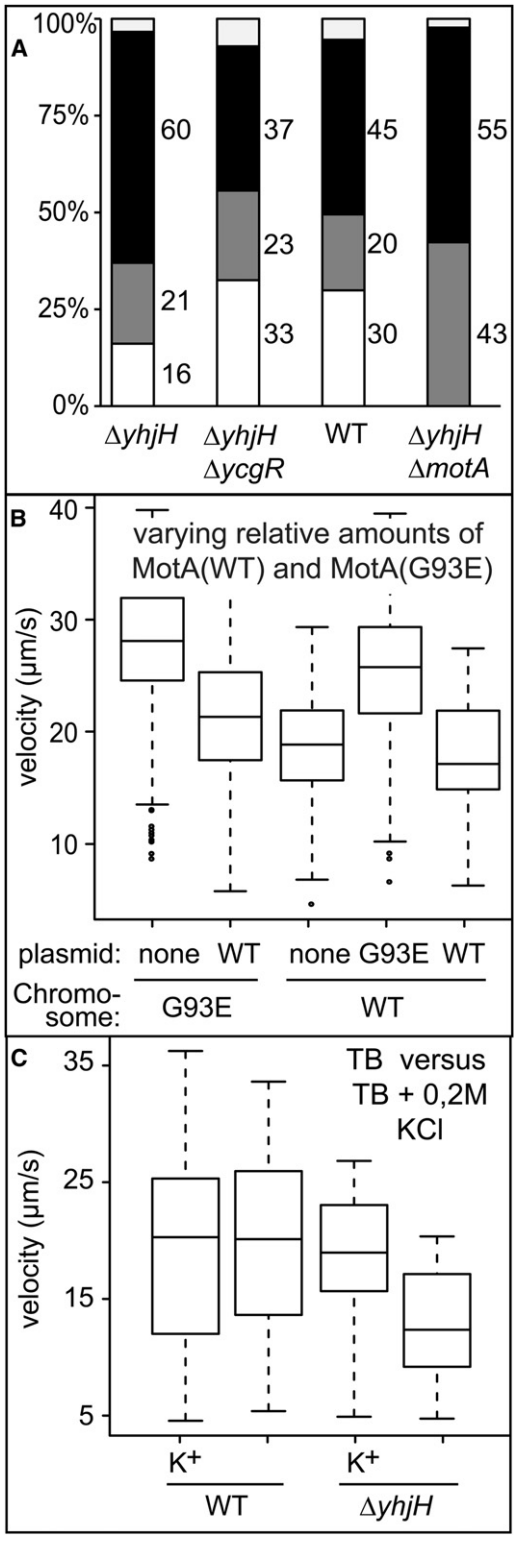

Figure 4. YcgR Limits Individual Stators in a Brake-like Fashion

(A) Rotation behavior of tethered WT and mutant cells. Tethered cells were assigned to four categories (see the Experimental Procedures): passively rotating (gray), actively rotating (white), nonrotating (black), and ambiguous (light gray). For each strain, at least 200 cells were scored, and average percentages are displayed next to bars for comparison. Statistical analysis of these data revealed that the following notions are statistically valid (for details, see the Extended Experimental Procedures): (1) The Δ*yhjH* mutant shows more static cells and less actively rotating cells than the WT or the Δ*yhjH* Δ*ycgR* mutant ($p < 0.05$). (2) The small differences for the passively rotating cells among these three strains were not found to be statistically significant despite small confidence intervals. (3) The Δ*yhjH* Δ*motA* mutant shows more passively rotating cells compared to the Δ*yhjH* mutant ($p < 0.05$).

(B) Swimming velocities of Δ*yhjH* strains coexpressing WT *motA* and the *motA* (G93E) suppressor allele. Alleles are expressed alone or reciprocally from either plasmid or the chromosome as indicated. Velocities of at least 60 individual cells are displayed as for Figure 1. Median velocities of all strains were significantly different from each other ($p < 0.05$).

(C) Swimming velocities of WT and Δ*yhjH* mutant in the presence and absence of 0.2 M K^+. Box plots summarize the velocities of at least 50 individual cells and are displayed as for Figure 1. The median velocity of the Δ*yhjH* mutant analyzed in the absence of K^+ is significantly different from the control strain and/or conditions ($p < 0.05$).

See also Figure S4.

significant increase in velocity. Velocity was further increased when *motA*(G93E) was expressed from the plasmid in the presence of a chromosomal WT *motA* copy and reached maximal levels when the *motA*(G93E) suppressor was the only *motA* copy present in the cell (Figure 4B). In the presence of higher levels of the inducer (0.2%), the plasmid-born allele of merodiploid strains [*motA*(wt) + *motA*(G93A)] became fully dominant, resulting in velocities corresponding to the respective haploid *motA* WT or *motA*(G93E) strain (data not shown). From this, we conclude that at the lower inducer concentration (0.08%), the plasmid encoded *motA* allele yields only slightly more MotA protein than the chromosomal *motA* allele, leading to intermediate velocities. In contrast, at saturating inducer concentrations (0.2%), the plasmid encoded *motA* allele produces much higher MotA protein levels than the chromosomal *motA* allele, and thus the plasmid copy becomes fully dominant. Importantly, all strains showed a unimodal speed distribution, demonstrating that intermediate velocities result from variations occurring at the cellular level (by mixing WT and mutant motor proteins) as opposed to variations at the population level (by mixing slow and fast cells) (Figure S4A). Also, when the same combinations of *motA* WT and suppressor alleles were coexpressed in a *yhjH*$^+$ strain, no speed differences were observed (Figure S4A). The observation that at elevated cellular levels of c-di-GMP coexpression of WT and suppressor *motA* alleles results in intermediate swimming velocities suggested that flagellar motors harboring a mixture of WT and YcgR-blind stator complexes display ratio-dependent intermediate motor outputs. This suggests that YcgR can inactivate individual stator complexes independently and that inactivation of a subset of stators in the same motor is not sufficient to arrest motors, but instead causes submaximal torque production.

Motor Curbing Involves Electrostatic Interactions between the Rotor and Stator

Next, we addressed the question of the molecular consequences of YcgR binding to stator complexes. Torque generation requires electrostatic interactions between the MotA stator and FliG rotor proteins. This involves MotA residues that are in the immediate vicinity of residues affecting YcgR interaction

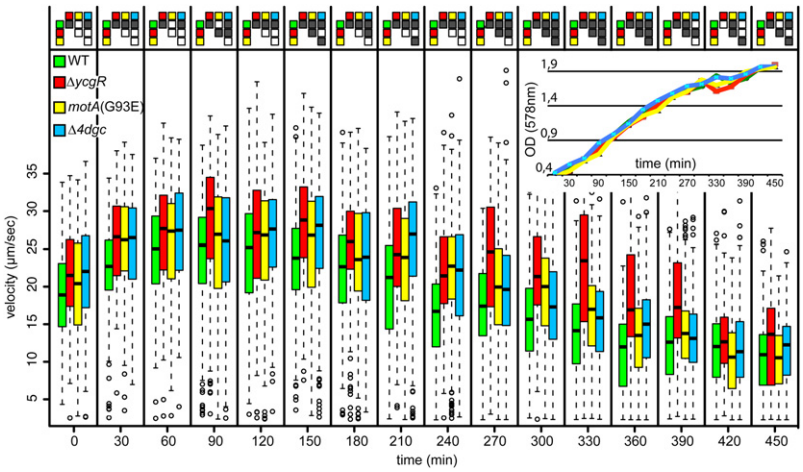

Figure 5. YcgR and c-di-GMP Control Deceleration at Entry into Stationary Phase

Velocities of individual cells of WT and mutant strains were scored in 30 min intervals throughout the growth curve starting at an optical density of 0.4 (time = 0). Velocities of at least 100 individual cells are summarized as box plots and displayed as in Figure 1. The top panel depicts a matrix of pairwise comparison of median velocities at single time points for statistically significant differences (Kruskal-Wallis rank sum test): The strain identity is indicated by color-coded squares and significant differences ($p < 0.05$) or nonsignificant differences are indicated with filled or open squares, respectively. The increase of the optical densities of each strain is shown in the inset.

(Zhou et al., 1998). The presence of high concentrations of potassium ions can affect flagellar motor function, presumably by interference with the electrostatic interactions between MotA and FliG (Zhou et al., 1998). Therefore, we tested whether potassium has an effect on the swimming performance of mutants with elevated cellular c-di-GMP levels. Remarkably, the addition of 200 mM KCl to the medium 5 min before recording bacterial swimming trajectories completely restored the swimming velocity of a Δ*yhjH* mutant to WT levels (Figure 4C). Fluorescence microscopy experiments showed that treatment with potassium did not lead to the dissociation of YcgR from the basal body complexes and thus does not influence the cellular c-di-GMP concentration or the YcgR motor interaction (Figure S4B). The potassium effect on Δ*yhjH* mutant cells was also observed on motility test plates, while Na^+ or several divalent cations had no effect on swimming performance (Figure S4C and data not shown). Also, changes of the medium pH between 4.5 and 8.3 had no influence on swimming performance of the Δ*yhjH* mutant, arguing against the idea that the reduced swimming speed of this strain is related to an altered membrane potential (data not shown). Since K^+ ions can be tolerated intracellularly in high concentrations, and considering the rapid response to K^+, a straightforward interpretation of these findings is that K^+ directly affects electrostatic interactions in the YcgR-bound MotA-FliG motor complex and thereby overcomes motor curbing.

Growth Phase-Dependent Control of Swimming Velocity Is Mediated by c-di-GMP and YcgR

Finally, we asked under which conditions the c-di-GMP signaling network (Figure 1) operates to modulate *E. coli* motility. The swimming velocity of *E. coli* depends on the growth phase with cells accelerating in midexponential phase and decelerating after reaching stationary phase. While acceleration was attributed to flagellar gene induction when cells approach stationary phase, the molecular basis for deceleration in stationary phase remained unclear (Amsler et al., 1993). Interestingly, Pesavento et al. recently showed that expression of *yhjH* is shut down upon entry of *E. coli* into stationary phase (Pesavento et al., 2008). Thus, bacterial deceleration might be a direct result of YhjH diminishment. To test this, we compared bacterial velocity of WT and three mutant strains [Δ*ycgR*, *motA(G93E)*, and Δ4*dgc*, the latter strain lacking all four DGCs linked to motility control] during different growth phases (Figure 5). All four strains showed an acceleration phase during logarithmic growth, followed by a phase of constant high velocity. This high-speed phase consistently occurred at optical densities between approximately 0.8 and 1.2 and persisted for approximately 90 to 120 min for the WT strain. The three mutants generally displayed faster swimming than the WT, with the Δ*ycgR* mutant showing the highest velocity at most time points, and the *motA*(G93E) and Δ4*dgc* strains displaying intermediate swimming speeds. As cultures approached stationary phase, velocity of WT cells gradually decreased from approximately 25 μm/s to speeds below 15 μm/s in stationary phase. In contrast, swimming speeds of the three mutant strains remained high for another 1–2 hr before these strains also decelerated and reached WT-like levels in stationary phase. This defines a window at the entry into stationary phase during which the c-di-GMP-YcgR regulatory network that we identified here intervenes with cell motility and enforces a significant reduction in swimming speed. This behavioral adaptation might be critical for a successful, energy-saving transition of rapidly propagating cells into resting cells under competitive conditions of vanishing resources.

DISCUSSION

The bacterial flagellar motor has been a fascinating studying object for more than 40 years. But despite significant advances in structure and function of the motor, a comprehensive model for the conversion of proton motive force into torque is still lacking. Here, we are adding a piece to the puzzle by showing that bacteria can fine-tune motor output by adjusting the intracellular concentration of the bacterial second messenger c-di-GMP. Our data demonstrate that intermediate c-di-GMP concentrations are translated into discrete swimming speeds and that this information is directly relayed to the flagellar motor by the c-di-GMP binding protein YcgR, which interacts with the proton channels in the cytoplasmic membrane to curb motor output. This allows cells to adapt their motility behavior in

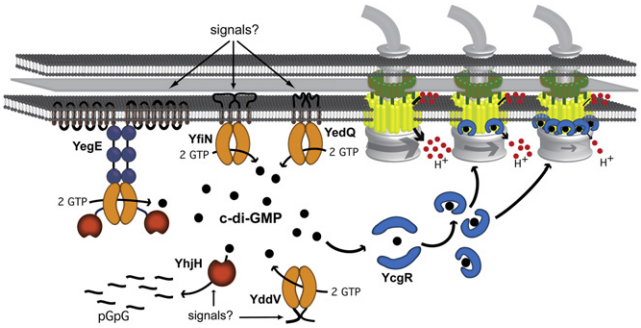

Figure 6. Model for c-di-GMP-Mediated Motor Curbing in *E. coli*

Cell envelope-spanning flagellar hook basal bodies (gray) and surrounding stator units (yellow, MotA; green, MotB) are shown. C-di-GMP is produced by four different DGCs and hydrolyzed by the PDE YhjH to linear di-GMP (pGpG). GGDEF domains (DGCs) and EAL domains (PDEs) are indicated in orange and red, respectively. Upon binding of c-di-GMP, the YcgR brake (blue) interacts with the MotA motor protein to limit individual stator complexes. Successive occupation of an increasing number of stator complexes from the same motor with c-di-GMP-loaded YcgR leads to a stepwise decrease of torque production (indicated by arrow size), which is associated with less proton (small red spheres) influx.

response to information about a changing environment and may contribute to the economic use of vanishing resources and/or to the physiological adaptation associated with the transition from a state of growth to a state of persistence.

We propose the following model for c-di-GMP mediated motor curbing (Figure 6): Docking of c-di-GMP loaded YcgR to MotA leads to reinforcement of electrostatic interactions between the stator subunit MotA and its rotor counterpart FliG. As a consequence, YcgR-free, active stators have to work against the drag imposed on the rotor by the arrested stator complexes that have YcgR latched onto. Increasing the number of YcgR-occupied stator complexes in response to higher c-di-GMP concentrations is predicted to cause a stepwise decrease of torque production and thus motor curbing. Under conditions of high load (e.g., in tethering experiments), this will eventually lead to motor arrest, whereas for a freely swimming cell this will lead to intermediate swimming velocities. The model is based on the following key findings: (1) motile suppressors that are YcgR-blind, harbor mutations in a defined region of MotA known to interact with FliG (Figure 2), (2) the efficiency of the YcgR-MotA interactions correlates with the cellular c-di-GMP concentration (Figure 3B), (3) YcgR binding to individual stator complexes leads to rotor locking rather than rotor disengagement (Figure 4A), (4) "mixed motors," which harbor WT and YcgR-blind MotA subunits, display discrete intermediate swimming speeds at high c-di-GMP concentrations (Figure 4B), and (5) the presence of potassium can overcome YcgR imposed swimming speed restriction (Figure 4C). Additional support for this model comes from "resurrection experiments," which showed that an increasing number of active stator complexes leads to discrete increments of flagellar rotation frequency (Blair and Berg, 1988; Darnton et al., 2007; Yuan and Berg, 2008). On the basis of these reports and according to our model, a flagellum with 11 stator complexes (Reid et al., 2006) could produce a maximum of 12 (0–11) output regimes that are translated into discrete swimming velocities (Figure 6). Because each stator complex harbors four copies of MotA, an alternative (but mutually not exclusive) explanation for the results obtained in Figure 4B is that intermediate swimming speeds are based on mixed individual stator complexes as opposed to mixed motors with YcgR-blind and YcgR-sensitive stators. In this scenario, the ratio of YcgR-blind and WT MotA within a stator complex would determine its efficiency, and, accordingly, each stator could produce a maximum of five different output levels.

It is noteworthy that flagellar motor arrest by a protein that functions in a brake-like fashion is not unprecedented. The monoflagellated bacterium *Rhodobacter sphaeroides* does not use a run-and-tumble mechanism, but rather a run-and-stop mechanism to perform chemotaxis. Pilizota et al. have reported recently that stopping involves rotor arrests that are mediated by one of the *Rhodobacter* homologs of CheY (Pilizota et al., 2009). Interestingly, *Rhodobacter* MotA, which shows 59% similarity to *E. coli* MotA, harbors a noncanonical sequence between the highly conserved residues R90 and E98, with G93 being deleted (Figure S2C). Poor conservation of the region of MotA implicated in motor curbing between *E. coli* and *R. sphaeroides* may reflect the fundamentally different physiological roles of their respective flagellar brakes.

It remains to be seen how many bacterial species employ a swimming speed control mechanism similar to the one described here. But, interestingly, there is a strong correlation between the presence of *motA* and the presence of GGDEF/EAL domain encoding genes in bacterial genomes. For example, of 63 bacterial species that do not harbor any GGDEF/EAL domain encoding gene (Galperin, 2005), only six species (three *Helicobacter* species, and one species each from the genera *Photorhabdus*, *Leifsonia*, and *Wigglesworthia*) harbor a copy of *motA*. Likewise, from 50 different species that harbor a YcgR-like protein (domain structure: YcgR-PilZ), all but one (*Shigella boydii*) are predicted to be motile. On the basis of these numbers, it seems likely that many bacterial species employ cyclic di-GMP signaling to control swimming velocity.

It is interesting to point out some analogies to EspE from *Bacillus subtilis*, which interferes with flagellar function in a clutch-like fashion (Blair et al., 2008). This protein was found to directly interact with the flagellar basal body, and clutch-insensitive suppressor mutations affected residues in FliG. Despite their localization outside of the FliG-MotA interface, these residues appear to be well positioned to indirectly affect the MotA-FliG interaction and thereby disengage rotor and stator. Interestingly, EspE is a glycosyltransferase implicated in exopolysaccharide biosynthesis and biofilm induction. The bifunctional EspE protein might thus directly coordinate motility control with exopolysaccharide biosynthesis to ensure successful surface colonization. Likewise, downregulation of cell motility and induction of surface adhesins and biofilm matrix components are inversely coordinated in many bacterial species by the action of DGCs and PDEs (Pesavento et al., 2008; Simm et al., 2004).

E. coli directs its movement in an aqueous environment via phosphorylation-mediated control of motor reversals. Why would bacterial cells, in addition to this sophisticated motor

control, modulate their swimming speed? It is well established that flagellar rotation rate is tightly coupled to proton influx (Gabel and Berg, 2003). A reduction of rotation speed would thus reduce the consumption of protons, and, consequently, slow swimming would save energy. Switching to a fuel-conserving locomotion regime is particularly important under low nutrient conditions. In this respect, it is noteworthy that not only is *yhjH* expression ceased at entry into stationary phase, but also that two of the four DGCs involved in velocity control, YegE and YedQ, display stationary phase induction on the transcriptional level (Weber et al., 2006). Interestingly, flagellar gene transcription has recently been found to be downregulated in stationary phase by a c-di-GMP-independent mechanism (Lemke et al., 2009). This additional level of control likely explains why cells eventually decelerate, even in the absence of *ycgR*-mediated motor curbing (Figure 5). The finding that c-di-GMP-mediated limitation of bacterial velocity coincides with entry into stationary phase, when nutrients become scarce, lends support for the idea that one function of the mechanism described here might be to adjust bacterial velocity to the energy status of the cell. Because c-di-GMP is a key factor controlling surface adherence, an alternative model could be that discrete swimming velocities reflect different stages of a preadaptation to a surface-associated, biofilm life style. A cell with curbed motor output generates less propulsion and thus has a higher propensity to become permanently attached if it happens to encounter a surface. Likewise, reduced motor activity could represent a signal to induce factors involved in surface adhesion. Thus, elevated c-di-GMP concentrations and associated slower swimming speeds in stationary phase might reflect an increasing need to settle down when nutrients become scarce.

The discovery of flagellar motor curbing might have implications beyond the biology of bacterial locomotion. On the basis of our findings, one could for example imagine to exploit the flagellar motor to engineer a rotary nanomachine that can be fine-tuned ad libitum (van den Heuvel and Dekker, 2007). The rotation speed of such a device could be controlled by adjustment of the c-di-GMP concentration with the help of DGC/PDE pairs that respond to external stimuli like light or other easily administered signals.

EXPERIMENTAL PROCEDURES

More-detailed descriptions of experimental procedures are provided in the Extended Experimental Procedures.

Video Tracking

Bacterial cells were grown in tryptone broth (TB) at 37°C to an optical density between 0.8 and 1.2 and were diluted into fresh TB at room temperature. Samples were immediately placed into microscopic chambers for recording of two 30 s videos of cells near the coverslip at 12 frames per second with a video microscope equipped with dark-field optics at 40× magnification. Video frames were imported as stacks into ImageJ 1.42 (http://rsbweb.nih.gov/ij/) and trajectories of usually several hundred bacteria were calculated with the "2D particle tracker" plugin (http://www.mosaic.ethz.ch/Downloads/ParticleTracker/). A custom made "R" script was used to compute velocities of individual bacterial cells based on particle tracker data, which contain XY coordinates of individual bacteria for each frame (http://www.r-project.org/). Experiments were repeated independently at least once, and a representative data set is shown.

Fluorescence Microscopy

E. coli cells harboring pHL55 (*yfp-ycgR*) and pVS31 (*cfp-fliM*) were grown as indicated above for video tracking, but with antibiotics to select for plasmids and with 0.04% L-arabinose to induce *cfp-fliM*. Z stacks of cells were acquired with 150 nm spacing on an Olympus IX71 microscope equipped with an UPlanSApo 100× objective and a coolSNAP HQ (Photometrics) CCD camera. Exposure times were 1.5 s for YFP and 0.5 s for CFP. Z stacks were deconvolved with softWorx (Applied Precision), and "maximum-intensity" Z projections were made with ImageJ 1.42.

FRET Measurements

E. coli cells harboring pHL55 (*yfp-ycgR*) and pHL14 (*motA-cfp*) were grown to an OD^{600} of 0.5 in the presence of 10 μM IPTG to induce *yfp-ycgR* and 0.001% L-arabinose to induce *motA-cfp*. Cells were harvested and resuspended in tethering buffer (Slocum and Parkinson, 1985), and acceptor photobleaching FRET measurements were performed on a Zeiss Axiovert 200 microscope, as described before (Kentner and Sourjik, 2009). YFP bleaching was accomplished by a 532 nm diode laser (Rapp OptoElectronic, Hamburg). For each measurement, photons were counted for 0.5 s with a counter function of the PCI-6034E board, controlled by a custom-written LabView 7.1 program (both from National Instruments, Austin, TX). CFP emission was recorded before and after bleaching of YFP by a 15 s laser pulse, and FRET was calculated as the signal increase divided by the total signal after bleaching, as defined previously (Sourjik et al., 2007).

Tethering Assay

Cells for tethering assays were grown in TB and prepared as described (Slocum and Parkinson, 1985). Movies of tethered cells were recorded with Nomarski optics and a 25× objective. Z projections of all frames in such a movie were made with ImageJ, and several hundred cells per strain and experiment were visually assigned to the categories mentioned in the results section as described in Blair et al. (2008).

Determination of Intracellular c-di-GMP Concentrations

Cultures were grown in tryptone medium to an optical density of 0.5. One milliliter aliquots were used to quantify total protein with a bicinchoninic acid assay. Cells from 5 ml culture were harvested quickly by centrifugation, and extracts were prepared essentially as described (Rabinowitz and Kimball, 2007). The extracts were analyzed by liquid chromatography-tandem mass spectrometry on an API 3000 triple-quadrupole mass spectrometer (Applied Biosystems, Foster City, CA), coupled with a Series 200 HPLC System (Perkin Elmer Instruments, Norwalk, CT). C-di-GMP was detected via selected reaction monitoring (SRM) in positive ionization mode. Liquid chromatography separation was achieved on a reversed-phase column with an ammonium acetate-methanol gradient (retention time for c-di-GMP: 8.8 min). C-di-GMP kindly provided by BioLog (Bremen, Germany) was used as an external authentic standard. Details of this method will be described elsewhere (C.S. and V.K., unpublished data).

SUPPLEMENTAL INFORMATION

Supplemental Information includes Extended Experimental Procedures, four figures, four tables, and two movies and can be found with this article online at doi:10.1016/j.cell.2010.01.018.

ACKNOWLEDGMENTS

We thank F. Hamburger for help with cloning, M. Dürrenberger for microscopy support, M. Podvinec for IT service, A. Vaknin for pAV1, and S. Parkinson for FliC antibody and advice. This work was supported by Swiss National Science Foundation Fellowship 3100A0-108186 to U.J. H.L. was supported by the Bioquant Graduate Program of Baden-Württemberg, M.A. by a grant from the Swiss National Science Foundation, and V.S. by the grant SO 421/7-1 from the Deutsche Forschungsgemeinschaft.

Received: November 3, 2009
Revised: December 9, 2009
Accepted: January 8, 2010
Published online: March 18, 2010

REFERENCES

Amikam, D., and Galperin, M.Y. (2006). PilZ domain is part of the bacterial c-di-GMP binding protein. Bioinformatics *22*, 3–6.

Amsler, C.D., Cho, M., and Matsumura, P. (1993). Multiple factors underlying the maximum motility of Escherichia coli as cultures enter post-exponential growth. J. Bacteriol. *175*, 6238–6244.

Berg, H.C. (2003). The rotary motor of bacterial flagella. Annu. Rev. Biochem. *72*, 19–54.

Blair, D.F., and Berg, H.C. (1988). Restoration of torque in defective flagellar motors. Science *242*, 1678–1681.

Blair, K.M., Turner, L., Winkelman, J.T., Berg, H.C., and Kearns, D.B. (2008). A molecular clutch disables flagella in the Bacillus subtilis biofilm. Science *320*, 1636–1638.

Crooks, G.E., Hon, G., Chandonia, J.M., and Brenner, S.E. (2004). WebLogo: a sequence logo generator. Genome Res. *14*, 1188–1190.

Darnton, N.C., Turner, L., Rojevsky, S., and Berg, H.C. (2007). On torque and tumbling in swimming Escherichia coli. J. Bacteriol. *189*, 1756–1764.

Frye, J., Karlinsey, J.E., Felise, H.R., Marzolf, B., Dowidar, N., McClelland, M., and Hughes, K.T. (2006). Identification of new flagellar genes of Salmonella enterica serovar Typhimurium. J. Bacteriol. *188*, 2233–2243.

Gabel, C.V., and Berg, H.C. (2003). The speed of the flagellar rotary motor of Escherichia coli varies linearly with protonmotive force. Proc. Natl. Acad. Sci. USA *100*, 8748–8751.

Galperin, M.Y. (2005). A census of membrane-bound and intracellular signal transduction proteins in bacteria: bacterial IQ, extroverts and introverts. BMC Microbiol. *5*, 35.

Girgis, H.S., Liu, Y., Ryu, W.S., and Tavazoie, S. (2007). A comprehensive genetic characterization of bacterial motility. PLoS Genet. *3*, 1644–1660.

Hazelbauer, G.L., Falke, J.J., and Parkinson, J.S. (2008). Bacterial chemoreceptors: high-performance signaling in networked arrays. Trends Biochem. Sci. *33*, 9–19.

Hengge, R. (2009). Principles of c-di-GMP signalling in bacteria. Nat. Rev. Microbiol. *7*, 263–273.

Jenal, U., and Malone, J. (2006). Mechanisms of cyclic-di-GMP signaling in bacteria. Annu. Rev. Genet. *40*, 385–407.

Kentner, D., and Sourjik, V. (2009). Dynamic map of protein interactions in the Escherichia coli chemotaxis pathway. Mol. Syst. Biol. *5*, 238.

Ko, M., and Park, C. (2000). Two novel flagellar components and H-NS are involved in the motor function of Escherichia coli. J. Mol. Biol. *303*, 371–382.

Kojima, S., and Blair, D.F. (2004). Solubilization and purification of the MotA/MotB complex of Escherichia coli. Biochemistry *43*, 26–34.

Lemke, J.J., Durfee, T., and Gourse, R.L. (2009). DksA and ppGpp directly regulate transcription of the Escherichia coli flagellar cascade. Mol. Microbiol. *74*, 1368–1379.

Meister, M., Lowe, G., and Berg, H.C. (1987). The proton flux through the bacterial flagellar motor. Cell *49*, 643–650.

Pesavento, C., Becker, G., Sommerfeldt, N., Possling, A., Tschowri, N., Mehlis, A., and Hengge, R. (2008). Inverse regulatory coordination of motility and curli-mediated adhesion in Escherichia coli. Genes Dev. *22*, 2434–2446.

Pilizota, T., Brown, M.T., Leake, M.C., Branch, R.W., Berry, R.M., and Armitage, J.P. (2009). A molecular brake, not a clutch, stops the Rhodobacter sphaeroides flagellar motor. Proc. Natl. Acad. Sci. USA *106*, 11582–11587.

Rabinowitz, J.D., and Kimball, E. (2007). Acidic acetonitrile for cellular metabolome extraction from Escherichia coli. Anal. Chem. *79*, 6167–6173.

Reid, S.W., Leake, M.C., Chandler, J.H., Lo, C.J., Armitage, J.P., and Berry, R.M. (2006). The maximum number of torque-generating units in the flagellar motor of Escherichia coli is at least 11. Proc. Natl. Acad. Sci. USA *103*, 8066–8071.

Ryjenkov, D.A., Simm, R., Römling, U., and Gomelsky, M. (2006). The PilZ domain is a receptor for the second messenger c-di-GMP: the PilZ domain protein YcgR controls motility in enterobacteria. J. Biol. Chem. *281*, 30310–30314.

Schirmer, T., and Jenal, U. (2009). Structural and mechanistic determinants of c-di-GMP signalling. Nat. Rev. Microbiol. *7*, 724–735.

Simm, R., Morr, M., Kader, A., Nimtz, M., and Römling, U. (2004). GGDEF and EAL domains inversely regulate cyclic di-GMP levels and transition from sessility to motility. Mol. Microbiol. *53*, 1123–1134.

Slocum, M.K., and Parkinson, J.S. (1985). Genetics of methyl-accepting chemotaxis proteins in Escherichia coli: null phenotypes of the tar and tap genes. J. Bacteriol. *163*, 586–594.

Sourjik, V., and Berg, H.C. (2002). Binding of the Escherichia coli response regulator CheY to its target measured in vivo by fluorescence resonance energy transfer. Proc. Natl. Acad. Sci. USA *99*, 12669–12674.

Sourjik, V., Vaknin, A., Shimizu, T.S., and Berg, H.C. (2007). In vivo measurement by FRET of pathway activity in bacterial chemotaxis. Methods Enzymol. *423*, 365–391.

Sowa, Y., and Berry, R.M. (2008). Bacterial flagellar motor. Q. Rev. Biophys. *41*, 103–132.

Stephens, L., Milne, L., and Hawkins, P. (2008). Moving towards a better understanding of chemotaxis. Curr. Biol. *18*, R485–R494.

van den Heuvel, M.G., and Dekker, C. (2007). Motor proteins at work for nanotechnology. Science *317*, 333–336.

Weber, H., Pesavento, C., Possling, A., Tischendorf, G., and Hengge, R. (2006). Cyclic-di-GMP-mediated signalling within the sigma network of Escherichia coli. Mol. Microbiol. *62*, 1014–1034.

Wolfe, A.J., and Visick, K.L. (2008). Get the message out: cyclic-Di-GMP regulates multiple levels of flagellum-based motility. J. Bacteriol. *190*, 463–475.

Yuan, J., and Berg, H.C. (2008). Resurrection of the flagellar rotary motor near zero load. Proc. Natl. Acad. Sci. USA *105*, 1182–1185.

Zhou, J., Lloyd, S.A., and Blair, D.F. (1998). Electrostatic interactions between rotor and stator in the bacterial flagellar motor. Proc. Natl. Acad. Sci. USA *95*, 6436–6441.

EXTENDED EXPERIMENTAL PROCEDURES

Construction of Strains and Plasmids

All strains are derivatives of the *Escherichia coli* K-12 wild-type MG1655 (Blattner et al., 1997) and are described in Table S2. Deletions were moved into MG1655 from a comprehensive mutant library (the "Keio collection," (Baba et al., 2006)) with the help of P1 transduction following standard protocols (Miller, 1972). A kanamycin marker used for selection during strain construction was generally removed by site specific recombination, leading to the generation of a short "Frt" scar sequence which replaces the deleted gene (Datsenko and Wanner, 2000). Gene deletions conferring a phenotype were confirmed by colony PCR. The second copy of *ycgR* in strain AB1374 was engineered by moving *lacI*^{q}, *bla* and the *ycgR* gene under control of the *lac* promoter from plasmid pAB524 (see Table S3) into the attachment site of bacteriophage λ with the help of in vivo recombination technology involving λInCh phage (Boyd et al., 2000). A *treF*::kan marker from Rho60 (Horlacher et al., 1996), which is highly cotransducible with *yhjH* was used to restore a functional copy of *yhjH* (checked by PCR) in the recipient AB1311 to yield AB1743. Plasmids are described in Table S3 and were constructed following standard molecular biology techniques with the help of PCR cloning (Sambrook et al., 1989). Final constructs were sequenced. Primer sequences are listed in Table S4.

Isolation of Motile Suppressor Mutants and Genetic Mapping

To isolate spontaneous motile suppressors, defective in a potential cellular target of YcgR, the tailor-made screening strain AB1374 (Δ*yhjH*::Frt Δ*yahA*::Frt Δ*yfeA*::Frt λ_{att}::(*bla lacI*^{q} P_{tac}::*ycgR*)) was used. In addition to having a deletion of *yhjH*, this strain lacks two additional PDE coding genes, *yahA* and *yfeA*, and harbors two copies of *ycgR* (the native copy plus an additional one under control of the *lac* promoter integrated at the attachment site of bacteriophage λ). These features were implemented to prevent the exclusive isolation of frequently occurring loss of function mutations in *ycgR* (*yhjH ycgR* double mutants are motile, see Figure 1 (Ko et al., 2000; Ryjenkov et al., 2006)) and to prevent isolation of gain of function mutations in *yahA* and *yfeA*. The latter mutations can compensate for the loss of *yhjH* by upregulation of the enzymatic activities of YahA or YfeA, respectively, and thus lead to lowering of the cellular c-di-GMP concentration. Implications of the suppressor mutations in *yahA* and *yfeA* for the structure function relationship of c-di-GMP specific phosphodiesterases will be described elsewhere.

Approximately 10^{8} AB1374 cells were placed in the center of a tryptone motility test plate (containing 10 μM isopropyl-β-D-thiogalactopyranoside) (Adler, 1966). After approx. 20h incubation at 37°C, motile suppressor mutants became visible as flares emanating from the center of the poorly motile colony. To identify the mutations causing suppression of the motility defect in the isolated spontaneous mutants, genetic mapping with the generalized transducing phage P1 was used. In brief, five independently isolated motile suppressors were individually subjected to a "transposon hop" with the help of a *himar1* mariner transposon ((Lampe et al., 1999), see Tables S2 and S3). Approx. 50000 transposon mutants from each hop were independently pooled and used to grow a P1 lysate. Some small fraction of phage particles in this lysate will by chance contain a stretch of chromosomal DNA from the motile suppressor that harbors the suppressor mutation plus a nearby transposon insertion. These rare phages were identified by transducing the Δ*yhjH* strain AB607 with the pool lysate, selecting for the kanamycin marker of the mariner transposon and screening approx. 1000 of these back transductants for motile clones on TB swarm plates (including 20mM Na-Citrate to prevent reinfection with phage P1). Rare motile transductants (approx. 0.05%) were colony purified and a clonal lysate was prepared. The clonal lysate was used as before to transduce AB607, and transductants were checked for motility. For one mutant the cotransduction frequency of the selected kanamycin resistance and the suppressor mutation was found to be 95%. Finally, the location of the transposon insertions was determined with semi-random PCR and subsequent sequencing. The insertion site of the transposon was identified between nucleotide 1976787 and 1976788 according to the colibri database (http://genolist.pasteur.fr/Colibri/). This position is 95% cotransducible with the *motAB* operon. Consequently, the *motA* and *motB* genes were sequenced. A single nucleotide exchange in *motA*, corresponding to *motA*-1(G93E) was identified. Four additional suppressor mutations were identified in GGDEF and/or EAL protein coding genes. These are expected to influence c-di-GMP levels, similarly to the mutations in *yahA* and *yfeA* (see above) and will be described elsewhere. The kanamycin marker itself does not have any influence on growth or swimming performance and was employed in subsequent strain constructions to move the *motA* suppressor mutations into different strain backgrounds. The same marker also facilitated screening for additional suppressor mutations in the *motAB* locus with the help of strain AB1397 (Δ*yhjH*::Frt Δ*yahA*::Frt Δ*yfeA*::Frt λ_{att}::(*bla lacI*^{q} P_{tac}::*ycgR*) 1976787::Tn*mariner*(kan) *motA*^{wt}), because it allows for easy enrichment of such mutations, with the help of P1 transduction.

Video Tracking

Cultures for video tracking were diluted at least 1:100 from a fresh TB over night culture into 20 ml TB in 100 ml Erlenmeyer flasks and grown at 37°C to optical densities (at 578nm) between 0.8 and 1.2 (for strain comparison) or the indicated optical densities for "speed over growth curve" experiments (see Figure 5). Aliquots were harvested and immediately diluted into fresh TB, or TB containing 10% Ficoll 400 (Pharmacia), or TB containing 0.2 M KCl at RT (between 21° and 27°C) to yield a suitable number of bacteria per field of view (e.g., at OD^{578} = 1 a 1:100 dilution is appropriate). After dilution, aliquots were immediately placed into a simple microscopic chamber (except for experiments involving K^{+}, where a 5 min recovery from osmotic upshock was allowed). The chambers consisted of a conventional microscope slide and coverslip spaced by two strips of double sided adhesive tape. These chambers are approx.

200 μm deep and accommodate a volume of approx. 50 μl. Bacterial cells were filmed close to the cover within 2 min after sample preparation with dark field optics at 40x magnification on a Polyvar (Reichert-Jung) microscope, equipped with an IQeye 703 digital camera (http://www.iqeye.com/). Under these conditions cells rarely show tumble events and most cells swim counterclockwise on circular tracks as described before (Lauga et al., 2006). Per strain and condition two 30 s avi movies from two different fields of view were recorded at 12 frames per second. No signs of photo damage to cells were detectable under these experimental conditions. Movies were imported as individual 512x384 pixel grayscale frames into ImageJ 1.42 (http://rsbweb.nih.gov/ij/) on a desktop computer and the trajectories of at least 100 bacterial cells were recorded with the help of the ''2D Particle Tracker'' plug-in (http://www.mosaic.ethz.ch/Downloads/ParticleTracker (Sbalzarini and Koumoutsakos, 2005)) with the following settings: radius = 15; cutoff = 0; percentile = 0.1; linkrange = 2, displacement = 20. Particle tracker summary files containing XY coordinate information for the center of mass of each bacterium in each frame were analyzed with the help of a custom made program implemented in ''R'' (http://www.r-project.org/). This software loads summary files from the ''2D Particle Tracker'' and eliminates trajectories that have a risk of being composed of tracks from more than a single cell (and therefore have a poor non-particle discrimination score assigned, for details see ''2D particle Tracker'' documentation). Also, trajectories shorter than 15 frames (1.24 s) or trajectories close to the edge of the field of view are discarded. The remaining trajectories are used to compute median velocities. Statistical analysis of differences in swimming speed was performed with a Kruskal-Wallis rank sum test in order to determine if there are significant differences among the population median velocities. If the general Null-hypothesis that all population medians are equal was rejected, a Bonferroni-Dunn post-hoc test (Dunn, 1964) was used for comparing the individual groups. Note that both testing procedures are very conservative, due to the parametric nature of the Kruskal-Wallis test and the full Bonferroni correction for multiple comparisons in Dunn's post test. We observed day to day variation of absolute velocities, which are most likely based on temperature differences. To account for these differences only values that were obtained on the same day in the same set of experiments are directly compared to each other. Experiments were repeated independently at least once. This setup allows for simultaneous measurements of hundreds of cells and is entirely based on non-proprietary, platform-independent software. Measured velocities compare well to velocities that have been measured for *E. coli* elsewhere (DiLuzio et al., 2005) (Alon et al., 1998).

Fluorescence Microscopy

Cells transformed with pHL55 (*yfp-ycgR*) and pVS31 (*cfp-fliM*) were grown to OD^{578} = 0.5-0.8 at 37°C in TB plus ampicillin (100μg/ml), chloramphenicol (30μg/ml) and L-arabinose (0.04%) and placed on an agarose pad (2% molecular biology grade agarose in 1x minimal salts ''A'' (Miller, 1972)) without any intermittent centrifugation step. Z-stacks (150nm spacing) were simultaneously acquired at two different wavelengths, with the ''changing wavelength first'' option activated, on an Olympus IX71 microscope equipped with an UPlanSApo 100 × /1.40 oil immersion objective and a coolSNAP HQ (Photometrics) CCD camera. YFP fluorescence was recorded at excitation 500/20 nm and emission 535/30 nm with 1.5 s exposure time; CFP fluorescence with excitation 436/10 and emission 470/30 nm with 0.5 s exposure. Images were deconvolved for 10 cycles with softWoRx version 3.6 (Applied Precision) at ''aggressive'' ratio and ''high'' noise filtering. Projections of pictures from 5-6 different focused Z-planes were prepared with the ''maximum intensity'' algorithm in ImageJ 1.42 (http://rsbweb.nih.gov/ij/).

Fluorescence Resonance Energy Transfer (FRET) Measurements

Cells were grown as for microscopy but at 34°C for about 4 hr, to an OD^{600} of 0.45-0.5, in the presence of 10μM isopropyl-β-D-thiogalactopyranoside and 0.001% L-arabinose to induce fusion protein production from pHL55 and pHL14, respectively. Cells were harvested by centrifugation (4000 r.p.m., 5 min), washed and resuspended in tethering buffer (10mM potassium phosphate, 0.1mM EDTA, 1 mM L-methionine, 67 mM sodium chloride, 10 mM sodium lactate, pH 7). FRET measurements were performed on a Zeiss Axiovert 200 microscope, as described before (Kentner et al., 2006). For acceptor photobleaching, cells were concentrated about tenfold by centrifugation, resuspended in tethering buffer and applied to a thin agarose pad (1% agarose in tethering buffer). Excitation light was from a 75 XBO lamp, and bleaching of YFP was accomplished by a 532 nm diode laser (Rapp OptoElectronic, Hamburg). Emission from the field of view was narrowed with a diaphragm to the area bleached by the laser and passed through a BP 485/40 filter onto a photon multiplier (Hamamatsu H7421-40, Hamamatsu, Bridgewater, NJ). For each measurement point, photons were counted for 0.5 s using a counter function of the PCI-6034E board, controlled by a custom-written LabView 7.1 program (both from National Instruments, Austin, TX). CFP emission was recorded before and after bleaching of YFP by a 15 s laser pulse, and FRET was calculated as the signal increase divided by the total signal after bleaching, as defined previously (Sourjik et al., 2007).

To measure concentration dependence of FRET responses to chemostimulation, cells coexpressing CheY-YFP and CFP-FliM from one bicistronic construct (pAV1) were attached to a polylysine-coated coverslip and placed in a flow cell, which was kept under constant flow (500 μl/min) of tethering buffer by a syringe pump (Harvard Apparatus). By rapid exchange of the buffer reservoir, solutions of 30 μM α-methyl-D,L-aspartate (Sigma) in tethering buffer were added or removed. FRET, defined as the fractional change in cyan fluorescence due to energy transfer, was calculated from changes in the ratios of yellow and cyan fluorescence signals, using KaleidaGraph 3.6 (Synergy Software, Reading, PA).

Tethering Assay

Cells for tethering assays were grown in TB at 37°C to OD^{578} = 0.2-0.3 and prepared as described (Slocum and Parkinson, 1985). 30 s movies of tethered cells were recorded as described for video tracking, but with nomarski optics and a 25x air obejctive. Z-projections of all frames in such a movie were made with ImageJ and several hundred cells per strain and experiment were visually assigned to one of the following categories, essentially as described in (Blair et al., 2008): "Run" (cells that spin actively), "Clutch" (cells that are passively rotated), "Brake" (cells that do not move) or ambiguous (cells that could not be clearly assigned). To compare the fractions of cells in the four categories between genotypes, we used an analysis of variance (procedure GLM in the statistical software JMP 7.0.1). The data was arcsine(sqrt)-transformed to achieve approximately normally distributed residuals. The analysis was based on experiments from two experimental blocks that were done at two different times. Figure 4A shows the results of the second experimental block. For the statistical analysis, we combined both blocks, and introduced a random factor into the analysis to correct for possible effects of the blocks.

SUPPLEMENTAL REFERENCES

Adler, J. (1966). Chemotaxis in bacteria. Science *153*, 708–716.

Alon, U., Camarena, L., Surette, M.G., Aguera y Arcas, B., Liu, Y., Leibler, S., and Stock, J.B. (1998). Response regulator output in bacterial chemotaxis. EMBO J. *17*, 4238–4248.

Amann, E., Ochs, B., and Abel, K.-J. (1988). Tightly regulated tac promoter vectors useful for the expression of unfused and fused proteins in Escherichia coli. Gene *69*, 301–315.

Baba, T., Ara, T., Hasegawa, M., Takai, Y., Okumura, Y., Baba, M., Datsenko, K.A., Tomita, M., Wanner, B.L., and Mori, H. (2006). Construction of Escherichia coli K-12 in-frame, single-gene knockout mutants: the Keio collection. Mol. Syst. Biol. *2*, 2006.0008.

Bibikov, S.I., Biran, R., Rudd, K.E., and Parkinson, J.S. (1997). A signal transducer for aerotaxis in *Escherichia coli.* J. Bacteriol. *179*, 4075–4079.

Blattner, F.R., Plunkett, G., 3rd, Bloch, C.A., Perna, N.T., Burland, V., Riley, M., Collado-Vides, J., Glasner, J.D., Rode, C.K., Mayhew, G.F., et al. (1997). The complete genome sequence of Escherichia coli K-12. Science *277*, 1453–1462.

Boyd, D., Weiss, D.S., Chen, J.C., and Beckwith, J. (2000). Towards single-copy gene expression systems making gene cloning physiologically relevant: lambda InCh, a simple Escherichia coli plasmid-chromosome shuttle system. J. Bacteriol. *182*, 842–847.

Datsenko, K.A., and Wanner, B.L. (2000). One-step inactivation of chromosomal genes in Escherichia coli K-12 using PCR products. Proc. Natl. Acad. Sci. USA *97*, 6640–6645.

DiLuzio, W.R., Turner, L., Mayer, M., Garstecki, P., Weibel, D.B., Berg, H.C., and Whitesides, G.M. (2005). *Escherichia coli* swim on the right-hand side. Nature *435*, 1271–1274.

Dunn, O.J. (1964). Multiple comparisons using rank sums. Technometrics *6*, 241–252.

Guzman, L.M., Belin, D., Carson, M.J., and Beckwith, J. (1995). Tight regulation, modulation, and high-level expression by vectors containing the arabinose PBAD promoter. J. Bacteriol. *177*, 4121–4130.

Horlacher, R., Uhland, K., Klein, W., Ehrmann, M., and Boos, W. (1996). Characterization of a cytoplasmic trehalase of Escherichia coli. J. Bacteriol. *178*, 6250–6257.

Kentner, D., Thiem, S., Hildenbeutel, M., and Sourjik, V. (2006). Determinants of chemoreceptor cluster formation in *Escherichia coli.* Mol. Microbiol. *61*, 407–417.

Ko, B.C.B., Turck, C.W., Lee, K.W.Y., Yang, Y., and Chung, S.S.M. (2000). Purification, identification, and characterization of an osmotic response element binding protein. Biochem. Biophys. Res. Commun. *270*, 52–61.

Lampe, D.J., Akerley, B.J., Rubin, E.J., Mekalanos, J.J., and Robertson, H.M. (1999). Hyperactive transposase mutants of the Himar1 mariner transposon. Proc. Natl. Acad. Sci. USA *96*, 11428–11433.

Lauga, E., DiLuzio, W.R., Whitesides, G.M., and Stone, H.A. (2006). Swimming in circles: motion of bacteria near solid boundaries. Biophys. J. *90*, 400–412.

Metcalf, W.W., Jiang, W., Daniels, L.L., Kim, S.K., Haldimann, A., and Wanner, B.L. (1996). Conditionally replicative and conjugative plasmids carrying lacZ alpha for cloning, mutagenesis, and allele replacement in bacteria. Plasmid *35*, 1–13.

Miller, J.H. (1972). Experiments in Molecular Genetics (Cold Spring Harbor, New York: Cold Spring Harbor Laboratory Press).

Sambrook, J., Fritsch, E.F., and Maniatis, T. (1989). Molecular Cloning: A Laboratory Manual (Cold Spring Harbor, New York: Cold Spring Harbor Laboratory Press).

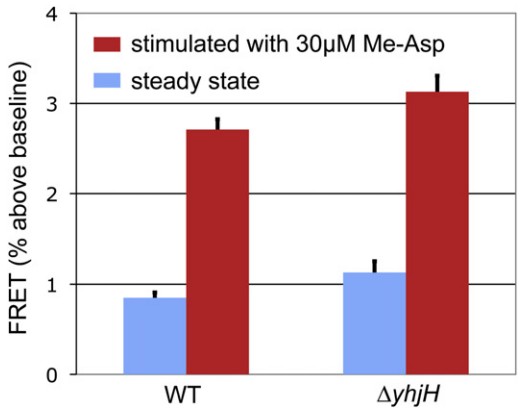

Figure S1. The Δ*yhjH* Mutant Shows Normal Interaction of CheY-P and the Switch (FliM), Related to Figure 1

FRET (expressed as % fractional change of CFP fluorescence) between CheY-YFP and CFP-FliM is compared between the wild-type and Δ*yhjH* mutant in the absence and presence of a saturating concentration of attractant (30μM α-methyl-D,L-aspartate). Stimulated values are shown in red, steady state values are shown in blue.

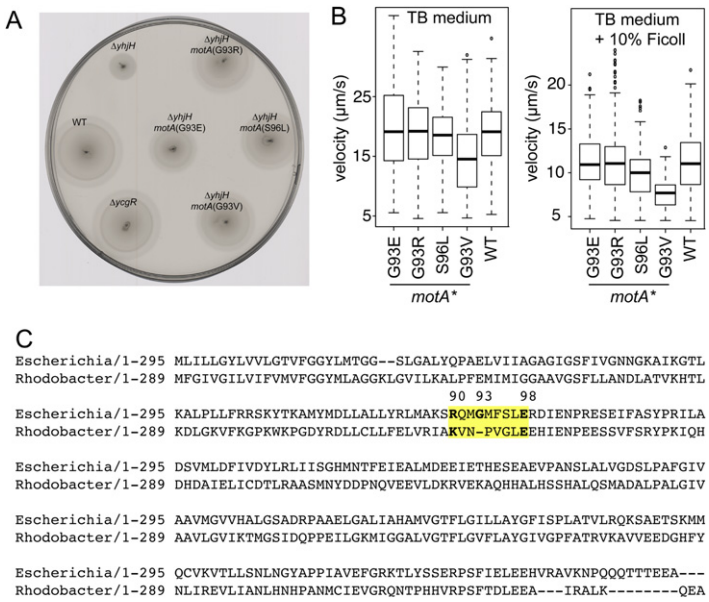

Figure S2. Related to Figure 2

(A) Suppressor mutants perform well in motility test plates. Motility behavior of the four suppressor mutants is compared to wild-type, a Δ*yhjH* and a Δ*ycgR* mutant in tryptone motility test plates (plate diameter = 150 mm, incubation time ca. 7h at 37°C).

(B) Glycine 93 and serine 96 have a general role for motor function. The swimming velocities of mutants harboring *motA* suppressor alleles in a *yhjH*$^+$ background as well as control strains were recorded at two different viscosities (with and without 10% Ficoll). At low viscosity the velocity of the *motA*(G93V) mutant is significantly different from wild-type velocity (left panel), at high viscosity, both the *motA*(G93V) and *motA*(S96L) mutants are significantly different from the wild-type (right panel). All p-values are < 0.05. Given the high conservation of the glycine residue at position 93, it is likely that the G93E and G93R exchanges will cause a deleterious effect under some unknown conditions, relevant for bacterial motility.

(C) *Rhodobacter sphaeroides* MotA has a deletion of G93. An alignment of MotA sequences from *E. coli* and *R. sphaeroides* is shown. This alignment is based on a ClustalW multiple sequence alignment (http://www.ebi.ac.uk/Tools/clustalw2/index.html) of 440 diverse MotA sequences from the non-redundant-sequences protein database at NCBI. A region comprising amino acids 90 to 98 (according to *E. coli* numbering) is highlighted. Please compare with Figure 2A.

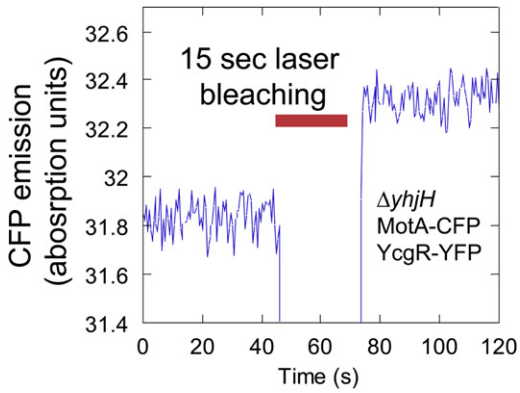

Figure S3. A typical Bleach FRET Curve, Related to Figure 3B

An example of raw data of the results displayed in Figure 3B. Samples of a Δ*yhjH* strain expressing *motA-cfp* and *yfp-ycgR* from plasmids were excited for CFP fluorescence and CFP emission was followed over time. At the indicated time (red bar), YFP is bleached with strong laser light for 15 s. Increase of CFP emission after YFP bleaching indicates FRET-based quenching of CFP before laser illumination.

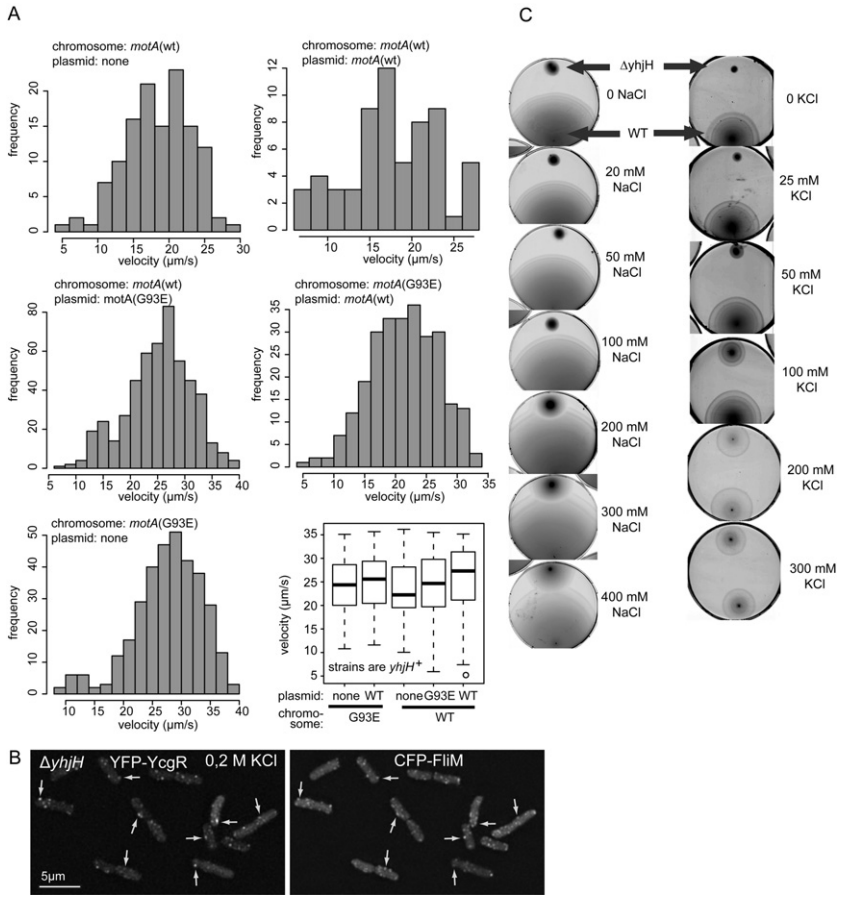

Figure S4. Related to Figure 4

(A) Swimming speeds of cells co-expressing wild-type *motA* and *motA*(G93E) are based on "mixed motors." Histograms: Populations of Δ*yhjH* strains co-expressing wild-type *motA* and *motA*(G93E) show a unimodal velocity distribution. The data shown in Figure 4B are represented as histograms to allow assessment of velocity distribution. Absolute numbers of cells are shown on the *y* axis (frequency). Relevant genotypes are indicated. Please note that scales on the X-axes are different among the different histograms to account for different boundary values. Box plot: Wild-type (*yhjH*$^+$) strains co-expressing wild-type *motA* and *motA*(G93E) show no velocity differences. Swimming velocities of the indicated *yhjH*$^+$ strains are shown as box plots that summarize the velocities of individual cells. Boxes enclose the lower and upper quartile, thick horizontal lines represent the median value, the most extreme values are indicated by the dashed lines, circles are outlier values of individual cells (see experimental procedures for details). Cells were grown as for the experiments presented in Figure 4B to $OD^{578} = 1$ at 37°C in the presence of chloramphenicol to select for the presence of plasmids and 0.08% L-arabinose to allow submaximal expression of plasmid encoded *motA* alleles. Based on a non-parametric statistical test, none of the velocities shown are significantly different in a pairwise comparison. The only exceptions are the strains harbouring wild-type *motA* on the chromosome and an empty plasmid versus wild-type *motA* in the chromosome and wild-type *motA* on the plasmid. Thus increasing the dosage of wild-type MotA in an otherwise wild-type strain appears to slightly promote swimming speed.

(B) YcgR colocalizes with flagellar basal bodies despite the presence of high K^+ concentrations. Fluorescence micrographs of cells expressing the indicated fusion proteins are shown. Arrows indicate fluorescent foci. Cultures were grown in the presence of 0.2 M KCl.

(C) High concentrations of K^+ can overcome the motility defect of a Δ*yhjH* mutant. The wild-type is compared to a Δ*yhjH* mutant in tryptone broth motility test plates containing the indicated concentrations of KCl or NaCl. Plates containing high concentrations of salts were incubated for prolonged periods to allow for reasonable colony sizes under the slow growth conditions at high salt concentrations.

Table S1. **Summary of statistical analysis for data presented in Fig. 1**
The swimming velocities of the wild type and the Δ*yhjH* mutant are compared to all other mutants with the Bonferroni-Dunn posthoc test. The overall significance level was set to alpha=0.05 which after dividing by the number of pairwise comparisons (21*20/2) results in a Bonferroni individual alpha of 0.05/210 ≈ 0.00024. Please notice that these settings lead to a very conservative testing procedure. Strain combinations are indicated by their numbers. Numbering is according to figure 1. Genotypes are indicated. Significant differences are indicated by "True", non-significant differences are indicated by "False".

Strain Number	Genotype	Combination	Significant difference	Combination	Significant difference
1	WT	1-2	TRUE	2-1	TRUE
2	ΔyhjH	1-3	TRUE	2-3	FALSE
3	ΔyhjH ΔyfiN	1-4	TRUE	2-4	FALSE
4	ΔyhjH ΔyegE	1-5	TRUE	2-5	TRUE
5	ΔyhjH ΔyedQ	1-6	TRUE	2-6	TRUE
6	ΔyhjH ΔyddV	1-7	TRUE	2-7	TRUE
7	ΔyhjH ΔyfiN ΔyegE	1-8	TRUE	2-8	TRUE
8	ΔyhjH ΔyfiN ΔyedQ	1-9	TRUE	2-9	TRUE
9	ΔyhjH ΔyfiN ΔyddV	1-10	FALSE	2-10	TRUE
10	ΔyhjH ΔyegE ΔyedQ	1-11	FALSE	2-11	TRUE
11	ΔyhjH ΔyddV ΔyegE	1-12	FALSE	2-12	TRUE
12	ΔyhjH ΔyddV ΔyedQ	1-13	FALSE	2-13	TRUE
13	ΔyhjH ΔyegE ΔyedQ ΔyfiN	1-14	TRUE	2-14	TRUE
14	ΔyhjH ΔyegE ΔyddV ΔyfiN	1-15	FALSE	2-15	TRUE
15	ΔyhjH ΔyedQ ΔyddV ΔyfiN	1-16	FALSE	2-16	TRUE
16	ΔyhjH ΔyedQ ΔyddV ΔyegE	1-17	FALSE	2-17	TRUE
17	ΔyhjH ΔyedQ ΔyddV ΔyegE ΔyfiN	1-18	FALSE	2-18	TRUE
18	yhjH^{+} ΔyedQ ΔyddV ΔyegE ΔyfiN	1-19	FALSE	2-19	TRUE
19	ΔyhjH ΔycgR	1-20	FALSE	2-20	TRUE
20	ΔycgR	1-21	TRUE	2-21	FALSE
21	ΔyhjH ΔyahA ΔyfeA ΔyjcC ΔyciR Δrtn ΔyfgF				

Table S2 Bacterial strains		
Strain	Relevant Genotype	Ancestor, comments, reference
MG1655	Wild type	K-12 wild type, (Blattner et al., 1997)
AB434	Δ*ycgR*::Frt	MG1655
AB607	Δ*yhjH*::Frt	MG1655
AB710	Δ*yhjH*::Frt Δ*yfiN*::Frt	AB607
AB711	Δ*yhjH*::Frt Δ*yedQ*::Frt	AB607
AB712	Δ*yhjH*::Frt Δ*yddV*::Frt	AB607
AB717	Δ*yhjH*::Frt Δ*ycgR*::Frt	AB607
AB725	Δ*yhjH*::Frt Δ*yedQ*::Frt Δ*yddV*::Frt	AB711
AB727	Δ*yhjH*::Frt Δ*yedQ*::Frt Δ*yfiN*::Frt	AB711
AB728	Δ*yhjH*::Frt Δ*yfiN*::Frt Δ*yddV*::Frt	AB710
AB742	Δ*yhjH*::Frt Δ*yfiN*::Frt Δ*yddV*::Frt Δ*yedQ*::Frt	AB725
AB1305	Δ*yhjH*::Frt Δ*yfiN*::Frt Δ*yegE*::Frt	AB710
AB1306	Δ*yhjH*::Frt Δ*yedQ*::Frt Δ*yegE*::Frt	AB711
AB1307	Δ*yhjH*::Frt Δ*yddV*::Frt Δ*yegE*::Frt	AB712
AB1308	Δ*yhjH*::Frt Δ*yedQ*::Frt Δ*yddV*::Frt Δ*yegE*::Frt	AB725
AB1309	Δ*yhjH*::Frt Δ*yedQ*::Frt Δ*yfiN*::Frt Δ*yegE*::Frt	AB727
AB1310	Δ*yhjH*::Frt Δ*yfiN*::Frt Δ*yddV*::Frt Δ*yegE*::Frt	AB728
AB1312	Δ*yhjH*::Frt Δ*yegE*::Frt	AB607
AB1311	Δ*yhjH*::Frt Δ*yfiN*::Frt Δ*yddV*::Frt Δ*yedQ*::Frt Δ*yegE*::Frt	AB742
AB1743	*treF*:: kan *yhjH*$^+$ Δ*yfiN*::Frt Δ*yegE*::Frt Δ*yddV*::Frt Δ*yedQ*::Frt	AB1311, *treF* is highly cotransducible w/ *yhjH*
AB1374	Δ*yhjH*::Frt Δ*yahA*::Frt Δ*yfeA*::Frt λ_{att}::(*bla lacI*^{q} P_{tac}::*ycgR*)	AB607, screening strain
AB1397	Δ*yhjH*::Frt Δ*yahA*::Frt Δ*yfeA*::Frt λ_{att}::(*bla lacI*^{q} P_{tac}::*ycgR*) 1976787::Tn*mariner*(kan)	AB1374 with *motA*-cotransducible marker
AB1468	Δ*yhjH*::Frt 1976787::Tn*mariner*(kan) *motA*-1 (G93E)	mot$^+$ suppressor of AB607
AB1576	Δ*yhjH*::Frt 1976787::Tn*mariner*(kan) *motA*-4 (G93R)	mot$^+$ suppressor of AB607
AB1577	Δ*yhjH*::Frt 1976787::Tn*mariner*(kan) *motA*-2 (S96L)	mot$^+$ suppressor of AB607
AB1578	Δ*yhjH*::Frt 1976787::Tn*mariner*(kan) *motA*-3 (G93V)	mot$^+$ suppressor of AB607
AB1469	1976787::Tn*mariner*(kan) *motA*-1 (G93E)	mot$^+$ suppressor mutations in *yhjH*$^+$ backgr.
AB1579	1976787::Tn*mariner*(kan) *motA*-4 (G93R)	mot$^+$ suppressor mutations in *yhjH*$^+$ backgr.
AB1580	1976787::Tn*mariner*(kan) *motA*-2 (S96L)	mot$^+$ suppressor mutations in *yhjH*$^+$ backgr.
AB1581	1976787::Tn*mariner*(kan) *motA*-3 (G93V)	mot$^+$ suppressor mutations in *yhjH*$^+$ backgr.
AB1643	Δ*yhjH*::Frt Δ*motA*::kan	AB607
AB1718	Δ*yhjH*::Frt Δ*yahA*::Frt Δ*yfeA*::Frt Δ*yjcC*::Frt Δ*rtn*::Frt Δ*yciR*::Frt Δ*yfgF*::Frt	AB607, "Δ6*pde*"
AB1753	Δ*yhjH*::Frt Δ*ycgR*::Frt Δ*motA*::Frt	AB717
AB1756	Δ*yhjH*::Frt Δ*ycgR*::Frt 1976787::Tn*mariner*(kan) *motA*-3 (G93V)	AB717
AB1757	Δ*yhjH*::Frt Δ*ycgR*::Frt 1976787::Tn*mariner*(kan) *motA*-2 (S96L)	AB717
AB1755	Δ*yhjH*::Frt Δ*ycgR*::Frt Δ*fliG*::kan	AB717
BW20767	RP4-2-*tet*:Mu-1*kan*::Tn*7* integrant *leu-63*::IS*10 recA1 creC510 hsdR17 endA1 zbf-5 uidA*(Δ*Mlu*I)::*pir*$^+$ *thi*	pAB540 delivery strain (Metcalf et al., 1996)

Table S3 Plasmids		
plasmid	Relevant Genotype	comments, reference
pBAD33	*cat*$^{+}$ P_{BAD} *araC* p15A	L-arabinose inducible expression vector, (Guzman et al., 1995)
pTrc99	*bla*$^{+}$ (amp^{R}) P_{tac} *lacI*^{q}	IPTG inducible expression vector, (Amann et al., 1988)
pCJ30	*bla*$^{+}$ (amp^{R}) P_{lac} *lacI*^{q}	IPTG inducible expression vector, (Bibikov et al., 1997)
pAB524	*ycgR*$^{+}$	pCJ30 based *ycgR* expression vector, this work
pAB560	*motAB*$^{+}$	pBAD33 based *motAB* expression vector, this work
pAB571	*motA-1*(G93E) *motB*$^{+}$	pBAD33 based *motA* suppressor allele expression vector, this work
pVS31	*cfp-fliM*	pBAD33 based *cfp-fliM* expression vector, (Sourjik and Berg, 2002)
pHL55	*yfp-ycgR*	pDK4 based *yfp-ycgR* expression vector, this work
pHL14	*motA-cfp*	pDK79 based *motA-cfp* expression vector, this work
pAB561	*motA-1*(G93E)-*cfp*	*motA* suppressor mutations in pHL14, this work
pAB564	*motA-4*(G93R)-*cfp*	
pAB563	*motA-3*(G93V)-*cfp*	
pAB562	*motA-2*(S96L)-*cfp*	
pAB540	Tn*mariner*(kan) *bla tnp*$^{+}$ OriT OriR6Kγ	Conjugation competent, conditionally replicative *Himar*1 based Transposon delivery vector (Lampe et al., 1999), this work
pDK4	pTrc99 derived N-terminal YFP^{A206K} fusion expression vector,	(Kentner et al., 2006)
pDK79	General expression vector; p15A ori, pBAD promoter, Kan^{R}	
pAV1	pTrc99 derived CheY-YFP CFP-FliM expression plasmid	Personal gift from Ady Vaknin (Hebrew University) to H.L.

Table S4 Oligonucleotides used as PCR primers		
Designation	Sequence 5′->3′	Function, final construct
1451	AActgcagAGTCATTACCATGAGCAGTTCCTG	Cloning *ycgR*, pAB524
1452	tacccAAGCTTaaTCAGTCGCGCACTTTGTCCG	
2934	ggGGTACCggtcaacagtggaaggatgatgtcG	Cloning *motA*, pAB560
2935	gcTCTAGAccatgctcacgctgTCACCTCGG	
3013	cgcggcagatgGTGatgttttcgctg	Site directed mutagenesis, pAB563
3014	cagcgaaaacatCACcatctgccgcg	
3015	cgcggcagatgGAGatgttttcgctg	Site directed mutagenesis, pAB561
3016	cagcgaaaacatCTCcatctgccgcg	
3017	cgcggcagatgAGGatgttttcgctg	Site directed mutagenesis, pAB564
3018	cagcgaaaacatCCTcatctgccgcg	
3019	gatggggatgtttTTGctggaacgtg	Site directed mutagenesis, pAB562
3020	cacgttccagCAAaaacatccccatc	
1641	AAGAGAATGCCGCGACATCTTTGC	Confirming *yfiN* deletion
1642	TCACCATAGTTATCGGTGTGTCCATCC	
1643	gttacggttaaagagggcggccc	Confirming *yedQ* deletion
1644	gacctatcaacaattgtcaggcaaacg	
1645	CAAAGTCGCTGGGGCAGTTAAACTC	Confirming *yddV* deletion
1646	ttttcgttaattaacaccgcacc	
2123	gttaaacgcagttgcgcaaattatcc	Confirming *yegE* deletion
2124	ctggcgttcttatgcgctgttgc	
1658	tcatgcattcgccaatcacggc	Confirming *yhjH* deletion
1659	cgcgtggcaaatgcaccatcg	
1619	GGGCGTCGATCCACAATTGATCACG	Confirming *ycgR* deletion
1620	aaagcggatagcggcatctgtatcg	